IS-T 1910

Characterization of the Dilute Ising Antiferromagnet

by

Wiener, Timothy

MS Thesis submitted to Iowa State University

Ames Laboratory, U.S. DOE
Iowa State University
Ames, Iowa 50011-3020

Date Transmitted: Sept. 12, 2000

PREPARED FOR THE U.S. DEPARTMENT OF ENERGY
UNDER CONTRACT NO. W-7405-Eng-82.

DISCLAIMER

DISCLAIMER

Portions of this document may be illegible in electronic image products. Images are produced from the best available original document.

Characterization of the dilute Ising antiferromagnet $Y_{1-x}Tb_xNi_2Ge_2$ and the search for a potential Ising spin glass

Timothy Allen Wiener

Major Professor: Paul C. Canfield

Iowa State University

A spin glass is a magnetic ground state in which ferromagnetic and antiferromagnetic exchange interactions compete, thereby creating frustration and a multidegenerate state with no long range order. An Ising system is a system where the spins are constrained to lie parallel or antiparallel to a primary axis. There has been much theoretical interest in the past ten years in the effects of applying a magnetic field transverse to the primary axis in an Ising spin glass at low temperatures and thus study phase transitions at the T=0 limit.

The focus of this study is to search for and characterize a new Ising spin glass system. This is accomplished by site diluting yttrium for terbium in the crystalline material $TbNi_2Ge_2$. The first part of this work gives a brief overview of the physics of rare earth magnetism and an overview of experimental characteristics of spin glasses. This is followed by the methodology used to manufacture the large single crystals used in this study, as well as the measurement techniques used. Next, a summary of the results of magnetic measurements on across the dilution series from pure terbium to pure yttrium is

presented. This is followed by detailed measurements on particular dilutions which demonstrate spin glass behavior.

Pure $TbNi_2Ge_2$ is an Ising antiferromagnet with a several distinct metamagnetic states below 17 K. As the terbium is alloyed with yttrium, these magnetic states are weakened in a consistent manner, as is seen in measurements of the transition temperatures and analysis of Curie-Weiss behavior at high temperature. At low concentrations of terbium, below 35 %, long range order is no longer present and a spin-glass-like state emerges. This state is studied through various measurements, dc and ac susceptibility, resistivity, and specific heat. This magnetic behavior was then compared to that of other well characterized spin glasses. It is concluded that there is a region of concentrations for which a spin glass state is formed with the best spin glasses existing between the concentrations of 25 % and 30 %

Graduate College

Iowa State University

This is to certify that the Master's thesis of

Timothy Allen Wiener

has met the thesis requirements of Iowa State University

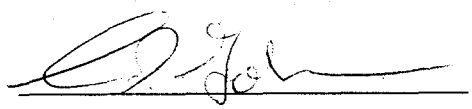

Committee Member

Committee Member

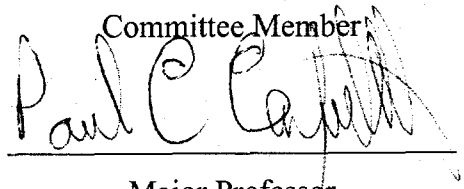

Major Professor

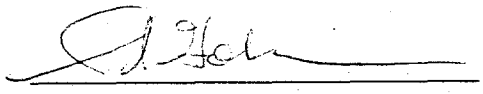

For the Major Program

For the Graduate College

TABLE OF CONTENTS

1. INTRODUCTION

1.1. Introduction

In this work experiments will be described that were performed to characterize the candidate metallic, Ising spin glass system $Y_{1-x}Tb_xNi_2Ge_2$. It will be shown that this system maintains its Ising behavior for all values of x and that this system is indeed a good spin glass. A brief motivation for the study of Ising spin glasses is given below. After an overview of the physics of spin glasses, a brief discussion will be presented of the methods used to grow single crystals from a flux growth technique and of the measurements used to characterize the system. In Chapter 5, properties of the system as a whole will be presented. This will lead to a division of the system into four concentration (x) regimes. Representative concentrations from three of these regimes will be looked at in some detail. The fourth of these regions, which displays the hallmarks of spin glasses, will be studied in Chapter 6, where it will be shown that concentrations of $0.25<x<0.35$ are good spin glasses. This will be followed by a brief conclusion and an outline of proposed future work.

1.2. The Non-metallic Ising Spin Glass: $LiHo_xY_{1-x}F_4$

Recent investigations into Ising spin glasses were performed on members of the dilution series $LiHo_xY_{1-x}F_4$. These crystals are a site-diluted and isostructural derivative of the dipolar-coupled, insulating, Ising ferromagnet $LiHoF_4$ which has a T_c of 1.53 K.

The spin glass transition temperature for the concentration x = 0.167 is T_g = 0.13 K. It has been shown that the application of a transverse magnetic field, H_t, perpendicular to the easy axis depresses the spin glass transition temperature (Figure 1.1) (Rosenbaum, 1991). This effect has made it possible to study phase transition in the quantum (T=0) regime.

Theoretically, this behavior is possibly described by the inclusion of a second term in the classical Hamiltonian for an Ising model. This gives for N interacting spins

$$H = -\sum_{i,j}^{N} J_{ij}\sigma_i^z\sigma_j^z - \Gamma\sum_{i}^{N}\sigma_i^x , \qquad (1.1)$$

where the σ's are the Pauli spin matrices, the random exchange J_{ij}'s connect spins *i* and *j*, and Γ is a transverse interaction energy which is related to H_t^2. The effect of this transverse interaction is to allow mixing of the original eigenstates and it is beyond the scope of this work to describe this in detail. The interested reader is directed to Rosenbaum, 1991; Wu, 1993; Rosenbaum, 1996, Brooke, 1999. From an experimental

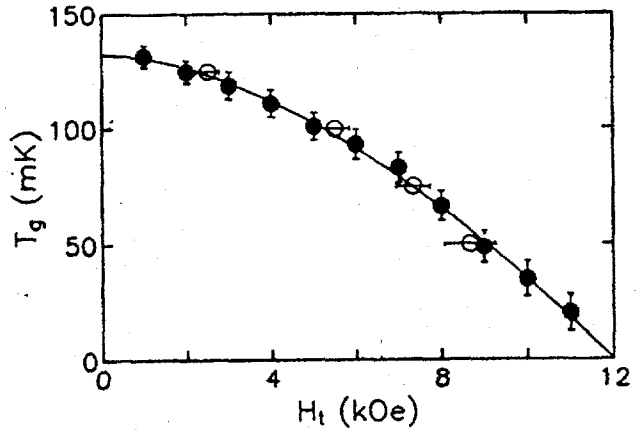

Figure 1.1. Depression of spin glass transition temperature, T_g, with the application of a transverse field, H_t (after Rosenbaum, 1991)

point of view it would be of interest to find a metallic system that manifests these properties, but with a higher T_g.

1.3. A Candidate Metallic, Ising Spin Glass $Y_{1-x}Tb_xNi_2Ge_2$

We hope to investigate whether the unusual effects observed for the insulating spin glass $LiHo_xY_{1-x}F_4$ are more general and can be seen in metallic systems. A possible candidate for a metallic Ising spin glass is the $Y_{1-x}Tb_xNi_2Ge_2$ system. This system is a site-diluted and isostructural derivative of the metallic Ising antiferromagnet $TbNi_2Ge_2$ which has an incommensurate antiferromagnetic transition at T_N of 16.7 K and a commensurate antiferromagnetic transition at 9.6 K (Bud'ko, 1999; Islam, 1998). Here the spins are coupled primarily by the RKKY interaction rather than the dipolar coupling of the last example. With its higher transition temperature one might expect that any spin glass state that exists would also have a higher freezing temperature as compared to the previous compound. This would allow measurements over a greater temperature range as well as at more accessible temperatures. One potential drawback is that the CEF ground state for the non-Kramer's ion, Tb^{3+}, has not been precisely determined, though it seems quite likely that it is a doublet or psuedodoublet which is well separated from the remaining higher energy levels (Islam, 2000).

In order to produce a site diluted, isostructural derivative of the $TbNi_2Ge_2$ compound, a suitable nonmagnetic ion must be used. This requires that (i) an isostructural, nonmagnetic compound exists, and (ii) and that the dilution process does not appreciably alter the crystalline environment, either the distance between atoms, or

the terbium point symmetry or CEF splitting. This last condition is introduced because a change in lattice parameters can be considered as an application of pressure on the system.

In the realm of the rare earth elements, there are four non-magnetic members, scandium, yttrium, lanthanum, and lutetium. Only three of these form compounds that are isostructural to $TbNi_2Ge_2$, and they are yttrium, lanthanum, and lutetium. In order to choose between these three we need to know how the lattice parameters change across the spectrum of rare earth elements for this structure. Figure 1.2 shows the lanthanide

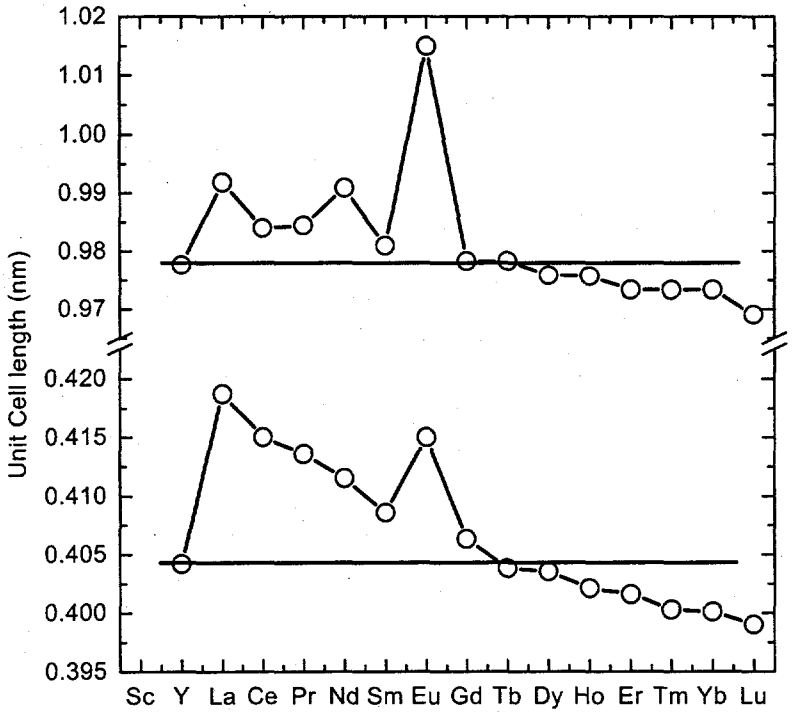

Figure 1.2 Lanthanide contraction in the RNi_2Ge_2 series of compounds. Bottom half is lattice parameter a, and top half is lattice parameter c (after Villars, 1997).

contraction for the series of compounds RNi_2Ge_2. From this it is clear that the best choice is yttrium, whose lattice parameters are almost identical to terbium. If this was not the case, it would be possible to find a mixture of lanthanum and lutetium, whose combined lattice parameters were close to those of terbium. Fortunately this was not necessary. The search for an Ising spin glass will now be confined to the $Tb_xY_{1-x}Ni_2Ge_2$ system.

In the next chapter, a brief survey is presented of the physics of rare earth magnetism and the experimental characteristics of spin glasses. This is followed by a summary of the methodology used to grow large single crystals from a flux technique in Chapter 3 and the measurement methods are outlined in Chapter 4. Chapter 5 presents the results of these measurements and discusses the trends displayed by the entire series. Chapter 6 presents the results of detailed measurements on particular dilutions that clearly demonstrate spin glass behavior.

2. PHYSICS REVIEW

2.1. Introduction

In this chapter, several pertinent concepts will be introduced that will form the basis for understanding in this study. First, a few general features of magnetic systems will be discussed, starting with a simple derivation of the Curie Law, an introduction to rare earth magnetism, RKKY interaction and the effects of CEF splitting of the J-multiplet electronic ground states. The discussion will then move on to the effects of disorder on magnetic systems. Finally the concept of a spin glass will be presented, followed by an overview of the experimental characteristics of spin glasses.

2.2. Magnetism

2.2.1. Curie Law

A common place to start the discussion of rare earth magnetism is with the derivation of the Curie law. This law describes the magnetic susceptibility as a function of temperature for a free ion. The derivation from a simple two level, s = ½, system gives a good understanding of the primary features of the physics underlining this law without going into too much mathematical detail.

The energy levels of a spin ½ system in a magnetic field are given by (Kittel, 1996)

$$U = -\vec{\mu} \cdot \vec{B} = m_s g \mu_B B \qquad (2.1)$$

where $m_s \pm ½$, g = 2 for an electron, B is the applied field, μ_B is the Bohr magneton whose value is approximately equal to the spin moment of a free electron. This gives $U = \pm\mu_B B$. The energy is minimized if the magnetic moment is parallel to the field and maximized if the moment is antiparallel to the field.

This system has only two levels and the equilibrium populations at a given temperature T are given by Boltzman statistics:

$$\frac{N_1}{N} = \frac{\exp\left(\mu_B B / k_B T\right)}{\exp\left(\mu_B B / k_B T\right) + \exp\left(-\mu_B B / k_B T\right)} \tag{2.2}$$

$$\frac{N_2}{N} = \frac{\exp\left(-\mu_B B / k_B T\right)}{\exp\left(\mu_B B / k_B T\right) + \exp\left(-\mu_B B / k_B T\right)} \tag{2.3}$$

where N_1, N_2 are the populations of the lower and upper levels and $N = N_1 + N_2$ is the total number of atoms. This is shown in Figure 2.1 The magnetization is the sum of the projection of the lower state (μ_B) and upper state ($-\mu_B$), which becomes

$$M = \left(N_1 - N_2\mu_B\right) = N\mu_B \frac{e^x - e^x}{e^x + e^x} = N\mu_B \tanh(x) \tag{2.4}$$

where $x = \mu_B B/k_B T$. for $x < 1$(low fields, high temperatures) $\tanh(x) \sim x$, and this gives

$$M = \frac{N\mu_B^2 B}{k_B T}. \tag{2.5}$$

Solving for the susceptibility we find,

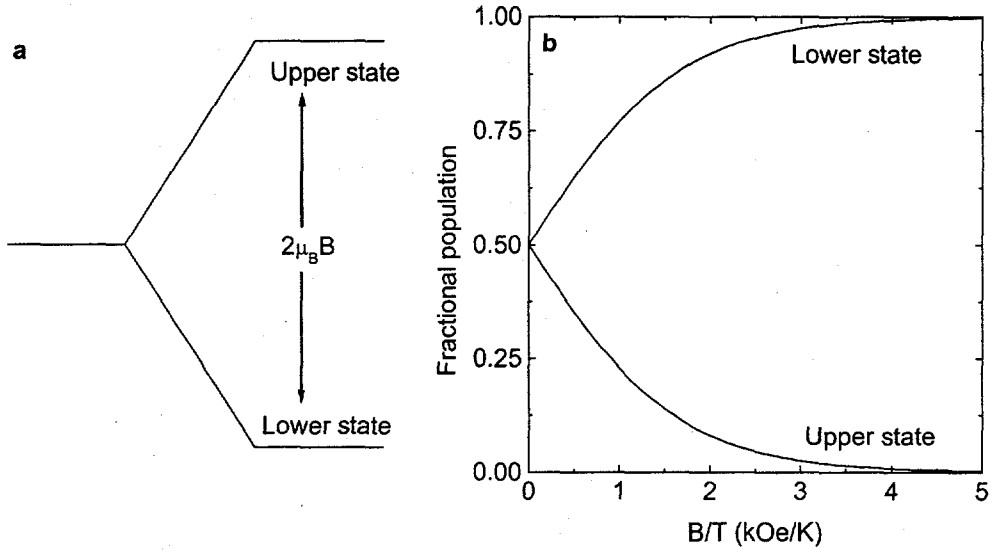

Figure 2.1. (a) energy splitting for one electron in an applied field B directed along the positive z-axis. In the low energy state the magnetic moment μ_B is parallel to the field. (b) The fractional population of a two level system as a function of temperature T and magnetic field B. The magnetization is proportional to the difference between the two curves.

$$\chi = \frac{\partial M}{\partial B} = \frac{N\mu_B^2}{k_B T} = \frac{C}{T} \tag{2.6}$$

Where C is the Curie constant for a s = ½ system. Notice that the susceptibility has a 1/T dependence.

An atom that has a total angular momentum quantum number J has 2J+1 energy levels spaced $\mu_B B$ apart. For arbitrary J, the magnetization can be calculated in a similar manner to the above example and replacing m_s with m_J. This leads to a magnetization of

$$M = Ng_J J\mu_B B_J(x) \tag{2.7}$$

where x is $g_J J\mu_B B/k_B T$ and B_J is the Brillouin function which is defined as

$$B_J(x) = \frac{2J+1}{2J} ctnh\left(\frac{(2J+1)x}{2J}\right) - \frac{1}{2J} ctnh\left(\frac{x}{2J}\right) \tag{2.8}$$

and g_J is the given by the Landé equation

$$g_J = 1 + \frac{J(J+1) + S(S+1)\, L(L-1)}{2J(J+1)} \tag{2.9}$$

For low applied fields and high temperatures (x<1), the Brillouin function can be approximated by

$$B_J(x) \cong \frac{J+1}{3J} x + O(x^3) \tag{2.10}$$

and by letting N be Avogadro's number the molar susceptibility becomes

$$\chi = \frac{\partial M}{\partial B} = \frac{N_A J(J+1)(g_J \mu_B)^2}{3k_B T} = \frac{N_A (p_{eff} \mu_B)^2}{3k_B T} = \frac{C}{T} \tag{2.11}$$

where C is the Curie constant for arbitrary J and p_{eff} is the effective number of Bohr magnetons. For low temperatures and high fields (x>>1) $B_J(x)$ approaches 1 and the magnetization is said to saturate at a value of $M_{sat} \cong N_A g J \mu_B$. Figure 2.2 shows the theoretical magnetization of a free trivalent terbium ion as a function of B/T. The values of p_{eff} and M_{sat} are dependent upon the values of J,L, and S for a given magnetic ion. In order to calculate these items one needs to know how to determine the ground state electronic configuration. For rare earth ions, this is accomplished by applying Hund's rules.

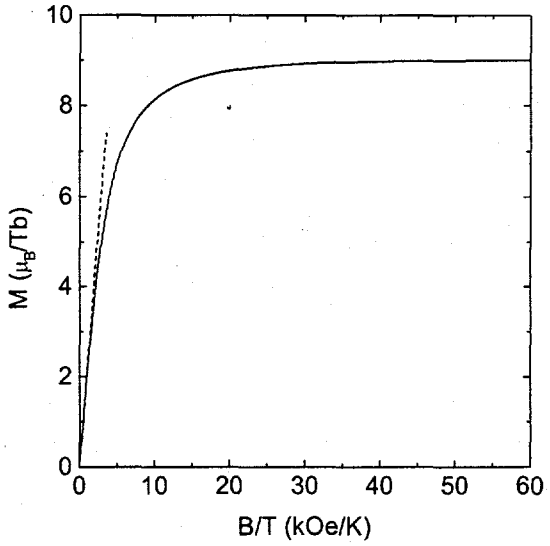

Figure 2.2. Plot of the theoretical magnetization as a function of B/T of Tb^{3+} ion (solid line) with J=6 and g_J=1.5. The saturated moment is 9 μ_B and the effective moment is 9.72 μ_B. The dashed line is the slope at low fields and high temperatures, such that $x = Jg_J\mu_B B/k_B T < 1$. It is in this region that Curie's law holds. For an applied field of 1 kOe, this inequality holds for T>0.6 K

2.2.2. Hund's Rules

In the previous section it was seen that the values of the spin angular momentum quantum number (S), orbital angular momentum quantum number (L), and the total angular momentum quantum number (J) are important for the theoretical determination of the magnetic properties of a material. In an atom with a partially filled shell with an one-electron level characterized by l. For any give l there are $2l+1$ possible values for l_z and two possible spin orientations for each l_z, giving a total of $2(2l+1)$ one electron levels (Ashcroft and Mermin, 1976). Many possible states can be made by placing n electrons into these $2(2l+1)$ levels, and if the electrons do not interact, all these states would be degenerate. Fortunately, most of this degeneracy is lifted by electron-electron Coulomb

interaction and by the electron spin-orbit coupling. In most cases the lowest lying levels after this degeneracy is lifted can be described by applying a set of rules to the combination of the quantum numbers of the individual electrons. These rules are known as Hund's rules. They are as follows (Rosenberg, 1965).

1) The lowest energy states are those in which the electrons are arranged so that as many as possible have their spins parallel to each other without violating the Pauli exclusion principle, which is only two electrons for each value of m. With $s = \pm 1/2$ depending on orientation of spin, $S = \sum s$, the combined spin momentum, is calculated.
2) The electrons with spins assigned as in 1) are distributed between the possible values of m so that $L = \sum m$, the combined orbital momentum, is a maximum.
3) These first two rules establish the values of L and S of the lowest energy states. This leaves (2L+1)(2S+1) possible lowest energy states. This degeneracy is lifted by the spin-orbit coupling. These states are characterized by their total angular momentum quantum number J, which runs in integer steps from J=|L-S| to L+S, each having a degeneracy of 2J+1. The ground state has J=|L-S| if the shell is less than half full and J=L+S if the shell is more than half full. If the shell is half full then L = 0 and J = S.

In magnetic problems, usually only the (2L+1)(2S+1) lowest states determined by the first two rules are important, the rest lying at energies too high to be of interest. Also, it is usually enough to consider only the 2J+1 lowest lying states determined by the third rule.

As an example consider terbium. Terbium has 8 electrons in the 4f shell, so that l = 3. By applying the first two rules we get

m	3	2	1	0	-1	-2	-3
s	↑↓	↑	↑	↑	↑	↑	↑

$S = \sum s = ½+½+½+½+½+½+½-½ = 6/2 = 3$
$L = \sum m = 3 +2 + 1 + 0 -1 -2 -3 + 3 = 3.$

With L = 3 and S= 3 this gives (2L+1)(2S+1) = 49 possible lowest lying energy levels. Since the 4f shell with 8 electrons is more than half full the lowest lying J level is given by J=L+S=6 with a total degeneracy of 2J+1 = 13 states. This degeneracy is lifted by the application of a magnetic field into a series of equally spaced energy levels in a similar manner as was seen in the case of the spin ½ electron in section 2.2.1. With S, L, J determined, it is now possible to determine g, p_{eff}, and M_{sat} and the expected magnetic behavior as a function of field and temperature, as was seen for the case of terbium in Figure 2.2. usually it is enough to consider only the 2J+1 lowest lying states determined by the third rule.

Table 2.1 shows the S, L, J values, g_J, p_{eff}, and M_{sat} for all the rare earths, along with approximate experimental values that are commonly found (Kittel, 1996). Notice the large discrepancies for both samarium and europium. Figure 2.3 shows the energy levels of praseodymium, samarium, europium and terbium as determined by Hund's rules. These are drawn to scale and the energy corresponding to 293 K is shown as the short vertical line coming up from the lowest level. For praseodymium and terbium there is a very large separation in energy between the two lowest energy levels and at room temperature it is appropriate to neglect the higher levels

Table 2.1. Angular momentum quantum numbers S, L, J, as determined by Hund's rules for the trivalent magnetic rare earth ions. Also presented are calculated values of the Landé (g_J), saturated moment (M_{sat}), effective moment (p_{eff}(calc)) and common experimental values of the effective moment (p_{eff}(exp)).

Ion	S	L	J	g_J	M_{sat}	p_{eff}(calc)	p_{eff}(exp)
Ce	0.5	3	2.5	0.857	2.14	2.54	2.4
Pr	1	5	4	0.800	3.20	3.58	3.5
Nd	1.5	6	4.5	0.727	3.27	3.62	3.5
Pm	2	6	4	0.600	2.40	2.68	--
Sm	2.5	5	2.5	0.286	0.71	0.84 (1.58)	1.5
Eu	3	3	0	--	--	-- (3.46)	3.4
Gd	3.5	0	3.5	2.000	7.00	7.94	8.0
Tb	3	3	6	1.500	9.00	9.72	9.5
Dy	2.5	5	7.5	1.333	10.00	10.64	10.6
Ho	2	6	8	1.250	10.00	10.61	10.4
Er	1.5	6	7.5	1.200	9.00	9.58	9.5
Tm	1	5	6	1.167	7.00	7.56	7.3
Yb	0.5	3	3.5	1.142	4.00	4.54	4.5

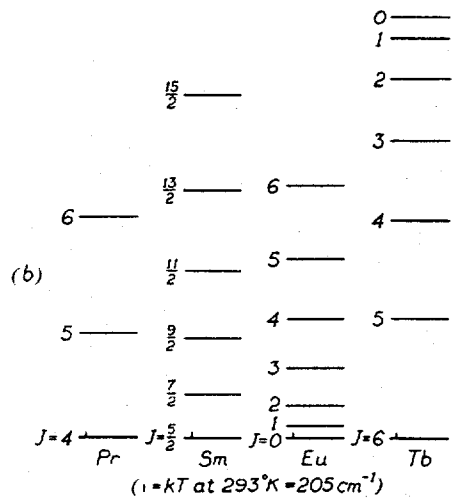

Figure 2.3. The energy levels of four rare earth ions, drawn to scale with the energy corresponding to 293 K also shown. Each of these levels are 2J+1 degenerate (after Rosenberg, 1965).

as they are not appreciably populated at room temperature. On the other hand, for samarium and europium, the energy levels are more closely spaced and at room temperature the second lowest energy level has an appreciable population which can not be neglected. Values of p_{eff} have been calculated for these two elements taking into account this population of excited states by Van Vleck and these values are shown in parenthesis in Table 2.1 (Rosenberg, 1965).

2.2.3. RKKY Exchange Interaction

The previous discussion is valid for non-interacting ions in free space. The results are modified by two effects due to the placement of the ions in a crystalline environment. The first of these effects is the interaction of the magnetic moment of one ion with the moments of the other ions present in the crystal. The other effect is caused by internal electric fields in the crystal created by the surrounding structure and neighboring atoms. The former effect will be discussed briefly in this section and the latter will be discussed in the next section.

For systems with interacting moments, the susceptibility may deviate from the Curie law. There are two primary modes for interaction to take place between magnetic moments. The first is a direct exchange interaction due to a spatial overlap of electronic wave functions. Figure 2.4 shows the radial densities of the electrons in gadolinium. The 4f electrons are much more strongly localized than the $5s^2$, $5p^6$, and $6s^2$ shells. The overlap between 4f shells on neighboring rare earth ions will be extremely small and therefore the possibility of a direct exchange between the ions will be highly reduced. In

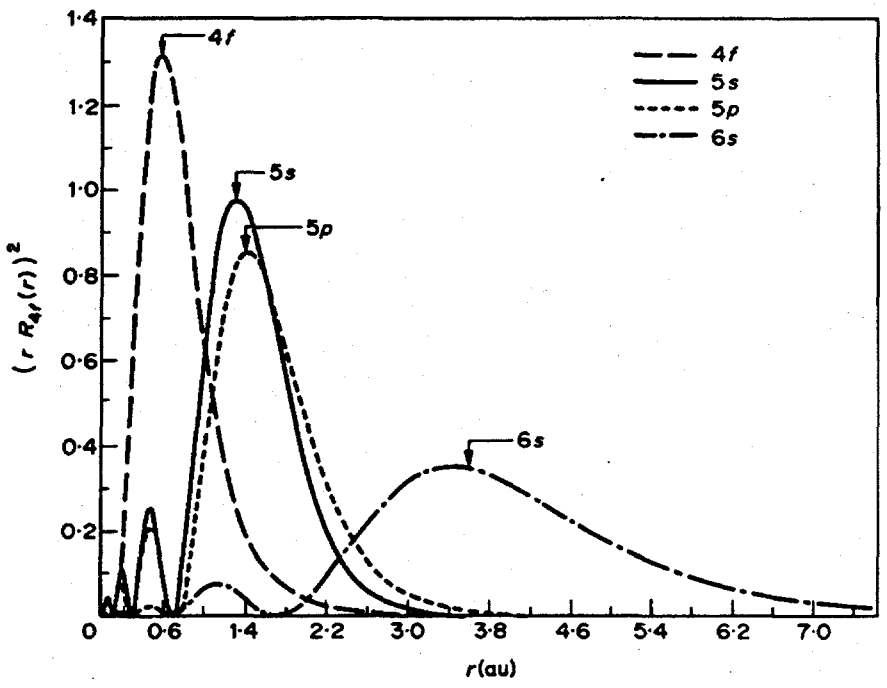

Figure 2.4. Radial densities of the electrons of Gd^{3+} from Hartree-Fock calculations (after Taylor and Darby, 1972).

a metal the primary interaction between the magnetic moments on the ions is then the indirect exchange.

This indirect exchange interaction arises when the localized spin of the 4f electrons interacts with the spin of the conduction electrons. This interaction polarizes the conduction electrons around the ion with respect to the ion's spin angular momentum. For example, the polarization is parallel between the localized 4f electrons and the 5d conduction electrons. For the rare earths from cerium to europium the spin angular momentum is oriented antiparallel to the orbital angular momentum (J = |L-S| for electron shells less than half full, Hund's third rule) and this leads to a polarization of the conduction electrons that is antiparallel to the magnetic moment. For gadolinium to

ytterbium the spin momentum is parallel to the orbital momentum and the polarization is parallel to the magnetic moment. It was shown by M. A. Ruderman, C. Kittel, T. Kasuya, and K. Yosida (RKKY) that this spin polarization alternates in sign with increasing distance from the ion and a frequency proportional to the Fermi wavevector, k_f, and decreases in magnitude approximately as the distance cubed (Hurd,1975). This interaction can be considered as a magnetic scattering event, where the scattering of a conduction electron from a magnetic ion is dependent on the spin configuration. This conduction electron then interacts with another magnetic ion and the scattering is again dependent on the local spin configuration. In this way the two magnetic ions are able to interact in a cooperative manner.

The oscillatory as well as the long range nature of the RKKY interaction, as this type of interaction has come to be known, can couple spins in either a ferromagnetic or an antiferromagnetic manner depending on the ions' separation and the shape of the Fermi surface. This can lead to many diverse magnetic orderings and RKKY exchange interaction's sensitivity to the morphology of the Fermi surface can profoundly affect the ordering wavevector, often leading to incommensurate magnetic structures. At high temperatures, the thermal energy of the atoms is greater than energy of the interaction and they do not order. At lower temperatures, it is possible for the energy of the interaction to overcome the thermal agitation and the ions are able to enter into an ordered state.

The Curie law is based on the premise of the possible spin states being populated in a thermally random manner. The presence of exchange interactions creates a preference for particular spin states. At high applied fields and low temperatures the

Curie law says that the majority of (and at absolute zero, eventually all) of the spins will be aligned with the field. A ferromagnetic interaction is also tending to align the moments with the field and it is not unreasonable to expect that a total alignment of the moments will occur at a temperature above absolute zero, or make the effective temperature less than the actual temperature. Conversely, an antiferromagnetic exchange interaction is tending to create a state in which the fractional population of spin up and spin down states are equal, which for the Curie law holds true at very high temperatures and low fields. So again it is not unreasonable to expect that in this case the interactions will retard the saturation of the moment, creating an effective temperature greater than the actual temperature.

This can be simply seen by applying a mean field approximation, where it is assumed that each magnetic ion experiences an internal field due to the exchange interactions. This field is proportional to the magnetization and is given by (Kittel,1996)

$$B_E = \lambda M , \tag{2.12}$$

where λ is independent of temperature and represents the exchange interactions. In this manner each spin will "see" the average magnetization of all the other magnetic ions. In the paramagnetic region (high temperatures) the magnetization (M) can be written as

$$M = \chi_p (B_a + B_E), \tag{2.13}$$

where B_a is the applied field. According to the Curie law (Equation 2.6) the paramagnetic susceptibility is given by χ_p=C/T. Combining these three equations leads to

$$M = \frac{C(B_a + \lambda M)}{T}. \tag{2.14}$$

Solving for M and the susceptibility, Equation 2.11 becomes

$$M = \frac{CB_a}{(T - \lambda C)} \tag{2.15}$$

$$\chi = \frac{\partial M}{\partial B_a} = \frac{C}{(T - \lambda C)} = \frac{C}{(T - \theta)} \tag{2.16}$$

where θ is the Weiss temperature (Kittel, 1996). Equation 2.13 is known as the Curie-Weiss law. θ is proportional to the exchange interaction represented by λ and causes the effective temperature (T-θ) to be less than the actual temperature, as was expected. Similar arguments can be applied to the antiferromagnetic case, except that now the magnetic ion would see a negative field (B_E) due to the other magnetic ions in the material. This means that λ is negative and leads to a negative Weiss temperature (θ). This negative θ causes the effective temperature (T-θ) to be more than the actual temperature, thereby resisting the tendency of the magnetization to saturate as the temperature is lowered.

2.2.4. The Ordered State

When the temperature is low enough, the energy of the exchange interaction is larger than the thermal averaging and the magnetic system enters into long range order. In the paramagnetic region, the orientation of any one magnetic moment is independent of the orientation of the other moments in the system, and one can talk about the energy state or level of a particular ion. In the ordered state, the orientation of a particular moment is determined by the orientation of all the others.

As mentioned previously, The RKKY exchange interaction is oscillatory in sign and is highly influenced by the shape of the Fermi surface. This can lead to many different types of spatial ordering. A commensurate magnetic structure has a spatial ordering, or wavevector, that is related to the underlying crystal structure. An incommensurate structure is one whose wavevector is not related to the crystal lattice. Often intermetallic magnetic systems can exhibit both of these types, such as $TbNi_2Ge_2$, which has an incommensurate structure below 16.8 K and a commensurate structure below 9.3 K. The ordered state may also be ferromagnetic, antiferromagnetic or somewhere in between. A ferromagnetic structure is one where all the spins point in the same direction, with the same saturation value. In an antiferromagnetic structure there is a unit cell in with an equal number of the moments pointing down and pointing up, or more strictly the value of the saturated magnetization directed down is equal to the that which is directed up. This unit cell is then repeated throughout the crystal. This can lead to a wide variety of different antiferromagnetic structures depending on the magnetic unit cell.

The transition to a magnetically ordered state is characterized by a transition temperature, the Curie temperature, T_C, for ferromagnets, and the Neél temperature, T_N, for antiferromagnets. This transition can be marked by a lambda-peak anomaly in specific heat measurements at the transition temperature. There are also very strong effects seen in susceptibility measurements and in resistivity measurements. There have been several theoretical studies linking these effects to the specific heat anomaly. It has been shown that the peak seen in $d(\chi T)/dT$ as a function of temperature is proportional to

the specific heat close to T_N for an antiferromagnet (Fisher, 1962), and that the peak seen in $d\rho/dT$ is also proportional to the specific heat close to T_N (Escorne, 1981).

2.2.5. Crystal Electric Field

In the previous section modifications to the Curie law due to the interaction of the magnetic ions with each other were examined. In this section a modification to the Curie law due to internal crystalline electric fields will be discussed.

The crystalline electric field (CEF) arises from the presence of nearby atoms in a lattice and is derived from the Coulomb repulsion between the electrons in a shell and the charges on neighboring ions (Hurd,1975). These fields are nonuniform electrostatic fields that reflect the symmetry of the ion's environment. The repulsion due to the CEF may be strong enough to disrupt the ground state of the magnetic ion as determined by Hund's rules. This means that some electrons in the unfilled shell may find it more energetically favorable to relocate to other m_l orbitals that have shapes that will keep them further away from the neighboring ions, thus changing the electron ground state configuration.

The 2J+1 degenerate states of a rare earth ion as determined from Hund's rules can be split into several levels dependent on the actual symmetry of the environment around the magnetic ion. This is seen in Figure 2.5 for a magnetic ion with L = 3 and S = 3/2 where the Hund's rule ground state J=3/2, which is fourfold degenerate, is split into two doublets. The energy splitting due to the CEF is not necessarily uniform and this has consequences to Curie's law. The derivation of Curie's law assumed an uniform splitting between all the levels when in a magnetic field. With the uneven splitting due to the

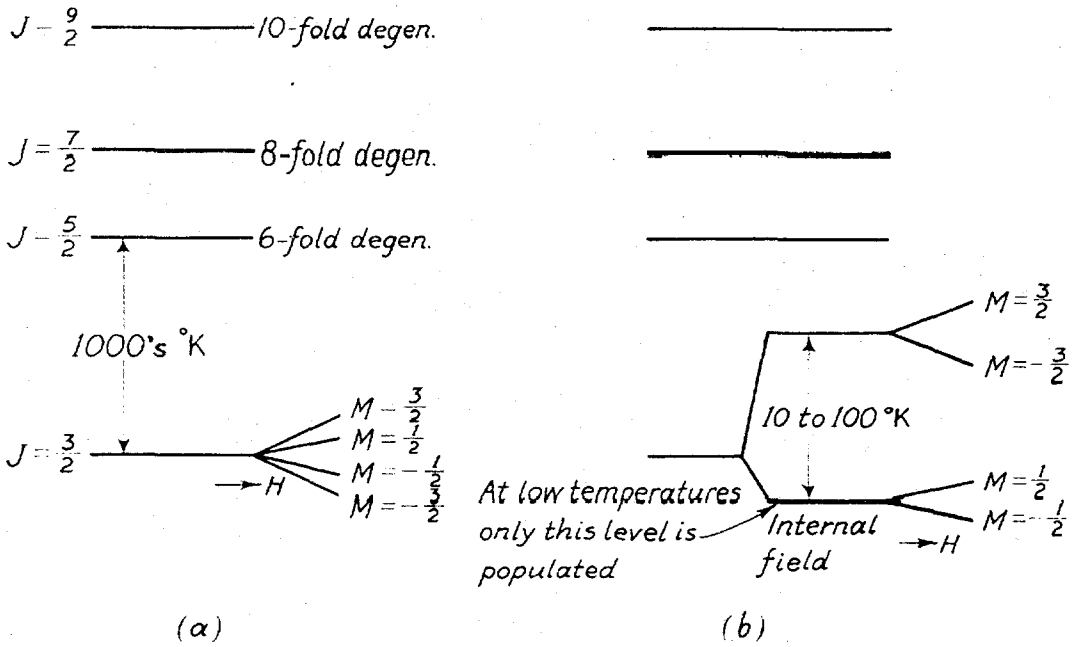

Figure 2.5. The energy levels of an ion with L=3 and S=3/2. The several different possibilities of J running from L-S to L+S in integer steps are separated by energies corresponding to 1000's of degrees K, so that only the lowest level, J=3/2 is appreciably populated. In (a) the fourfold degeneracy of the J=3/2 ground state is removed by a magnetic field H. In (b) the crystal electric field (CEF) splits this level into two doublets, of which only the lower one will be appreciably populated at low temperatures. The degeneracy of these doublets are also removed by the application of a field H. (after Rosenberg, 1965)

CEF, Curie's law will not hold except at temperatures which are sufficiently high compared to the splitting energy. At these higher temperatures the effect of the split CEF levels can be taken into account by means of a correction term to the next order in 1/T (Rosenberg,1965). The Curie law then becomes

$$\chi = \frac{C}{T}\left(1 - \frac{\Delta}{T}\right) \approx \frac{C}{T\left(1 + \Delta/T\right)} = \frac{C}{(T + \Delta)} = \frac{C}{(T - \theta)} \qquad (2.17)$$

where Δ is a correction term to account for the CEF effects and the last step was performed to make the equation look like the Curie-Weiss law (Equation 2.16).

The value of θ in this case will be dependent upon the direction of the applied magnetic field. Since the CEF favors particular m_l values, this will cause the magnetic moment to have a preferential orientation with respect to the crystalline lattice. If a magnetic field is applied parallel to this preferred direction, then the CEF will be aiding in aligning the moments with the field. This is similar to the case with ferromagnetic interactions and therefore it is not unreasonable to expect that θ will be positive. If the field is applied in a direction contrary to the CEF preferred direction, then the crystalline electric fields will be tending to prevent the moments from aligning with the field and therefore θ should be negative.

For the rare earths, the preferential alignment of the moments with respect to the crystalline environment can be extreme and depends on how the moments are constrained. The moments could be constrained to lie along a particular axis, creating an Ising system. This is the case with $TbNi_2Ge_2$. The moments can also be constrained to lie within a particular plane, for example $DyAgSb_2$ (Myers, 1999). There are also possibilities falling between these two extreme cases. A special case is that of gadolinium. Gadolinium has a half full orbital with seven electrons. This gives a value for the total orbital angular momentum (L) of zero, by Hund's second rule. This leads to a spherical orbital which is not altered by the CEF and therefore the ground state 2J+1 degeneracy remains unsplit. Therefore, the magnetic moment will be unconstrained and will be able to point in any direction. This is a Heisenberg system.

It can be shown (Boutron,1973; Dunlap, 1983), that for a tetragonal system, such as $TbNi_2Ge_2$, the effects of CEF splitting can be removed from magnetization data, at

least to first order, by performing a polycrystalline average of the susceptibility (or directly measuring randomly oriented polycrystalline samples) , defined as

$$\chi_{poly} = \frac{2\chi_{ab} + \chi_c}{3}. \qquad (2.18)$$

Here, χ_c is the susceptibility with the field parallel to the c-axis of the crystal and χ_{ab} is the susceptibility with the field applied perpendicular to the c-axis. By applying the Curie-Weiss law to χ_{poly} it is possible to extract θ_{poly}, which more accurately reflects the effects of the RKKY interaction.

One effect that is characteristic of RKKY mediated interactions is the scaling of quantities that are dependent upon the value of the exchange interaction with what is called the de Gennes factor. This factor is defined as

$$dG = (g_J - 1)^2 J(J+1), \qquad (2.19)$$

where g_J is the Landé g factor and J is the total angular momentum determined by the third Hund rule. Two important quantities that scale with dG are the transition temperatures between the paramagnetic state at high temperatures and the long-range ordered state at low temperatures, T_C or T_N, and the polycrystalline Weiss temperature, θ_{poly}.

2.3. What is a Spin Glass?

2.3.1. Definition

What is a spin glass? A spin glass may be defined as a random (or aperiodic), mixed-interacting, magnetic system characterized by a random but co-operative freezing

of spins at a well-defined temperature T_f. Below this temperature a highly irreversible, metastable frozen state exists without long-range spatial magnetic order (Mydosh, 1993). The name spin glass was coined via analogy to structural glasses that freeze with no long range atomic order. There are three important statements in this definition: randomness, mixed interactions, and a co-operative freezing. The randomness is created either by a random site occupancy between magnetic and nonmagnetic elements or by a random bond system where the bonds between well ordered magnetic sites are randomly distributed. It may also be accomplished by an aperiodic separation of the spins, which would hold for quasicrystalline systems, which are believed to be atomically well ordered. The mixed interactions are needed to produce a competition between ferromagnetic and antiferromagnetic interactions in order to produce frustration of the moments. This frustration plays a large role in the co-operative nature of the frozen metastable state. Thirdly, the transition is a co-operative one. Roughly speaking this means that all the spins freeze in unison, and it is no longer meaningful to talk about the energy states of the individual spins but rather the energy of the configuration of spins as a whole.

What happens to the spins in a spin glass as the temperature is reduced to T_f? A simple picture will be presented here to provide some physical insight into the problem. At very high temperatures the spins are purely paramagnetic and obeying the Curie-Weiss law as discussed earlier. At lower temperatures but still above T_f, the interaction between spins will give rise to locally correlated clusters. These clusters will also be paramagnetic and exhibit Curie-Weiss behavior. This formation of clusters is a

consequence of the randomness and mixed interactions. As the temperature approaches T_f more spins are involved in the clustering as the disorder due to temperature is removed. The spin system seeks a ground state configuration based on its particular distribution of spins and exchange interactions. This generates a set of random alignment axes into which the spins or clusters can freeze. Here frustration plays its role and a multidegenerate array of ground states is available to the system. Since there is a spectrum of energy differences between frozen states, the system may become trapped in a metastable state of higher energy. Below T_f, unusual magnetic behavior appears which is related to the glassy nature of the frozen state. In this state no long range magnetic order is formed. The following section will provide an overview of a few of the main experimental features seen in spin glasses. It will be against these features that the low terbium concentration region of this study will be compared.

2.3.2. Phase Diagrams

Before looking at specific characteristics of spin glasses, it is instructive to take a quick look at the variety of magnetic behavior available by changing the concentration of the magnetic ion present in the material. Figure 2.6 shows a schematic of the concentration regimes that are possible in a dilute magnetic alloy. At the very dilute concentration region there are isolated impurity-conduction electron couplings that result in the Kondo effect for some hybridizing systems. The next most dilute region can be described by interacting single spins without any clustering. The measurable properties, T_f as well as critical fields, can be described through a mean field concentration scaling of the parameters T/x, and H/x, where x is the concentration of magnetic ions. Following

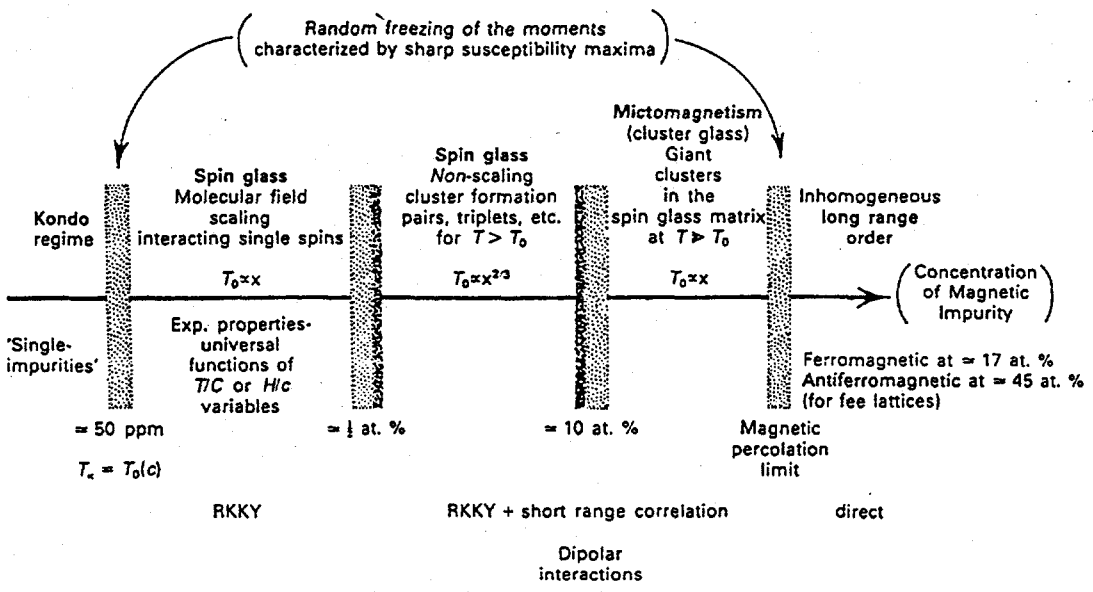

Figure. 2.6. Various concentration regimes for a canonical spin glass illustrating the different types of magnetic behavior that exist (after Mydosh, 1993).

this region is a region where the scaling breaks down and T_f follows a more closely to a $x^{2/3}$ relation. In this region, clusters of pairs and triplets (and higher) of spins are formed and begin to influence the system. At concentrations greater than 10 % these clusters dominate the magnetic properties and the region is called mictomagnetism to emphasize the anomalies generated by these very large clusters. Finally a percolation limit is reached for long range, inhomogeneous ferro- or antiferromagnetic order with a well defined transition temperature.

The term spin glass will be used to refer to the region from the dilute limit almost up to the percolation limit. This avoids the unnecessary complications of having three or more types of spin glass regimes. The different regions seen in Figure 2.6 are not separated by sharp boundaries, rather there is a gradual transition from one to another

(Mydosh, 1993). Figure 2.7 shows a general temperature versus concentration phase diagram for a dilute magnetic alloy. T_K is the average Kondo temperature which decreases with concentration. The spin glass region first appears for $T_f < T_K$. Above T_K, the spin glass region has first a linear then with a less than linear dependence of T_f on concentration. When the percolation limit is passed there is the nearly linear increase of Curie or Neel temperatures with concentration. Now that the region of spin glass properties has been outlined some of the experimental properties can be studied.

2.3.3. DC Susceptibility

At high temperatures the system is paramagnetic and follows the Curie-Weiss law. As the temperature is lowered the susceptibility deviates from this behavior. This is due to the formation of clusters and is most clearly seen in plots of $1/\chi$ as a function of temperature. This is shown in Figure 2.8 for several concentrations of *Au*Fe (Morgownik, 1983). The direction of the deviation is dependent on the type of clustering,

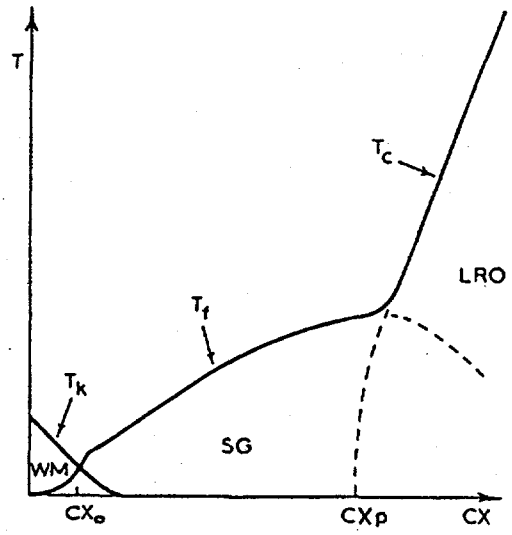

Figure 2.7. A general temperature-concentration phase diagram for a dilute magnetic alloy (after Mydosh, 1993).

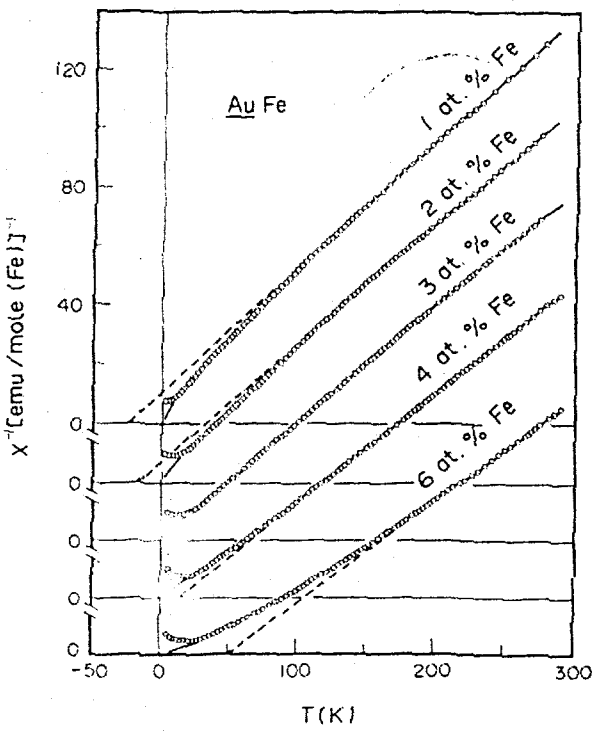

Figure 2.8. $1/\chi$ for 5 different concentrations of Fe in Au. The dashed lines are linear extrapolations of Curie-Weiss behavior from high temperature. θ is determined by where lines intercepts the x axis. Notice the deviations from C-W at low temperatures. For antiferromagnetic clustering, corresponding negative θ, there is a negative deviation. For ferromagnetic clustering, positive θ, the deviations are positive. (after Morgownik, 1983)

ferro- or antiferromagnetic. This clustering is determined by the value of the exchange interaction which is reflected in the Weiss temperature θ. For this particular material θ varies from negative to positive as the concentration increases. It should be noted that although *Au*Fe is a classic Kondo material, the Kondo effect occurs at iron concentrations of less than 400 ppm or 0.04 %. Thus the effects seen in Figure 2.8 are not manifestations of the Kondo effect.

At temperatures spanning T_f and low applied fields a striking difference is seen in the dc magnetization as a function of temperature depending on whether the sample is cooled in zero field (zfc) or in a small but non-zero field (fc). This is seen in Figure 2.9 which shows the zfc and fc magnetization for two concentrations of *Cu*Mn in an applied field of 6 Oe. The fc magnetization is fully reversible. The zfc magnetization is not and is highly sensitive to the rate of temperature increase, dT/dt (Mydosh,1993). These effects occur even though the field is so small, $\mu_B H << k_B T$, and clearly demonstrates the existence of a multidegenerate groundstate. The onset of these irreversibilities cleanly defines T_f.

The freezing temperature T_f is strongly influenced by magnetic field and decreases as the field increases. The Sherrington-Kirkpatrick (SK) model is a mean field theory for Ising spin glasses, and in this model a phase boundary has been proposed by de

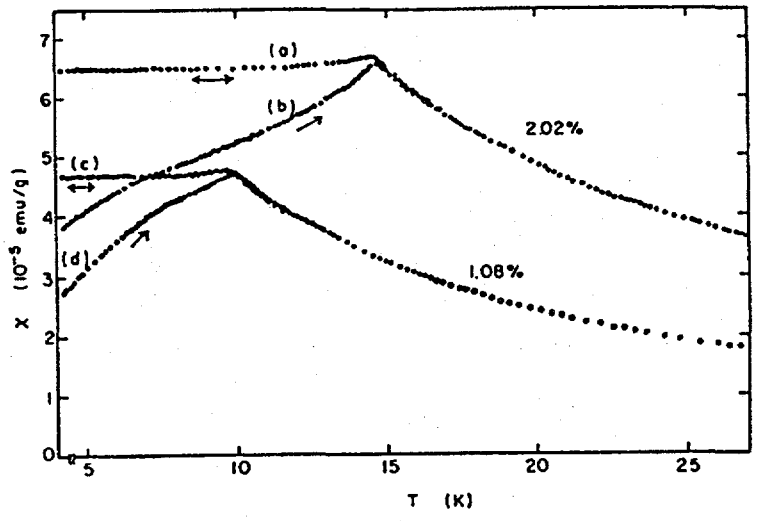

Figure 2.9. Field cooled [(a) and (c)] and zero field cooled [(b) and (d)]magnetization for *Cu*Mn at 1 and 2 % as a function of temperature. (after Mydosh, 1993)

Almeida and Thouless which is called the AT line (de Almeida, 1978). This line is given by the equation

$$H = A\left(1 - \frac{T_f(H)}{T_f(0)}\right)^{3/2}, \qquad (2.20)$$

where the coefficient A is a function of the averaged exchange interaction, J_0/J. This theory is developed for Ising spin glasses and this behavior of the freezing temperature is universally seen for Ising spin glasses and it is seen for non-Ising spin glasses as well (Katori, 1994).

From this discussion there are three characteristics of spin glasses that are seen in dc magnetization measurements. One of these is the deviation from Curie-Weiss behavior at temperatures above T_f, which reflects the creation of clusters and short range correlations with in the random system. The spin glass state can be thought of as being built from these clusters. Another signature of spin glasses seen from these measurements is the onset of magnetization irreversibilities at the freezing temperature dependent on the temperature and field history of the system. The freezing temperature is also dependent on the strength of the applied field and it follows the AT line derived from a mean field theory for Ising spin glasses.

2.3.4. AC Susceptibility

The ac susceptibility reveals several features that are held in common among many spin glass systems. Figure 2.10 shows the real and imaginary components of the ac susceptibility as a function of temperature for $Eu_{0.2}Sr_{0.8}S$ at different frequencies. The real part, χ', has a sharp peak at the freezing temperature. The high temperature

paramagnetic tail overlaps with that determined from dc measurements. On low temperature side χ' extrapolates to a finite value at T=0 and can be fit by

$$\chi'(T) = \chi'(0) + bT^n \qquad (2.21)$$

where for metallic spin glasses n is approximately 2 and a ratio of $\chi(0)/\chi(T_f) \sim 0.5\text{-}06$ is roughly found (Mydosh, 1993). These measurments have been applied to many spin glass systems which show the same general characteristics.

Figure 2.10 also shows the imaginary component of the ac susceptibility. For a spin glass there is a sudden onset of χ'' near T_f. This onset means that there are relaxation processes that are affecting the measurement and causing absorption. Effects like this are not seen in conventional magnetic transitions. From χ'', T_f can be determined from the maximum slope in this sudden onset.

Notice in Figure 2.10 that the peak in χ' moves to higher temperatures as the frequency increases. Higher frequencies are frozen out at higher temperatures. This is like a real glass getting more viscous as T_f is approached and is a manifestation of the system slowing down. For a frequency variation of about 10^3, T_f is increased by a few percent. It might be thought that this frequency dependence can be analyzed by applying the Arrhenius law for thermal activation,

$$\omega = \omega_0 \exp\left(-E_a / k_B T_f\right) \qquad (2.22)$$

where E_a is an activation energy and ω is the driving frequency of the measurement. For *Cu*Mn at 4.6 % E_a=4400 K and $\omega_0=10^{200}$ Hz. Results like this are unphysical, since this activation energy is several orders of magnitude greater than the ordering temperature

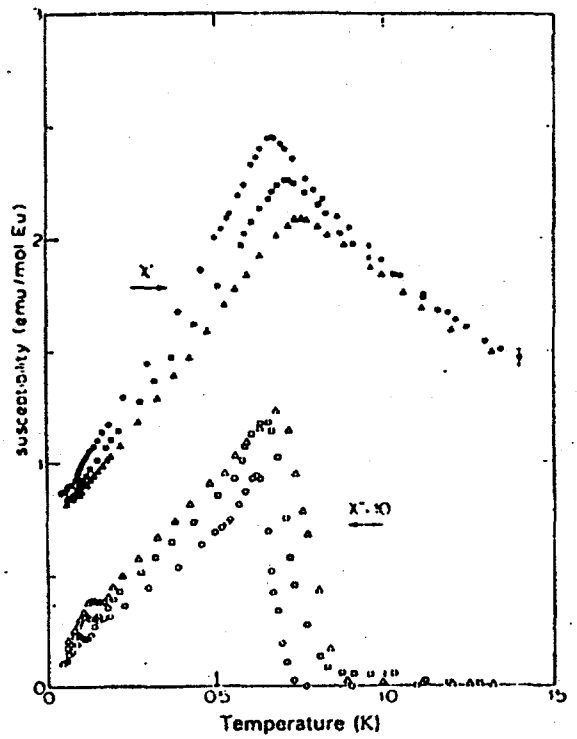

Figure 2.10. Temperature dependence for the real, χ' (solid symbols), and imaginary, χ'' (open symbols), components of the ac susceptibility for $Eu_{0.2}Sr_{0.8}S$ for frequencies of 10.9 Hz (circles), 261 Hz (squares), and 1969 Hz (triangles) with an ac driving field of 0.1 Oe. (after Mydosh, 1993)

and even the melting temperature and the frequency is very large compared to spin fluctuations, and are due to the very small change in T_f with frequency, and distinquishes a spin glass from a superparamagnet for which the Arhennius law does hold and gives physically realistic values of E_a and ω. This shows that there is more involved than a simple energy barrier blocking and thermal activation in a spin glass transition (Mydosh, 1993).

Another method used to analysis this frequency shift is to apply the Vogel-Fulcher law, which was derived to explain the viscosity of supercooled liquids and real glasses. For this case it can be written as,

$$\omega = \omega_0 \exp\left(-E_a / k_B\left(T_f - T_0\right)\right), \tag{2.23}$$

where a new parameter, T_0, is used and for real glasses is referred to as the ideal glass temperature. With three parameters the fit is naturally much better and produces more realistic values. For *Cu*Mn with 4.6 % values are obtained of $\omega_0=1.6\times10^8$ Hz, $E_a=11.8$ K, and $T_0=26.9$ K, which is less than the freezing temperature of this compound of 27.5 K for low frequencies. Currently there is no precise physical meaning for T_0 in spin glasses. Results like this are again typical for spin glasses.

2.3.5. Non-Linear Susceptibility.

In spin glass research, an important, relatively new parameter is the nonlinear susceptibility. According to theory, this parameter should exhibit the critical susceptibility divergence and exponent of a spin glass (Mydosh, 1993). There are two alternative but related definitions of the nonlinear susceptibility, χ_{nl}.

In the first definition, start by expanding the magnetization as a function of odd powers of the applied field H then calculate the susceptibility,

$$M(H) = a_1 H - a_3 H^3 + a_5 H^5 - a_7 H^7 + O\left(H^9\right) \tag{2.24}$$

$$\frac{\partial M(H)}{\partial H} = \chi = a_1 - a_3 H^2 + a_5 H^4 - a_7 H^6 + O\left(H^8\right). \tag{2.25}$$

Now one can measure the magnetization as a function of field or the ac susceptibility as a function of field. By fitting the above equations the nonlinear terms, a_3, a_5, a_7, and higher can be extracted.

In the second method, an ac driving field, h, is applied at a frequency, ω. A similar expansion is then performed but this time as a function of odd frequency harmonics, 3ω, 5ω, ... This leads to a $M(\omega)$ of the following form,

$$M(\omega) = \sum_{k=odd} [\Theta'_k \cos(k\omega t) + \Theta''_k \sin(k\omega t)], \tag{2.26}$$

where

$$\Theta'_1 = \chi'_1 h + \frac{3}{4}\chi'_3 h^3 + \frac{5}{8}\chi'_5 h^5 + \ldots$$

$$\Theta'_3 = \frac{1}{4}\chi'_3 h^3 + \frac{5}{16}\chi'_5 h^5 + \ldots \tag{2.27}$$

$$\Theta'_5 = \frac{1}{16}\chi'_5 h^5 + \ldots$$

and similarly for the imaginary component χ''. If it is assumed that the driving field h is small (i.e. keeping only leading terms for each harmonic), then the magnetization becomes,

$$M(\omega) = \chi'_1 h \cos\omega t + \frac{1}{4}\chi'_3 h^3 \cos 3\omega t + \frac{1}{16}\chi'_5 h^5 \cos 5\omega t + \ldots \tag{2.28}$$

and similarly for the imaginary component. Now one can measure the various parameters χ'_1, χ'_3, χ'_5, and higher.

Many different techniques have been used to determine χ. Unfortunately there are practical difficulties associated with each of them. For the field expansion the rather

large applied fields that might be used will affect the spin glass transition. This was seen in the discussion of the AT line. This disrupts the critical phenomenon. For the harmonic expansion the relaxation times quickly become larger than ω^{-1} and this also influences the critical behavior.

Regardless of these difficulties, χ_{nl} is still crucial in establishing the properties of the phase transition in spin glasses. This is illustrated in Figure 2.11 where χ'_3 for *Ag*Mn (0.5%) with a T_f = 2.945 K is plotted versus reduced temperature $(T-T_f)/T_f$. A log-log scale is used so that the slope is proportional to the critical exponent. It appears that there is a power law behavior with a critical exponent of 2.1 (Lévy, 1988). But note that χ'_3

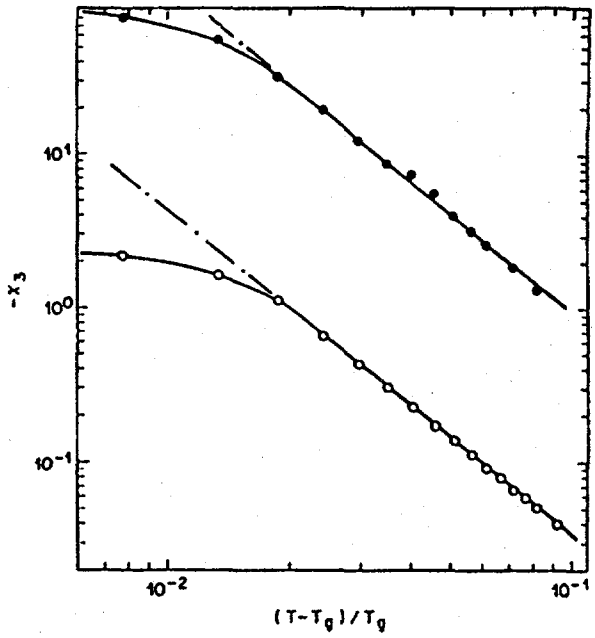

Figure 2.11. Temperature dependence of χ'_3 above T_f (T_g is the same as T_f, the freezing temperature of the spin glass). Sample of *Ag*Mn with 0.5 % was measured at 10^{-2} Hz in static fields of 0 Oe (open circles) and 90 Oe (closed circles) as a function of reduced temperature. The slope is the same in both curves and gives a critical exponent of 2.1. (after Lévy, 1988)

starts to round off below 2×10^{-2} in reduced temperature. This means that one cannot approach too close

to T_f before the transition is smeared out, probably because the distribution of relaxation times becomes too great and the system drifts out of equilibrium. In usual phase transitions, these divergences can be followed as close as 10^{-4} in reduced temperature to the transition. This shows that spin glasses do not display an ordinary phase transition (Mydosh, 1993). Even without the critical exponents, the sharp peak of $\chi_{nl}(T)$ at T_f distinguishes a spin glass freezing transition from a progressive freezing of the moments of superparamagnetic clusters (Bitoh, 1996). This is seen in Figure 2.12 which shows the nonlinear susceptibilities, χ_3, for the spin glass system $Au_{96}Fe_4$ and the superparamagnetic system $Cu_{97}Co_3$.

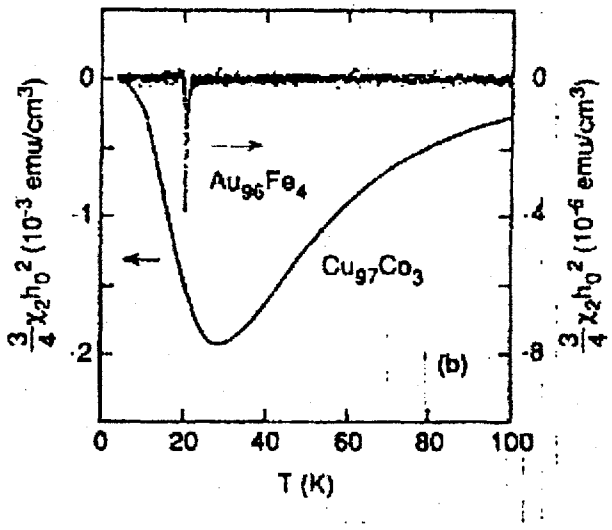

Figure 2.12 Nonlinear susceptibilities for the spin glass system $Au_{96}Fe_4$ and the superparamagnetic system $Cu_{97}Co_3$ (Bitoh, 1996).

2.3.6. Remanence and Relaxation

In the low temperature region where $T<T_f$ there are several properties which are highly dependent upon the relaxation processes of the frustrated spin glass state. These processes cause the magnetization to have a time dependence. These relaxation processes are an extensive problem and it is beyond the scope of this work to study them in detail. There are a couple measurements, though which are useful in demonstrating these effects and these will be considered in this section.

The first of these effects is the remanent magnetization. This is the magnetization that a spin glass maintains after an applied field is turned off. This remanent magnetization is formed because the applied field induces the spin glass to enter a metastable state that has a small net ferromagnetic component. When the field is reduced to zero, this small moment slowly dissipates. There are two types of remanence depending on the precise temperature and field history of the measurement. The first is the isothermal remanent magnetization (IRM). To measure the IRM a spin glass is cooled through T_f in zero applied field. Then a field is applied, a wait time, t_w, is allowed to elapse and then the field is returned to zero and the IRM is measured. The second type of remanence is the thermoremanent magnetization (TRM). Here a field is applied at temperatures above the freezing temperature. The spin glass is then cooled through the freezing transition and a wait time, t_w, is again allowed to elapse. The field is then returned to zero and the TRM is measured. The results of this type of measurement are seen in Figure 2.13. Here the TRM and IRM for a 0.5 % dilution of iron into gold, with a

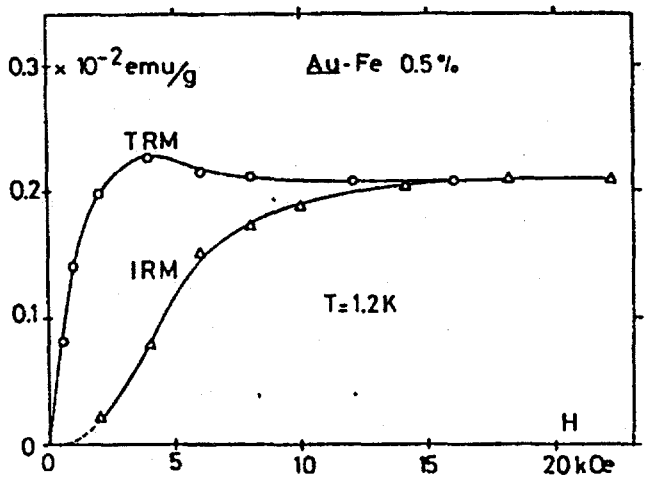

Figure 2.13. Field dependence of the TRM and IRM of AuFe 0.5 % at T=1.2 K (after Thoulence, 1974).

T_f of 5.2 K, are displayed (Tholence, 1974). This shows that the TRM saturates at lower fields than that of the IRM. These results are common among the spin glasses.

The relaxation processes that are present in the spin glasses are highly dependent on the wait time, t_w. The relaxation processes can be discerned in several ways. One can zero field cool the spin glass, wait a time, t_w, and then turn on a small field and track the magnetization as it increase with time. Another method is to track the remanent magnetization as it decreases with time. Many functional forms have been suggested to describe the relaxation of the magnetization. One popular form is the stretched exponential,

$$M(t) = M_0 \exp\left[-\left(t/t_p\right)^{1-n}\right], \qquad (2.29)$$

where M_0 and t_p are functions of the wait time and temperature and n is a function of temperature only. If n=0 then this becomes the Debye, single time constant exponential relaxation. If n=1 then M(t) is a constant and so n critically determines the exact relaxation rate.

The results of measuring the relaxation of the TRM of CuMn (0.5 %) are shown in Figure 2.14 for two different t_w (Mydosh, 1993). The thick solid lines are the experimental data, the thin solid lines are a fit to the stretched exponential. Equation 2.29

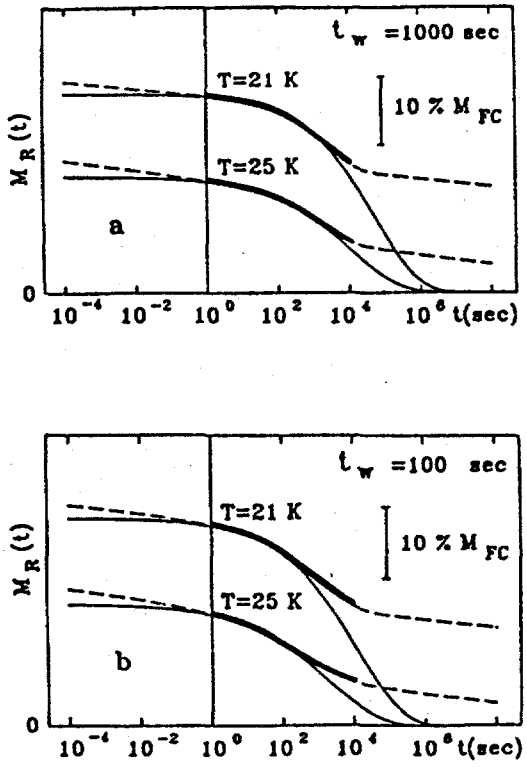

Figure 2.14. Relaxation of the TRM of *Cu*Mn 0.5 % in the time interval 10^{-4} to 10^{8} seconds. Thick full lines are the experimental data. Thin full lines represent fitting by stretched exponential alone and the dashed lines represent fitting by stretched exponential and a logarithmic term. (a) t_w = 1000 seconds and T = 21 K (top) and 25 K (bottom); and (b)) t_w = 100 seconds and T = 21 K (top) and 25 K (bottom) (after Mydosh, 1993).

fits reasonably well for times that are close to the wait time but the fit is progressively worse for much larger or smaller time scales. In order to get a better fit a second term is superimposed on the stretched exponential which is purely logarithmic of the form,

$$M'_R(t) = SH \ln t \qquad (2.30)$$

where S is the relaxation rate in dynamical equilibrium. By the addition of this second term the fitting greatly improves and this is seen by the dashed line in Figure 2.14. This shows that the relaxation process is logarithmic for $t<t_w$ and $t>t_w$ and the wait time superimposes a stretched exponential on the relaxation processes around $t=t_w$.

2.3.7. Specific Heat

In this section the features of spin glasses that are displayed in measurements of the specific heat will be explored. Figure 2.15 displays the magnetic contribution to the specific heat of CuMn (0.3 %) as a function of temperature and at several different applied fields (Mydosh,1993). For this compound the freezing temperature is T_f= 3.0 K. The features displayed here are quite generic and are common to most spin glasses. At temperatures above T_f it should be noticed that there is a broad maximum above T_f and then a long tail. In metallic spin glasses, this tail follows an approximate 1/T dependence. Instead of a sharp feature which is typical of conventional phase transitions, the broad and smeared out nature of these features are indicative of the short range correlation and clustering of spins that is slowly building up and removing entropy as the temperature is decreased. It is from these clusters that the spin glass state is eventually

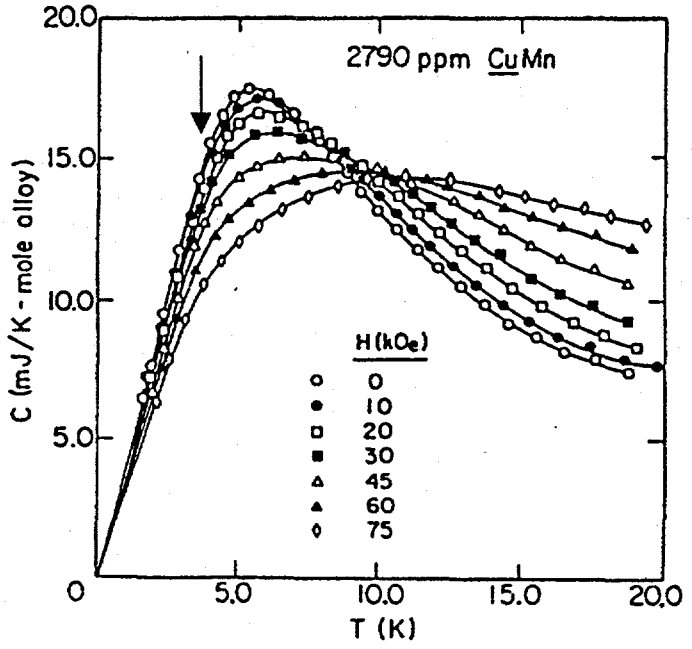

Figure 2.15. Magnetic contribution of the specific heat of *Cu*Mn (0.3 %) as a function of temperature at various fields. Note that T_f=3.0 K is indicated by the arrow. (after Mydosh, 1993).

constructed. Recall that the magnetic entropy, S_m, can be determined from the specific heat, $C_{p\text{-}mag}$,

$$S_m = \int_0^T \frac{C_{p-mag}}{T} \partial T = R \ln(2J+1), \qquad (2.31)$$

where the last term is the total degrees of freedom for a magnetic system. For spin glasses, a large proportion of this entropy is removed at temperatures above the freezing transition. This entropy is lost in the formation of the clusters.

At T_f there is very little to note, which in itself is noteworthy. There is no feature at freezing transition in contrast to the peaks and other features seen in the magnetic measurements. This is another indication that the transition is an unconventional one. Below T_f the specific heat has an approximately linear region. At the lowest

temperatures deviations to this linearity occur causing a positive upturn to force the specific heat to zero in accordance with the third law of thermodynamics. This low temperature upturn generally follows a $T^{3/2}$ behavior (Thomson, 1981). There are then a few primary features that are held in common between spin glasses in specific heat measurements. A broad peak and tail with a 1/T dependence for metallic systems indicative of the clustering occurring among the spins as the temperature drops. A large portion of the magnetic entropy is removed even before T_f is reached from above. No clear feature is seen at the transition in contrast to those seen in magnetization data. Below T_f there is an approximately linear region followed by a region with a $T^{3/2}$ dependence at the lowest temperatures.

3. CRYSTAL GROWTH

3.1. Advantages of Single Crystals

The first step in the study of crystalline materials is producing them. Quite often the initial crystals are in a polycrystalline form. This is frequently done by combining the pure elements using an arc-furnace with a water cooled copper hearth in an inert atmosphere, turning the samples several times between melts in order to insure homogeneity. Samples made in this way are called polycrystalline because they are composed of many microcrystals oriented randomly in space. Many new compounds are often discovered by this method, for example the rare earth nickel boro-carbides were first made in this way (Cava, 1994; Nagarajan, 1994). This method allows the study of the bulk and microscopic properties of the material, but since the microcrystals are randomly oriented, any information about anisotropic properties are averaged out. Single crystals are necessary for the study of the anisotropic properties of a material.

Another benefit of using single crystals is that their quality is generally superior to that of polycrystals. This is due primarily to impurities that are present at the grain boundaries of polycrystalline materials. These impurities are greatly reduced in single crystals due to their smaller surface area to volume ratio. Also for incongruent phases, the problem of having second phases present is large for arcmelted samples whereas second phases usually can be avoided and therefore are rarely present for flux grown samples. In addition, because of rapid cooling and crystallites growing against each

other, it is possible that a great amount of stress and strain may also be present in polycrystalline samples.

One method of crystal growth that works well is growth from a high temperature solution, also known as flux growth. This method provides an environment for the crystal to grow in that is free from many of the strains and temperature gradients that may be inherent to other methods. The crystals are grown from a liquid that is cooled over a long period of time so that the growth proceeds via a series of quasi-thermodynamically stable steps. This provides crystals that are relatively free from strain and displays their natural growth habits (Canfield, 1992). The next sections will more thoroughly discuss this technique as it is applied in the growth of certain binary and ternary compounds. The first section will discuss the growth of a binary compound and introduce binary phase diagrams. In the next section the growth of binary compounds from a third element will be discussed. The discussion will then move to the growth of ternary compounds, such as $TbNi_2Ge_2$, from a ternary melt and then to the growth of psuedoternary compounds. After this, specific techniques used in the growth of crystals from a high-temperature solution will be discussed.

3.2. Growth of Single Crystals from High Temperature Solutions

3.2.1. Binary Compounds

In order to grow binary compounds, it helps to become familiar with the associated binary phase diagram. These have been experimentally constructed for many elemental pairs and theoretically proposed for several others. An example of a phase

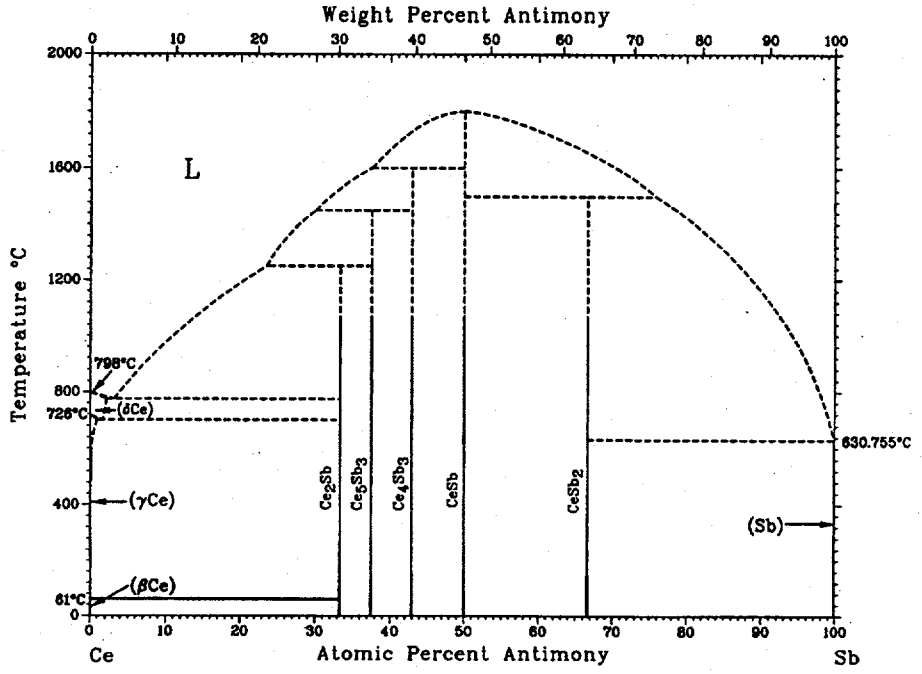

Figure 3.1 Phase diagram of Ce-Sb (after Massalski, 1992).

diagram is seen in Figure 3.1 for Ce and Sb. In the upper portion of the diagram is the region of homogeneous liquid (L). The lower portion contains solid compounds in equilibrium with the liquid and regions of all solid below the eutectic temperatures of approximately 760 °C and 630 °C. The curved line separating these two regions is the liquidus line. At low temperatures there are five compounds that are thermodynamically stable which are represented as vertical lines. These are Ce_2Sb, Ce_5Sb_3, Ce_4Sb_3, CeSb, and $CeSb_2$. Of these compounds, the only one that does not decompose before melting is CeSb, and is therefore a congruently melting compound. All the other compounds decompose into a liquid and a different solid before they reach the liquidus, and are called incongruently melting compounds. As an example, $CeSb_2$ is stable up to a

temperature of approximately 1500 °C, where it then decomposes into CeSb and liquid, which is represented by the horizontal peritectic line. This temperature is called the peritectic. If a composition of $Ce_{0.55}Sb_{0.45}$ is heated to above the liquidus then allowed to cool, several events will take place. First, as the melt cools below the liquidus, CeSb will be precipitated and the composition of the remaining liquid will move away from this compound, in this case to the left, following the curve of the liquidus. As the melt is further cooled past each successive peritectic, a different compound will be precipitated from the melt. At a composition of $Ce_{0.97}Sb_{0.03}$, the melt reaches a point where the liquidus reaches a minimum. This point is called the eutectic. A further decrease in temperature will result in the solidification of the remaining melt.

From the previous description, it is an easy step to grow single crystals from a high temperature solution, taking into account various limiting factors such as peritectic and eutectic temperatures. Limitations on temperature due to laboratory equipment must also be considered. The use of silicon carbide furnace elements and quartz to isolate the melt in an inert atmosphere, limits the upper temperature to 1500 °C and 1200 °C respectively. The case of $CeSb_2$ is illustrative of the procedure. From the phase diagram, it should be noted that $CeSb_2$ is in equilibrium with the melt up to 1500 °C, up to 10 atomic percent Ce can be dissolved in Sb at 1200 °C, and at 630 °C virtually all the Ce has been precipitated out in the form of $CeSb_2$ and the remaining melt is solidified as nearly pure Sb. Though 10 percent cerium can be accommodated, it is often advantageous to use a less concentrated solution. A solution whose composition is too close to that of the target crystal will often produce many small and intergrown crystals.

In order to better control the nucleation and allow space for the crystals to grow, less cerium is used, and in this case a concentration of $Ce_{0.05}Sb_{0.95}$ was found to produce well formed crystals. In order to avoid the solidification of the melt, the growth was ended at 675 °C, at which temperature the remaining liquid was decanted and large plate-like crystals of $CeSb_2$ were revealed (Figure 3.2a) (Canfield, 1992) (Bud'ko,1998).

The growth of crystals from an excess of one of the member elements is called a "self-flux" method, with the excess member acting as a flux to decrease the temperatures needed for growth. This method works well for many crystals, but not for all. As an example, consider CeSb. From the phase diagram it is seen that the lowest temperature at which CeSb exists in equilibrium with the melt with no other phases present is around 1500 °C. This is a rather high of a temperature for standard equipment and both cerium and antimony have large vapor pressures at this temperature. Single crystals of CeSb

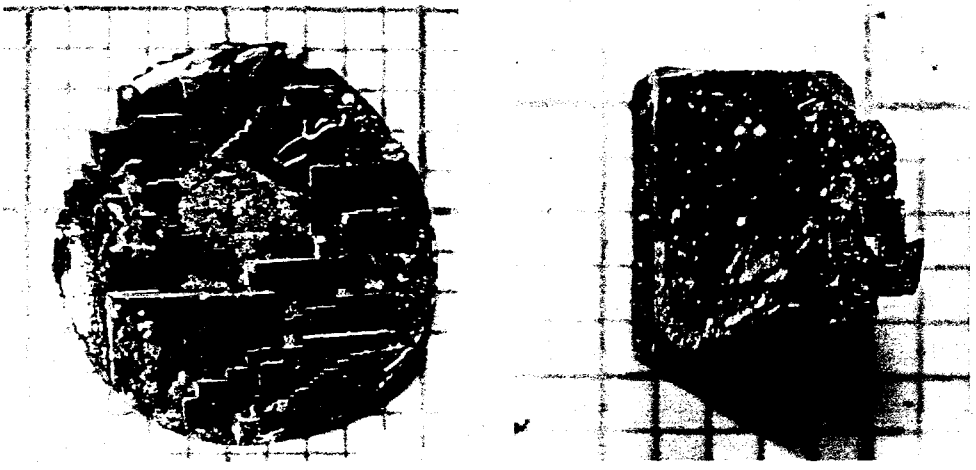

Figure 3.2 (a) Photograph of a single crystal of $CeSb_2$ grown from a self flux method. Notice the rectangular faceting on the face. The circular shape is caused by the crystal growing against the side of the crucible which has a circular cross-section (see section 3.2.4). (b) Photograph of a single crystal of CeSb grown from a third element flux. The crystal has a cubic growth habit which is consistent with the cubic crystal structure of CeSb. Both are on mm scales

have been grown from a mineralization technique, and many interesting phenomenon have been discovered but such crystals suffered from disorder and a lack of stoichiometry (Rossat-Mignod, 1977). In order to make flux growth feasible for this compound a method had to be found that lowered the growth temperature to accessible regions. This was done by the addition of a third element to the melt to act as a flux. This is much like using H_2O to grow crystals of NaCl well below its 800 °C melting point. Again, it was empirically determined that a concentration of $(CeSb)_{0.06}Sn_{0.94}$ heated to 1150 °C and cooled to 800 °C at which point the excess liquid was decanted revealed well formed cubic crystals (Figure 3.2.b) (Canfield, 1992). Measurements on these crystals have revealed that they are of a higher quality than those previously grown (Wiener, 2000a).

3.2.2. Ternary Compounds

Ternary compounds can be grown from high temperature solutions in a manner similar to that of binary compounds. The largest difference is the general absence of published ternary phase diagrams for many systems of interest. With 90 naturally occurring elements, there is a large number of possible binary combinations, and not all of them are published. There are 117,480 possible ternary combinations and only a relative few systems are well quantified. Because of this lack of knowledge about the liquidus surface and the corresponding peritectic eutectic temperatures, growth of ternary (and higher) compounds is an even more empirical process. Thus, initial attempts are based on studies of appropriate binary phase diagrams.

For the growth of $TbNi_2Ge_2$, these diagrams would be Tb-Ni, Tb-Ge, and Ni-Ge (Figure 3.3). It is unfortunate that the Tb-Ni diagram does not exist, but several binary

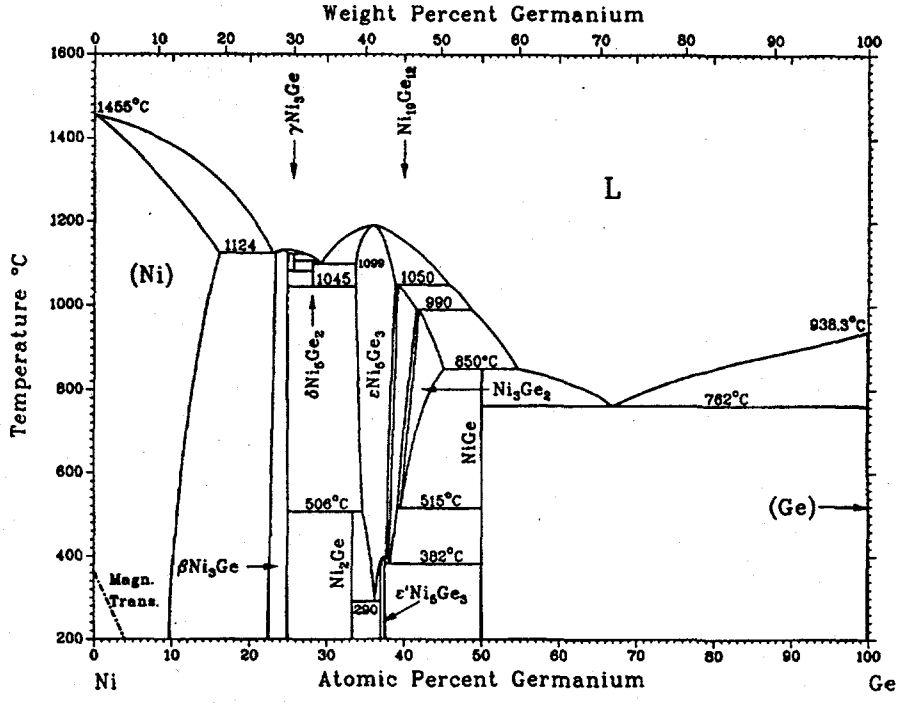

Figure 3.3 Phase Diagram for Ni-Ge (after Massalski,1992)

compounds of Tb-Ni are known to exist, as do several ternary compounds. There is a broad eutectic trough in the Ni-Ge diagram with the eutectic at a composition of $Ni_{0.33}Ge_{0.67}$, and initial attempts were performed with this concentration as a flux. From qualitative (crystal size, morphology, amount of flux on surface facets) and quantitative (resistivity, magnetization, powder x-ray diffraction) analysis of the resulting crystals, suitable initial concentrations and temperature profile were optimized. This led to the use of $Ni_{0.5}Ge_{0.5}$ as a flux rather than the eutectic composition. A summary of the binary and ternary phases are shown in a ternary phase diagram (Figure 3.4). Though there are many binary and ternary compounds in this system, it proved possible to grow large single

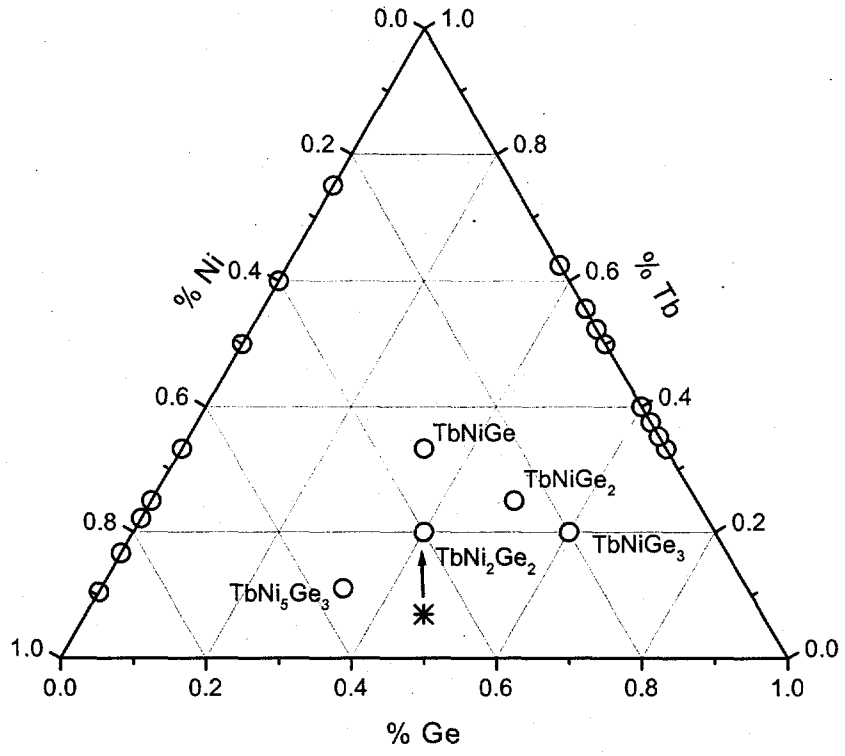

Figure 3.4 Tb-Ni-Ge ternary phase diagram. Circles represent known compounds and the * and arrow represents the starting melt composition for the growth of $TbNi_2Ge_2$.

crystals of $TbNi_2Ge_2$, with an initial composition of $Tb_{0.07}Ni_{0.465}Ge_{0.465}$. Details of the growth are described in section 3.2.4.

3.2.3. Psuedoternary Compounds

A psuedoternary compound is an alloy on one or more sites of a ternary compound, in contrast to a quaternary compound which has a distinctive crystallographic site(s) for each particular element. The underlying assumption behind this type of growth is that the physical and chemical processes controlling the precipitation of the crystal are unable to distinguish between chemically similar elements. $TbNi_2Ge_2$ is amenable to this procedure in a couple ways. It has been shown to be possible to substitute cobalt and

copper for nickel and thereby study the effects of band filing on the magnetic properties of the system (Wiener, 2000b). More importantly, it is often possible to substitute one rare earth element for another. This has led to many studies on the effects of deGennes scaling and the substitution of Heisenberg, Ising, and X-Y magnetic moments on the magnetic properties of many systems, such as RNi_2B_2C (Cho, 1996) and R-Mg-Zn quasicrystals (Fisher, 1999). As was mentioned in chapter 1, yttrium was chosen as the nonmagnetic as the counterpart to the terbium based on the observation that the lattice parameters of the two pure compounds, $TbNi_2Ge_2$ and YNi_2Ge_2, are very similar. In substitution series, there is a concern that the actual composition may be different from the nominal concentration of the starting melt. In this study, actual compositions were measured to be close to the nominal concentrations for all x (see Chapter 5).

3.2.4. Experimental Technique for Crystal Growth

The growth of $TbNi_2Ge_2$ and its derivatives takes place in a well controlled environment. Elemental starting materials with typical purities of 99.99 – 99.999 % are placed in a 2ml or 5ml alumina crucible, which is called the "growth crucible". A second crucible is filled two-thirds full with quartz wool and inverted on top of the growth crucible. The crucibles are then sealed in quartz tubing with a partial pressure of argon in order to prevent oxidation of the melt. The growth is then placed inside a box furnace and heated to 1190 °C. The sample is then cooled slowly over a period of approximately 100 hours to a temperature of 1000 °C. At this temperature the growth was stopped so as to avoid growing some of the possible phases present in the Ni-Ge phase diagram as impurities, and the crystals are separated from the remaining liquid. This is easily done

by removing the quartz ampoule from the furnace and quickly inverting it into a centrifuge and spinning it for a few seconds. During the spin, the quartz wool that was placed in the inverted crucible acts as a strainer, physically separating the crystals from the decanted flux. A diagram of the temperature profile for the growth is shown in Figure 3.5 (a). Figure 3.5.(b) contains a schematic of the ampoule in which the growth takes place, showing the placement of crucibles, quartz wool, and the pure elements as described above. Figure 3.6 shows an example of the crystals of $TbNi_2Ge_2$ grown in this manner. They are relatively large and well shaped, having a plate-like morphology with typical dimensions of 4 mm × 4 mm × 1 mm, with the c-axis perpendicular to the plane of the plate (Islam, 1998).

(a) (b)

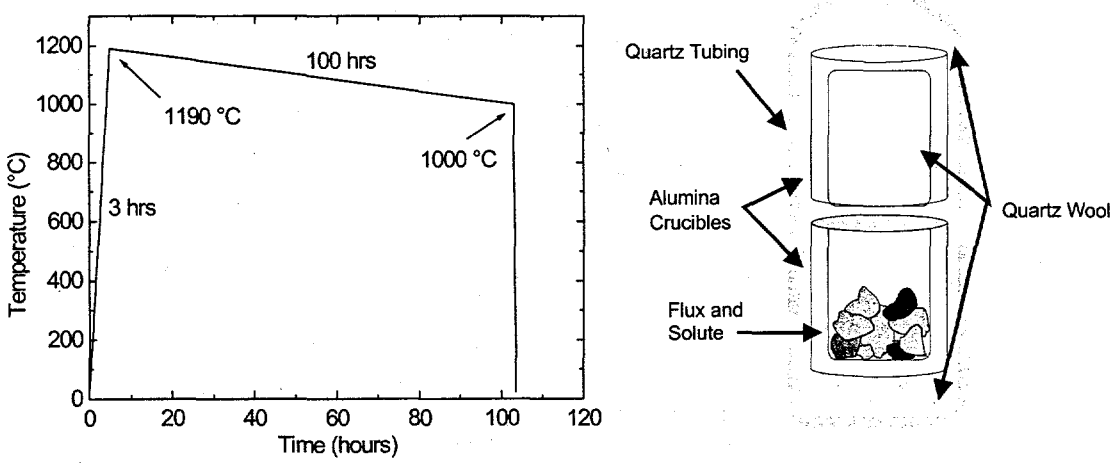

Figure 3.5 (a) Temperature profile for the growth of single crystals of $TbNi_2Ge_2$ from an NiGe-rich flux. At about 100 hours, the ampoule is removed from the furnace and the remaining flux is decanted from the desired crystals. (b) diagram of the ampoule used for crystal growth.

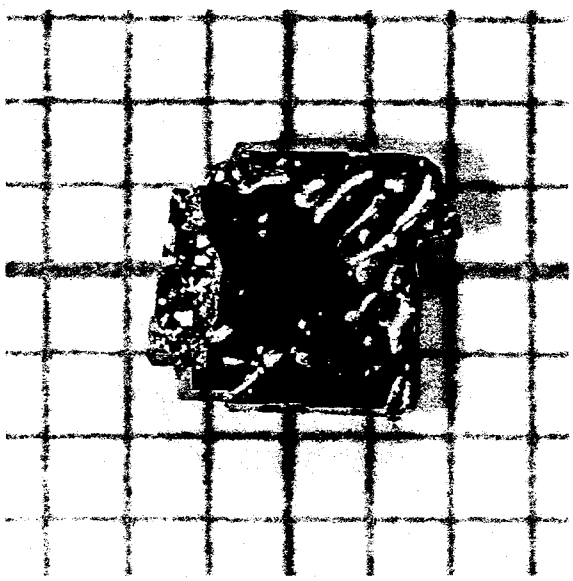

Figure 3.6 Photograph of a crystal of $TbNi_2Ge_2$ on a mm scale. The morphology is consistent with the tetragonal crystal symmetry. Also notice the small droplets of solidified residual flux on the surface, just right of center. Significantly larger crystals can be grown by this technique.

4. EXPERIMENTAL METHODS

4.1. Magnetization Measurements

4.1.1. DC Magnetization

DC magnetic measurements were performed in a Quantum Design Magnetic Property Measurement System (MPMS) Superconducting Quantum Interference Device (SQUID) magnetometer for temperatures between 1.8 and 350 K and fields up to 55 kOe. Samples were chosen for measurement based on size and lack of residual flux on the surface. Sample masses varied from approximately 15 mg for pure $TbNi_2Ge_2$ to 62 mg for $Tb_{.1}Y_{.9}Ni_2Ge_2$. These masses were chosen so as to provide a maximum magnetization of 1 emu at 55kOe, a value well below the 1.25 emu upper limit of the calibrated range of the system. Occasionally, residual flux would be mechanically removed, either by scraping with a scalpel or polishing with a Buehler Minimet polisher with a fine polishing pad and powdered alumina in water.

Samples were mounted inside two clear plastic drinking straws, the interior drinking straw having been fashioned in a manner useful for positioning the sample in a preferred orientation with respect to the applied magnetic field. In order to hold the plate-like samples with the axis normal to the surface of the plate (the c-axis) so that it is parallel to the field direction, the interior straw was folded along its length and then cut in half. The sample was then placed between the two halves, often sandwiched between two discs of weighing paper. For measurements with the c-axis perpendicular to the field direction, the interior straw was slit along its length and an X was cut half way along its

length, opposite to the slit, with the lower flap of the X pried back to provide a ledge for the sample to rest on. This method minimizes the background signal, although the contribution of the paper discs to the signal, although usually negligible, cannot be accurately subtracted.

Measurements were performed either with a zero-field cooled or field cooled history. In a zero-field cooled (zfc) measurement the sample is stabilized at a temperature well above any transition temperature in zero applied field. The sample is then cooled to a temperature below the transition, usually 1.8 K. At this temperature a field is applied and data is collected with increasing temperature. In a field cooled (fc) measurement the sample is stabilized at a temperature above the transition in zero applied field. A field is then applied and then the sample is cooled to its starting temperature, usually 1.8 K and data are taken with increasing temperature.

4.1.2. AC Magnetization

AC Magnetic measurements were performed in a Quantum Design MPMS SQUID magnetometer with an AC option. This allows experiments to be performed in oscillating fields with an amplitude between 0 to 4 Oe and with frequencies between 0.01 and 10000 Hz and an applied bias dc field up to 55 kOe. Samples were measured only with the applied field parallel to the c axis and mounted in the same manner as for DC magnetization with the same orientation.

4.1.3. Low Field Measurement Corrections

During this study, it was noticed that problems arose in data taken at low magnetic fields. In particular, measurements that were supposedly taken in the same low

field and in temperature ranges above any critical temperatures on the same sample, did not always coincide. This leads to an apparent offset between the affected data sets. This made analysis of the data extremely difficult, especially in the determination of the irreversibility temperature which was defined as the temperature at which the zero field cooled and field cooled data differed by 0.5 %. In Figure 4.1 the zfc and fc dc susceptibility data for $Tb_{0.60}Y_{0.40}Ni_2Ge_2$ is shown. These data were taken in a nominal field of 50 Oe. The offset between the two data sets is about 1.3 % at 15 K, which is well above the Néel temperature of 8.4 K for this dilution.

At this temperature both measurements should be identical. Closer examination revealed that the offset is approximately constant between 10 and 20 K. This indicated that the data could be made to coincide by an appropriate renormalization. In low applied

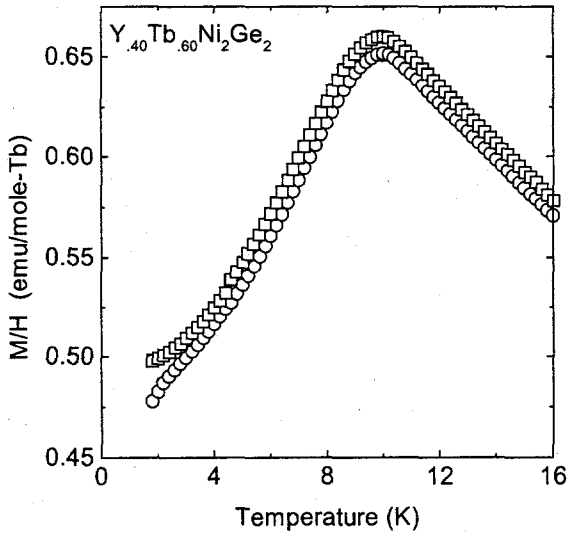

Figure 4.1 raw data for the low field dc susceptibility of $Y_{0.40}Tb_{0.60}Ni_2Ge_2$ at 50 Oe. Circles are zfc data and squares are fc data. Notice the large offset between the data at 15 K.

fields, the susceptibility can be approximated by χ = M/H rather than the theoretical definition of the susceptibility being the derivative of the magnetization with respect to the applied field, it appeared that an acceptable method would be to normalize the data to the theoretical definition at a particular temperature.

This was done by performing a measurement of the magnetization with respect to field at a temperature above the region of interest, in this case at 15 K. The result of this can be seen in Figure 4.2(a). At this temperature the magnetization is linear with respect to field and the slope is the susceptibility. The experimental zfc and fc data were normalized to this value by the application of a multiplicative constant. After normalization (Figure 4.2(b)) the offset has disappeared and the irreversibility temperature can be easily determined and is found to be about 7 K for this particular

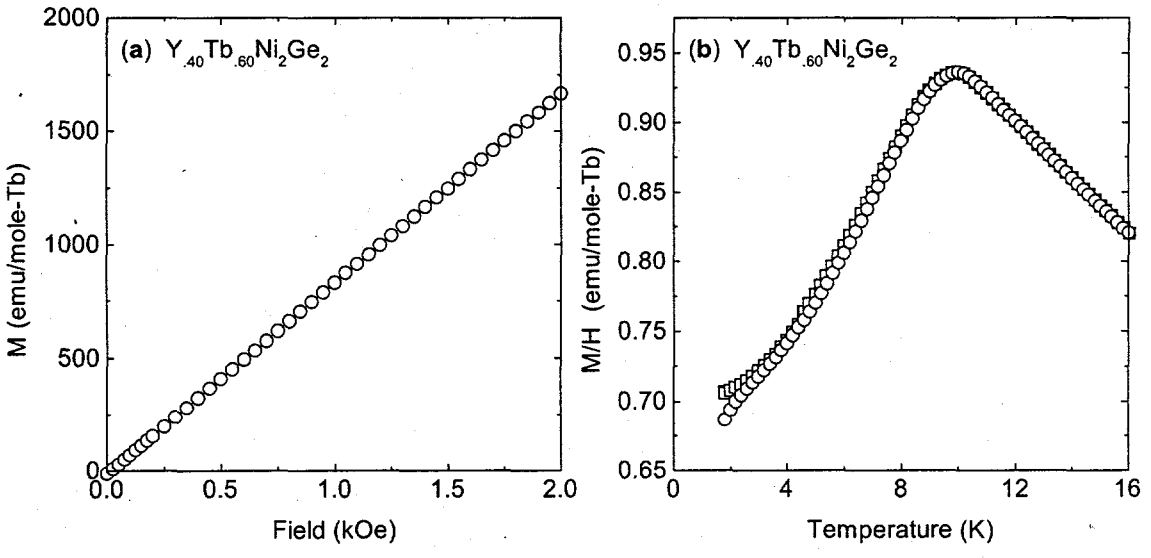

Figure 4.2 (a) magnetization as a function of applied field at 15 K for $Y_{0.40}Tb_{0.60}Ni_2Ge_2$. (b) Low field dc susceptibility of $Y_{0.40}Tb_{0.60}Ni_2Ge_2$ at 50 Oe after normalization (see text). Irreversibility between zfc (circles) and fc (squares) is more clearly seen than in Figure 4.1.

sample. This procedure was performed on data taken from all samples measured for purposes of consistency.

What is the origin of the above experimental problem? One clue is found if we look at the values of the susceptibilities before and after normalization. In the case of our example the values are approximately 40 % higher after normalizing. This indicates that the assumed field of 50 Oe in which the measurement was performed was higher than the actual applied field. In order for the experimental susceptibility, M/H, in Figure 4.1 to be equal to the susceptibility as determined from the slope of Figure 4.2(a), χ, the applied field can be determined from $H = \chi/M$. In this case the applied field is found to be about 34.8 Oe for the zfc data and 35.3 Oe for the fc data. Where does this 15 Oe difference come from? In an attempt to understand this, measurements of the magnetization as a function of applied field were performed in different temperatures (Figure 4.3(a)). This experiment was performed on $Tb_{0.45}Y_{0.55}Ni_2Ge_2$ after the SQUID had performed several other measurements with temperatures ranging from 1.8 to 350 K and fields from 0 to 55 kOe. As expected, the slopes of the various measurements decrease with increasing temperature, since the susceptibility is supposed to decrease with temperature. In a perfect world, the magnetization should be zero in a zero applied field so that all these lines should cross at the point H = 0 Oe, M = 0 emu/g. If they cross at a point H = 0 Oe, M 0 emu/g, this would indicate that there was a ferromagnetic component to the system, perhaps originating from some second phase impurities. If the lines cross at a point H 0 Oe, M = 0 emu/g, then there was a residual field present. As can be seen here, the lines cross at a point H = 15 Oe, M = 0 emu/g. Measurements were taken at higher

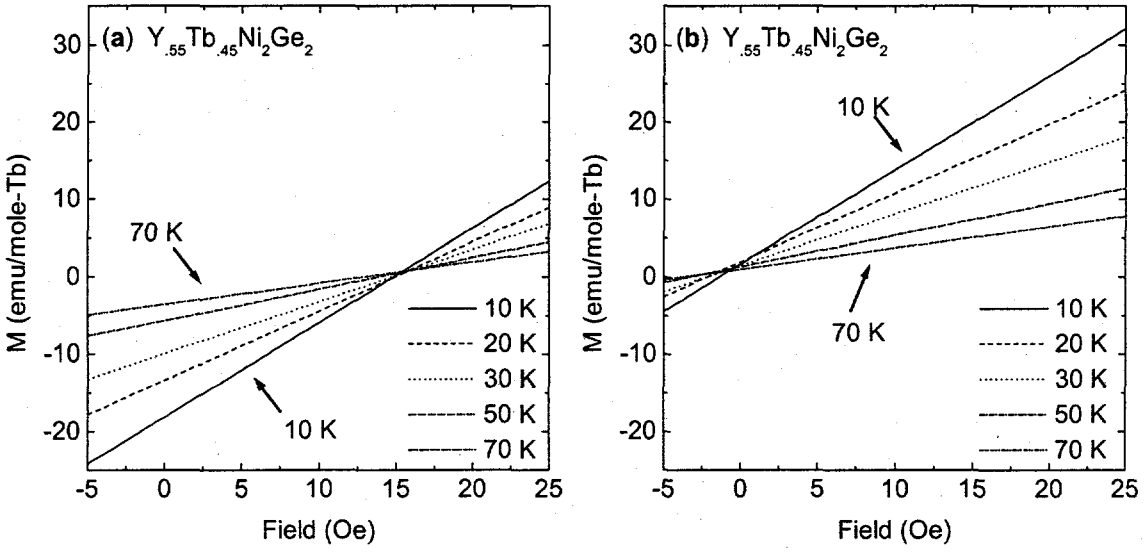

Figure 4.3 (a) Magnetization as a function of applied field of $Y_{0.55}Tb_{0.45}Ni_2Ge_2$ at different temperatures as listed in figure. Notice that all the lines cross at approximately H = 15 Oe and M = 0 emu/mole-Tb. (b) Magnetization as a function of applied field of $Y_{0.55}Tb_{0.45}Ni_2Ge_2$ at different temperatures as listed in figure with SQUID being demagnetized between runs. Notice that all the lines cross at approximately H = -1.5 Oe and M = 0 emu/mole-Tb

temperatures and they cross at the same point (not shown). This means that a field of 15 Oe had to be applied in order to achieve an effective field of 0 Oe, or there is a persistent field of 15 Oe which is opposed to the applied field. Therefore an applied field of 50 Oe would be effectively reduced to 35 Oe, which is comparable to the values obtained for the effective fields seen in the previous case.

In an attempt to reduce this residual field, the SQUID was run through a demagnetization sequence in order to reduce the trapped field in a superconducting magnet. M(H) runs were performed for the same temperatures and on the same sample as in Figure 4.3(a) with the exception that the SQUID was demagnetized before each run. Figure 4.3(b) shows the results of this experiment. From this it can be concluded that

even after being demagnetized, there is still a remnant field though it is reduced significantly to approximately 2 Oe and parallel to the direction of the applied field. Measurements at higher temperatures are similar (not shown). In both of these figures it is noticed that the lines tend to cross at a value of M that is slightly greater than 0 emu/g. This could indicate that there is a small amount of ferromagnetic impurities present. This would not be too surprising since both terbium and nickel are ferromagnetic at these temperatures and therefore the small amount of flux that adhered to the surface of the crystals or was trapped in small pockets inside the crystal could contribute a small ferromagnetic component.

Another measurement problem that occurs is the difficulty of performing measurements between 4.2 and 4.4 K in the SQUID magnetometer. This is associated with the boiling point of liquid helium at 4.2 K. The magnetometer has two modes of temperature control, one for temperatures above this point and another for below. Neither method works well at temperatures near this point and the magnetometer becomes unstable in temperature. Due to this problem, various features may be seen in both magnetization and resistivity data around 4.4 K. In many measurement there is a gap in the data for this region. In others, sharp features may be seen, but they are probably manifestations of this temperature instability and are therefore ignored.

4.2. Resistivity

Resistivity measurements were made with the standard four-probe technique within the temperature and magnetic field environment of the Quantum Design MPMS.

Samples used for measurement were shaped with a wire saw using a 0.005 inch diameter wire with 600 grit silicon carbide powder suspended in a water and glycerol solution. Sometimes in was also necessary to polish the samples using a Buehler Minimet polisher with a fine polishing pad and powdered alumina in water in order to remove residual flux and to remove steps from the surface. Platinum wires with a 0.025 mm diameter were attached to the samples using Epotek H20E silver epoxy and cured at 120 °C for 30 minutes. Typical contact resistances were between 1 and 2 Ω. A typical resistance bar is shown in Figure 4.4. Uncertainty in the measurement of the cross-sectional area and distance between voltage contacts are the major source of uncertainty in these measurements, limiting the precision of the resistivity to around 10%. The resistance of the samples was measured using a LR-400 AC bridge operating at a frequency of 15.9 Hz and an excitation current of 3 mA. The data acquisition was controlled and saved by

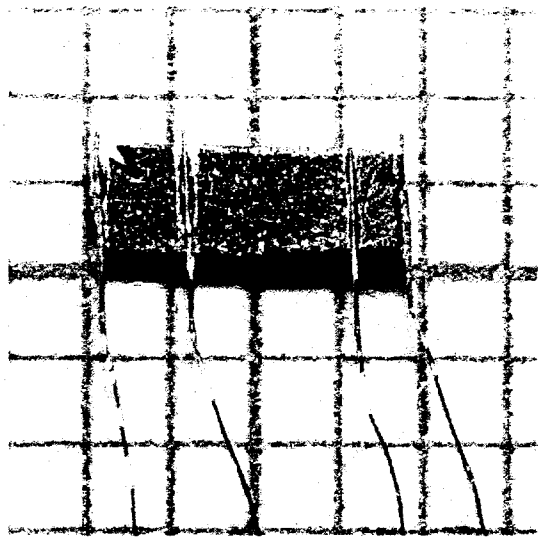

Figure 4.4 Photograph of a sample of $Y_{0.20}$ $Tb_{0.80}Ni_2Ge_2$ shaped into a resistivity bar with platinum wires attached with silver epoxy (see text), on a mm scale. The c-axis is out of the page.

External Device Control (EDC), an extension to the MPMS operating system.

4.3. Specific Heat

Specific heat measurements were performed using the heat capacity option of the Quantum Design Physical Property Measurement System (PPMS). This option uses a relaxation technique in which the sample is briefly heated and then allowed to cool. The system was typically allowed to cool over 1.5 to 2 time constants in order to achieve maximum accuracy within a reasonable amount of time. The response of the sample was then fit using a model that accounts for the thermal relaxation of both the sample and the sample platform with grease. Samples were affixed to the platform using Apiezon N grease. The thermal response of the platform and grease was measured first to allow for the subtraction of this contribution to the final measurement. The thermal contact of the sample to the environment was minimized by evacuating the sample chamber to approximately 0.01 mTorr. Samples for measurement were chosen on the basis of size, typically being about 3 mm by 3 mm, and the flatness of one face, which aids in the thermal contact of the sample to the sample platform.

In order to study the magnetic contribution to the specific heat that portion which is due to the electrons and lattice must be subtracted out. The simplest method is to have a suitable nonmagnetic material that is similar to the magnetic material being studied. A first choice would be YNi_2Ge_2. The yttrium compound was chosen for this dilution series because it is structurally similar to $TbNi_2Ge_2$, and therefore its specific heat should be a good approximation. There are two other possible choices as well. It has been shown

that the specific heat of $LaNi_2Ge_2$ and $LuNi_2Ge_2$ are nearly identical up to at least 50 K (Bud'ko, 1999). This shows that the slight differences in lattice parameters and masses between the lanthanum and lutetium compounds do not have a significant effect on the specific heat. This means that the nonmagnetic part of the specific heat of $TbNi_2Ge_2$ is best fit by either $LaNi_2Ge_2$ or $LuNi_2Ge_2$. Figure 4.5 shows a comparison of the specific heat of the lanthanum and yttrium compounds. Whereas lanthanum and lutetium compounds are identical, the yttrium compound has a very different temperature dependence. This difference may be due to the difference in masses between the two substances, and the Debye model suggests a simple scaling of the masses should make the specific heats the same (Chernikov, 2000). This is not the case and the specific heat of yttrium could not be simply scaled onto the lanthanum data.

Therefore it appears that the best choice to account for the nonmagnetic

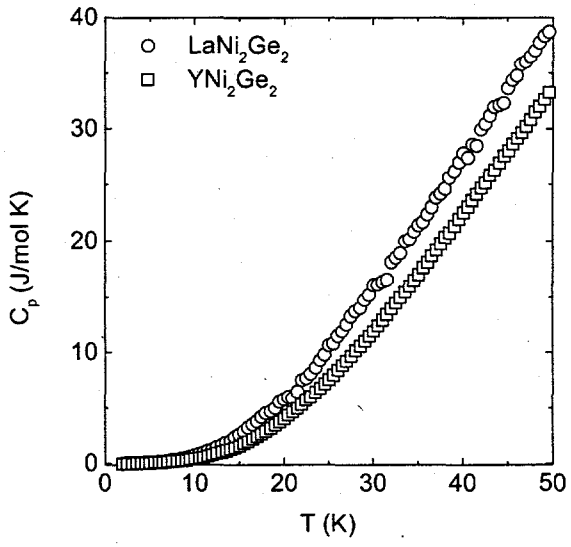

Figure 4.5. Temperature dependent specific heat, C_P, for (circles) $LaNi_2Ge_2$ and (squares) YNi_2Ge_2

component of the specific heat of the terbium compound is to use lanthanum. On the other hand, this can not be used for the entire dilution series since at low concentrations of terbium the specific heat will be due primarily to the yttrium in the compound. A plausible compromise is to subtract off that part of the nonmagnetic specific heat due to the yttrium using the yttrium data and to subtract off that part of the nonmagnetic specific heat due to the terbium using the lanthanum data. This leads to the formula

$$C_{p\text{-}mag}(Y_{1-x}Tb_xNi_2Ge_2) = C_p(Y_{1-x}Tb_xNi_2Ge_2) - (1-x)C_p(YNi_2Ge_2) - C_p(LaNi_2Ge_2)$$

which was used for all specific heat data presented in this study.

5. $Y_{1-x}Tb_xNi_2Ge_2$ (0<x<1)

5.1. Introduction

In this chapter some of the experimental results of this study are presented. In section 5.2 the experimental features of the end members of the series, pure $TbNi_2Ge_2$ and pure YNi_2Ge_2, are shown and discussed. In the section 5.3, the major features of the dilution series are presented and a temperature-composition phase diagram is introduced. This phase diagram is broken up into four regions. Sections 5.4 through 5.7 will look at representative compositions of several of these regions. The region of the dilution series that displays spin glass properties will be looked at in greater detail in chapter 6.

5.2. $TbNi_2Ge_2$ and YNi_2Ge_2

Recent studies have shown that the compound $TbNi_2Ge_2$ has many low temperature magnetically ordered states depending on temperature and applied field (Bud'ko, 1999; Islam, 1998). Figure 5.1(a) shows the DC susceptibility measured in 1 kOe from 2 K to 350 K with the field applied parallel ($\chi_{||}$) to and perpendicular ($\chi_{\perp}$) to the c-axis. It appears that the compound is Ising-like with the moments parallel to the c-axis. This has been confirmed by neutron diffraction studies (Islam, 1998). The feature seen in $\chi_{\perp}$ at ~ 45 K is due to thermal population of higher energy CEF levels. Figure 5.1(c) shows the low temperature portion of dc susceptibility, which clearly shows the two antiferromagnetic transitions in $\chi_{||}$. No transitions are seen in $\chi_{\perp}$. Figure 5.1(d) shows

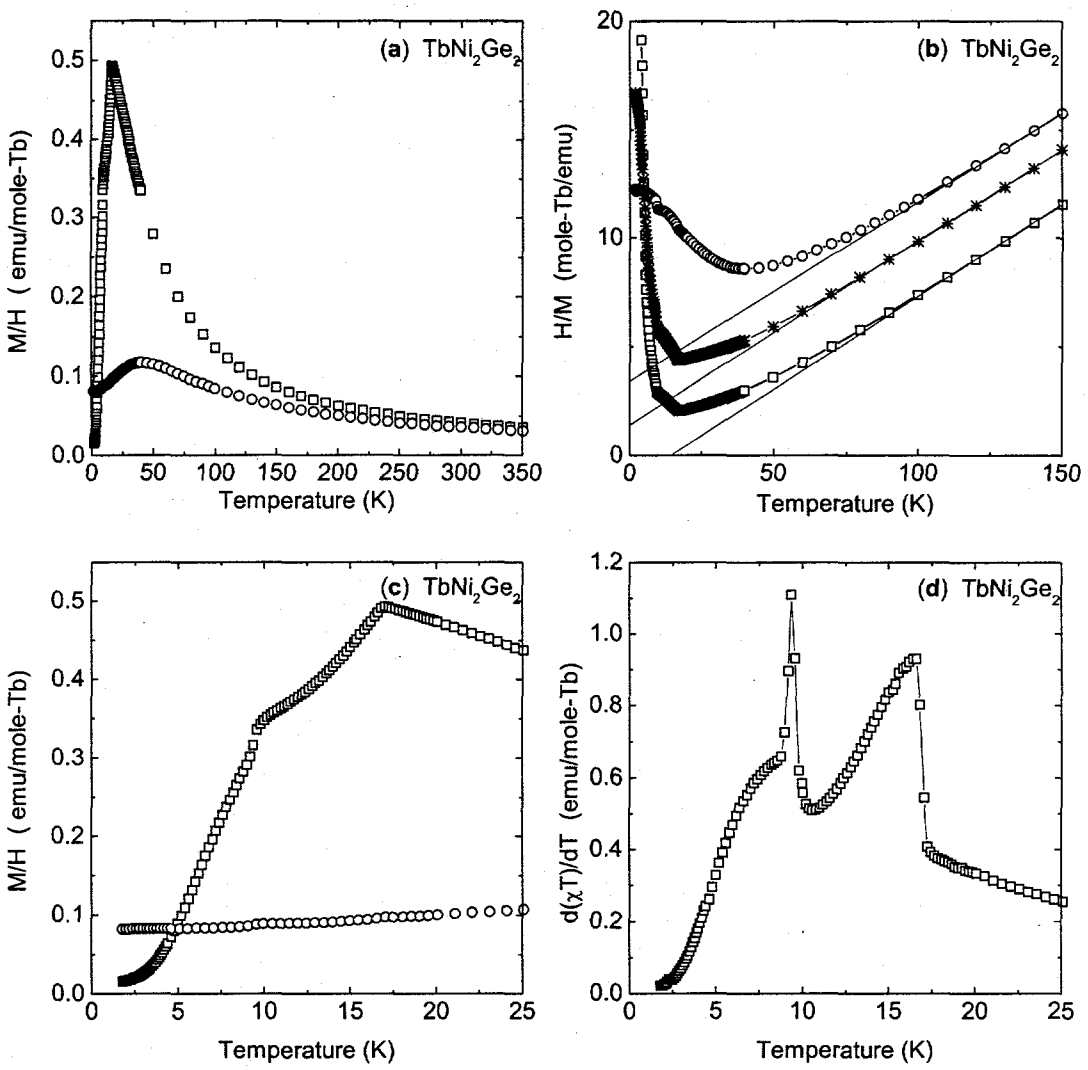

Figure 5.1. (a) Anisotropic temperature dependent dc susceptibility of $TbNi_2Ge_2$ at 1 kOe for field applied parallel to the c-axis (squares) and perpendicular to the c-axis (circles). (b) Inverse dc susceptibility for field parallel (squares) and perpendicular (circles) to the c-axis and for polycrystalline average (*). The solid lines are fits to the Curie-Weiss law at temperatures above 150 K extrapolated to low T. (c) Low temperature part of the susceptibility. (d) Plot of $d(\chi T)/dT$ as a function of temperature with a field of 1 kOe applied parallel to the c-axis.

$d(\chi T)/dT$ for H||c as a function of temperature. This is thought to be proportional to the magnetic specific heat near an antiferromagnetic transition (Fisher, 1962). For this reason transition temperatures will be determined from the peaks in this function. Both transitions are prominently displayed by lambda-like peaks, similar to what one might expect from the specific heat. The transition temperatures determined from these peaks are $T_N = 16.6 \pm 0.1$ K and $T_t = 9.4 \pm 0.1$ K, where the nomenclature for the transitions is following that of reference (Islam, 1998).

The high temperature DC susceptibility has been fit to a modified Curie-Weiss law,

$$\chi = \frac{C}{(T-\theta)} + \chi_0 \qquad (5.1)$$

where C is the Curie constant, θ is the Weiss temperature, and χ_0 is a temperature independent term. This last term reflects the temperature independent contributions to the total susceptibility, such as Pauli and Van Vleck paramagnetism, the diamagnetism of the ionic cores, and other effects that might arise from the experimental environment, such as the slight gap between the straws and the paper holding the samples. These contributions are negligible for pure $TbNi_2Ge_2$ as the paramagnetic contribution from the Tb^{3+} moments is much larger. This can be seen in Figure 5.1(b), which shows the inverse susceptibility as a function of temperature, where the solid lines are fits to Equation 5.1 at temperatures above 100 K. Below 100 K there are significant deviations from Curie-Weiss behavior. As the terbium is diluted with yttrium in the series, these secondary sources will become increasingly more significant.

Fits to this equation were made to the susceptibility with the applied field parallel and perpendicular to the magnetic easy axis (c-axis), as well as to the polycrystalline average. The polycrystalline average was determined by the following equation,

$$\chi_{poly} = \frac{(\chi_{\parallel} + 2\chi_{\perp})}{3}. \tag{5.2}$$

This is done so as to remove the effects of CEF splitting, at least to first order, from the determination of the effective moment and the Weiss temperature (Boutron,1973; Dunlap, 1983). This is also seen in Figure 5.1(b) where deviations from Curie-Weiss behavior begin at a lower temperature than for H⊥c and H||c. For $TbNi_2Ge_2$ $\theta_{\parallel}$ = 12.0 ± 2 K, $\theta_{\perp}$ = -50.7 ± 10 K, θ_{poly} = -14.6 ± 5 K, and the effective moment per terbium ion is 9.7 μ_B, which are also in agreement with previously published results (Bud'ko, 1999) and is comparable to the theoretical value of 9.72 μ_B for the Tb^{3+} ions.

Figure 5.2 shows the results of zero field resistivity measurements as a function of temperature. The resistivity is metallic with a residual resistance ratio defined as

$$RRR = \frac{\rho(300\ K)}{\rho(2\ K)}, \tag{5.4}$$

has a value of RRR = 4 for this compound ((a) inset). The low temperature resistivity (a) displays two kinks at the transition temperatures due to the loss of spin disorder scattering as the terbium moment become ordered. The derivative of the resistivity with respect to temperature (b), which is also considered to be proportional to the magnetic specific heat (Escorne, 1981), shows two sharp lambda-like peaks at T_N = 16.6 ± 0.1 K and T_t 9.3 ± 0.1 K which are similar in value to the peaks seen in $d(\chi T)/dT$.

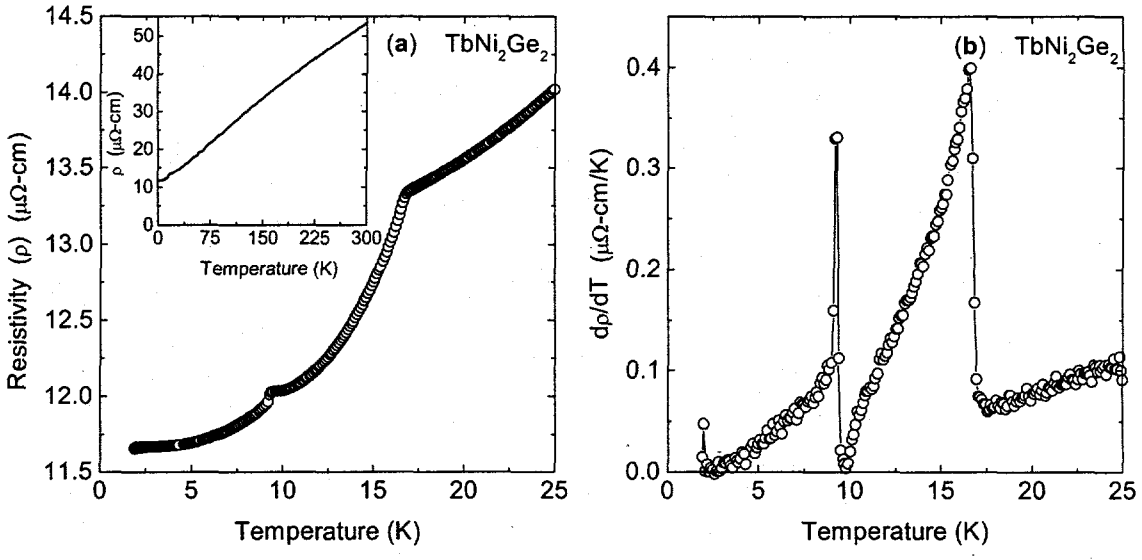

Figure 5.2. (a) Low temperature part of the zero-field temperature dependent resistivity of $TbNi_2Ge_2$. Inset show resistivity up to 300 K. (b) Low temperature part of $d\rho/dT$ as a function of temperature.

Figure 5.3(a) shows the magnetic specific heat, $C_{p\text{-}mag}$, with respect to temperature of the magnetic component of $TbNi_2Ge_2$. This was accomplished by subtracting the specific heat of $LaNi_2Ge_2$, which being nonmagnetic only consists of electronic and lattice contributions, from the specific heat of $TbNi_2Ge_2$ to isolate the magnetic contribution. Again, the two transition are clearly seen by lambda-like peaks and occur at $T_N = 16.55 \pm 0.05$ K and $T_t = 9.65 \pm 0.05$ K. Comparing the specific heat with $d(\chi T)/dT$ and $d\rho/dT$, it can be seen that these later functions do have similarities to the specific heat, though are not perfect imitations of it. With this said, all transition temperatures stated in this paper will be determined from the peaks in $d(\chi T)/dT$, unless otherwise noted. From these three measurements, specific heat, resistivity, and susceptibility, The

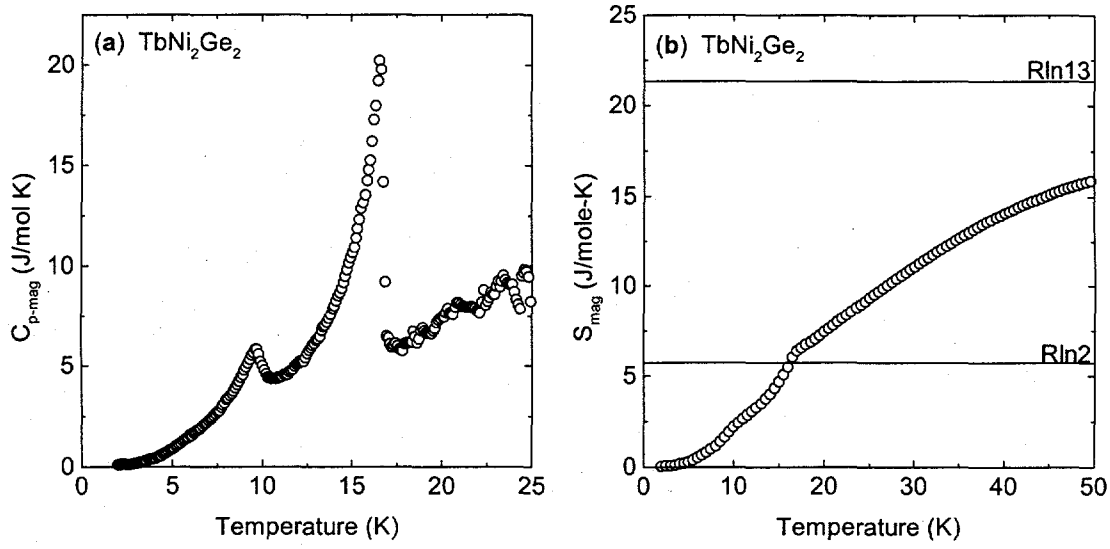

Figure 5.3. (a) Low temperature part of the zero-field magnetic specific heat as a function of temperature of $TbNi_2Ge_2$. (b) Magnetic entropy as a function of temperature. The solid lines show total theoretical magnetic entropy Rln13 and magnetic entropy of a doublet ground state, Rln2.

transition temperatures are determined to be $T_N = 16.6 \pm 0.1$ K and $T_t = 9.45 \pm 0.2$ K where the uncertainties reflect the differences in values from all three methods.

Figure 5.3(b) shows the magnetic entropy as a function of temperature where the solid lines show the entropy of psuedodoublet ground state, Rln2, and the total expected entropy of Rln13. The low temperature specific heat follows a T^3, which is typical of antiferromagnetic systems and is due to magnons and this same dependence was extrapolated down to 0 K to determine the entropy. As can be seen, the transitions at 9.65 K and 16.55 K removes only a little more entropy than that of Rln2. Another large portion of the entropy is removed by 50 K through the population of another set of CEF levels around 45 K (Islam, 2000). Since the entropy has not reached its maximum value

of Rln13 by 50 K, it is likely that other Schottky-like anomalies exist at higher temperatures. This behavior is consistent with the ordering of the CEF split ground states for $T < T_N$. In comparison the unsplit $GdNi_2Ge_2$ shows almost full removal of Rln8 at T_N (Bud'ko, 1999).

Figure 5.4 shows low temperature, field stabilized, metamagnetic states in both (a) magnetization and (b) resistance measurements with the field applied parallel to and perpendicular to the c-axis. These measurements were performed with increasing field to avoid the complications of hysterisis effects (Bud'ko, 1999). Six metastable states can be discerned (with the application of a slightly higher field one more transition occurs into the saturated moment state). It is clearly seen form these measurements, as well as from

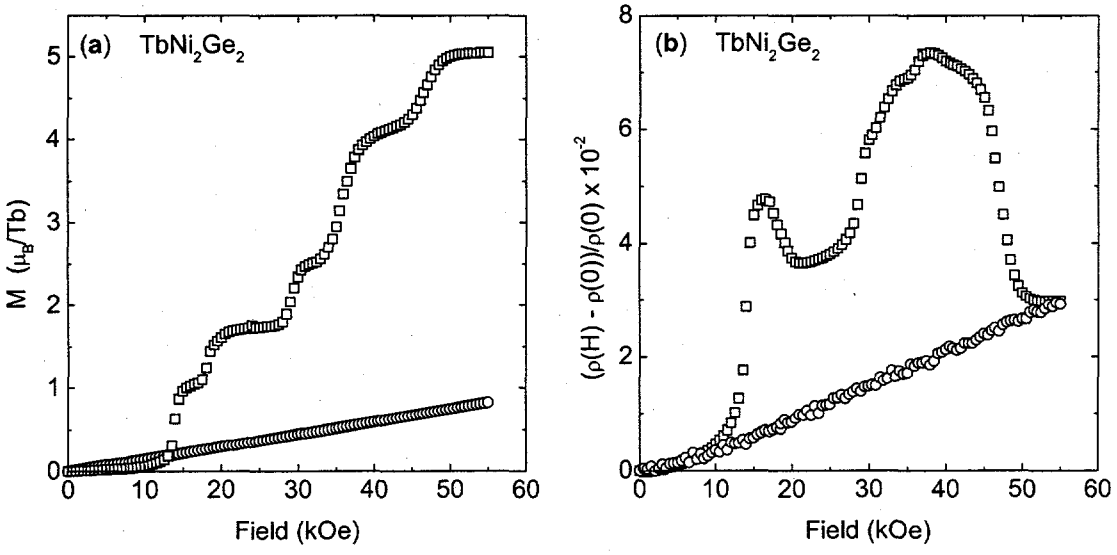

Figure 5.4. (a) Field dependent magnetization at 2 K for $TbNi_2Ge_2$ with the field applied parallel (squares) and perpendicular (circles) to the c-axis. (b) Magnetoresistance at 2 K for fields applied parallel (squares) and perpendicular (circles) to the c-axis.

the temperature dependent susceptibility measurements, that this compound is anisotropic with an easy axis along the c-axic (normal to the surface of the crystal) with little coupling between the applied field and the local moment sublattice when the field is applied perpendicular to the c-axis

Another way to measure this anisotropy is shown in Figure 5.5(a). Here the results of rotating a sample of $Y_{0.99}Tb_{.01}Ni_2Ge_2$ around an axis that runs through the plane of the sample and perpendicular to the applied field of 55 kOe and at 2 K. In this way the plane of the sample sweeps through an angle (θ) with respect to the applied field. Since the magnetometer measures the projection of the magnetic moment along the field direction, the magnetization as a function of angle should follow a $M|\sin\theta|$ dependence,

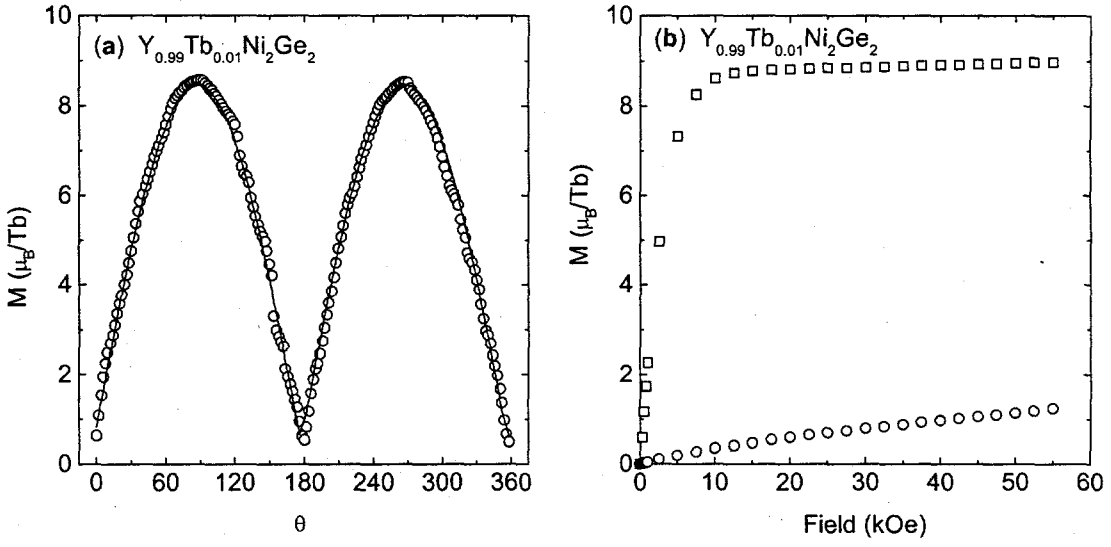

Figure 5.5. (a) Magnetization as a function of the angle (θ) between the applied field and the plane of the crystal for composition x = 0.01 at 55 kOe. The solid line shows fit of the projection of the magnetization as a function of angle, as described in the text. (b) Magnetization as a function of field applied parallel (squares) and perpendicular (circles) to the c-axis for x = 0.01.

which is verified by the solid line which is a fit to this function. This confirms that the magnetically easy axis lies along the c-axis. Figure 5.5(b) shows the magnetization as a function of field for the same sample with the field applied parallel and perpendicular to the c-axis for comparison. These measurements show that the anisotropy is purely a single ion effect associated with the CEF splitting.

Figure 5.6(a) shows the temperature dependent DC susceptibility at 1 kOe and the field dependent magnetization at 2 K of YNi_2Ge_2 for fields applied parallel and perpendicular to the c-axis. The susceptibility shows practically temperature independent Pauli-like paramagnetic behavior. At low temperature there is a slight upturn in M/H which may be associated with a small concentration of paramagnetic impurities. By fitting the upturn to Curie-Weiss law these impurities are estimated to be about 1 terbium

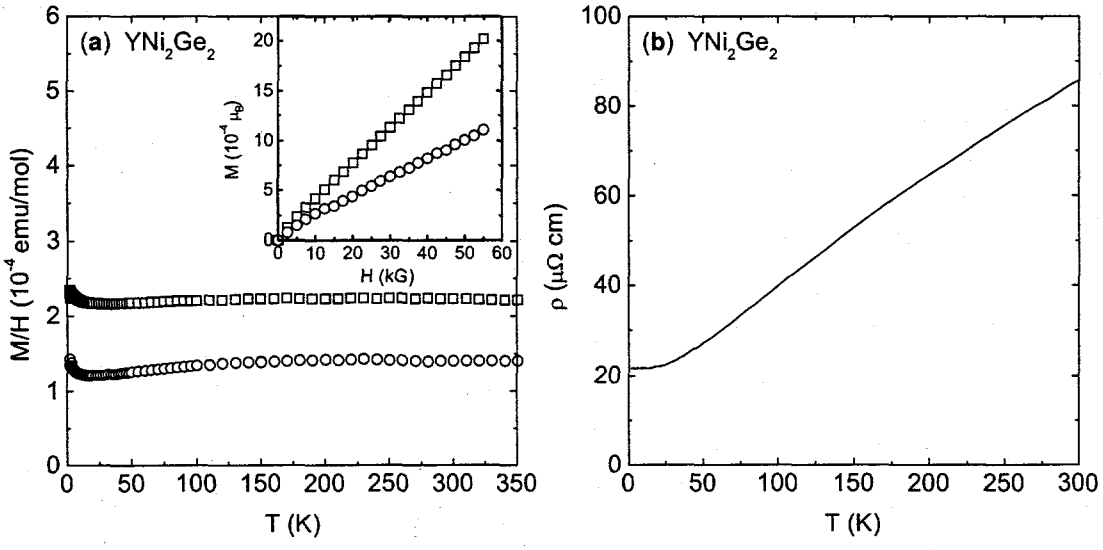

Figure 5.6. (a) Anisotropic temperature dependent dc susceptibility of YNi_2Ge_2 for a 10 kOe field applied parallel (squares) and perpendicular (circles) to the c-axis. Inset shows anisotropic field dependent magnetization at 2 K. (b) Zero-field resistivity as a function of temperature.

ion out of every 90,000 yttrium ions, which is close to the expected purity level of 0.9999. The susceptibility is weakly anisotropic with $\chi_{\|} > \chi_{\perp}$.Magnetization data at 2 K are nearly linear up to 55kOe (inset) The zero field temperature dependent resistivity is shown in Figure 5.6(b). The resistivity is metallic in character with a residual resistance ratio RRR of about 4 which is similar to that of $TbNi_2Ge_2$ (Bud'ko, 1999).

5.3. The $Y_{1-x}Tb_xNi_2Ge_2$ Series

As x is increased in the system $Tb_xY_{1-x}Ni_2Ge_2$, several interesting features appear. Perhaps the most important features can be addressed from a study of the changes in the characteristic temperatures as a function of composition (x). This is can be seen in Figure 5.7, where the two Neel temperatures (T_N, T_t), introduced in the previous section, and the irreversibility temperature (T_{ir}) are plotted. The irreversibility temperature is defined as the temperature at which the zero-field cooled (zfc) magnetization and the field-cooled (fc) magnetization differ by 0.5%. For a clear example of this see Figure 5.14(a). Based on these data we can divide the system into four main parts.

The first part is the region $0.75<x<1.0$. In this region both antiferromagnetic transitions exist, along with an irreversibility temperature. The second region has only the first transition and irreversibility temperatures and occurs when x is between 0.45 and 0.75. The third region is defined by $0.375<x<0.45$, where the antiferromagnetic transition and the irreversibility temperature coincide. The final region is defined by $x<0.375$. In this region there is no indication of antiferromagnetism and the irreversibility takes on many of the characteristics of a magnetic spin glass. The

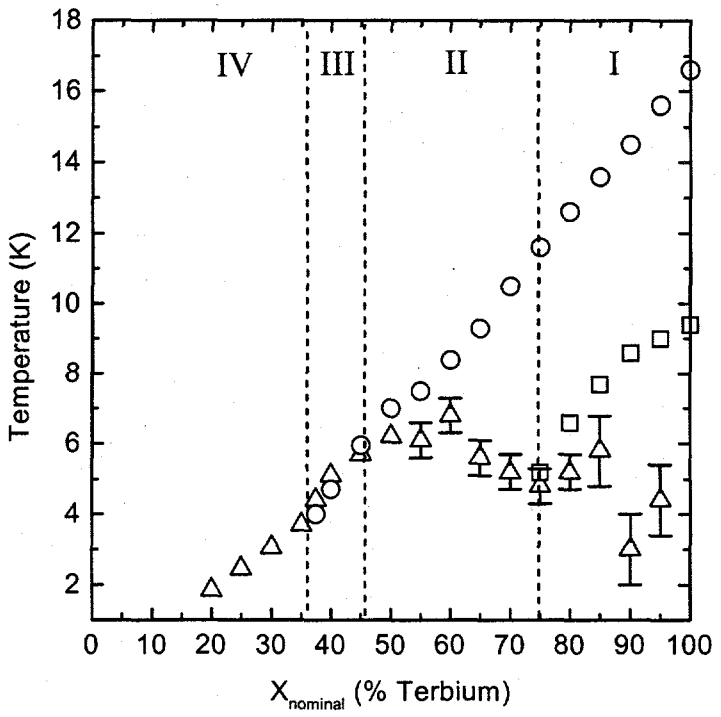

Figure 5.7. Temperature-composition phase diagram for $Y_xTb_{1-x}Ni_2Ge_2$. Temperatures plotted are the high temperature antiferromagnetic transition (T_N, circles), low temperature antiferromagnetic transition (T_t, squares), and irreversibility temperature (T_{ir}, triangles) as described in the text. The dashed vertical lines delineate the four regions of interest as mentioned in text.

concentrations below x = 0.20 may be considered that portion of the map similar to regions medieval cartographers labeled as "here there may be dragons". If there are features present at these concentrations, they take place at temperatures below 2 K, which are inaccessible to the techniques used in this study.

As can be seen in Figure 5.7, the high temperature antiferromagnetic transition (T_N), is approximately linear with respect to the concentration of terbium (x). Magnetic

transitions are expected to scale with respect to the deGennes factor in rare earth intermetallic compounds, which in a dilution series scales with x.

Weiss temperatures (θ) were determined from the high temperature dc magnetization in the manner described in section 5.2. These are shown in Figure 5.8(a). $\theta_{\|}$ is positive for all values of x and decreases in a linear fashion with x. $\theta_{\perp}$ is negative for all values of x and tends to increase in magnitude with decreasing x. The scatter in values for $\theta_{\perp}$ most probably reflects slight deviations in the applied field from being perfectly perpendicular to the c-axis. Since $\chi_{\|} >> \chi_{\perp}$, a small contribution of $\chi_{\|}$ to $\chi_{\perp}$ will have a much stronger effect than a small contribution of $\chi_{\perp}$ will have on $\chi_{\|}$. Because of this, all that can really be said is that $\theta_{\perp}$ is strongly negative and compared to the positive

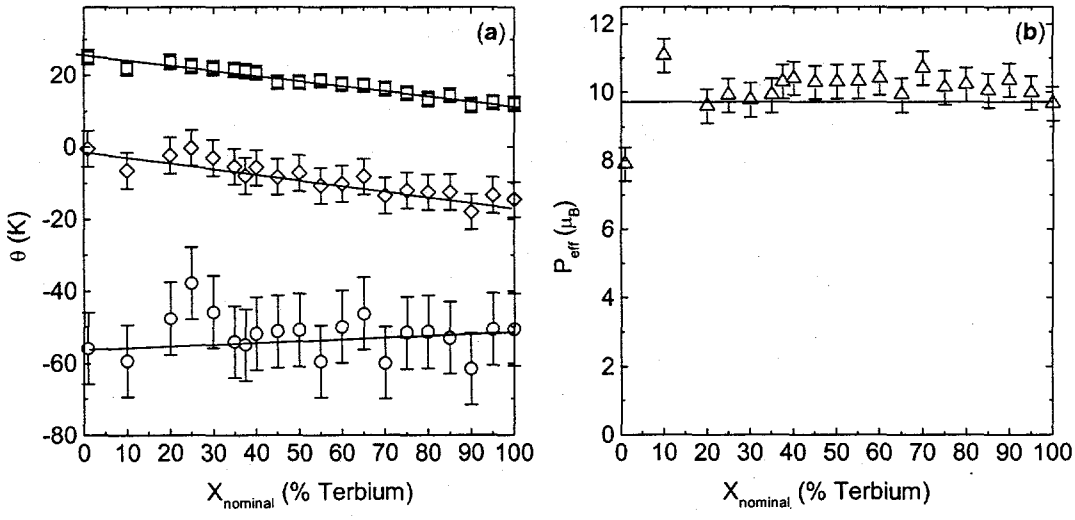

Figure 5.8. (a) Weiss temperatures (θ) as a function of composition (x) with field applied parallel (squares), perpendicular (circles) to the c-axis and polycrystalline average (diamonds). Lines are a guide to the eye. (b) Effective moment as determined from fits to Curie-Weiss law of polycrystalline average as a function of composition (x). Solid line shows calculated effective moment of 9.72 μ_B.

values of $\theta_{||}$ this compound is highly anisotropic for all values of x. θ_{poly} is also negative for all values of x and tends to decrease in magnitude with decreasing x. This is consistent with T_N decreasing in the same manner.

The effective moment per terbium ion, as determined from fitting χ_{poly} to the modified Curie-Weiss law as explained above, is close to the theoretical value of 9.72 μ_B for all values of x (Figure 5.8(b)). There seems to be a small systematic increase in the effective moment for values of x greater than 0.4. Between x = 0.2 and x = 0.35, the effective moment is very close to the theoretical value and this region corresponds to the region that displays spin glass behavior. The more erratic values for the p_{eff} for values of $x < 0.2$ may be explained by the actual dilution concentration not being the same as the nominal concentration and even one percent makes a large difference at small concentrations.

Conversely, in a similar manner, the concentration of terbium in the samples was also determined from the high temperature polycrystalline susceptibility. This was done by fixing the effective moment at 9.72 μ_B and calculating how much terbium would be needed to achieve that value. The concentration was also measured directly by electron microprobe analysis (EMPA) for nominal concentrations of x = 0.0, 0.20, 0.40, 0.60, 0.80, and 1.0. The results are seen in Figure 5.9. The solid line is the nominal concentration. The EMPA data lies close to the nominal values, with only a very slight positive deviation of about 2 % at x = 0.60. For concentrations between $0.20<x<0.40$, the concentrations derived from susceptibility measurements follow the nominal and EMPA values. Above x = 0.40 the susceptibility values vary greatly from the nominal values,

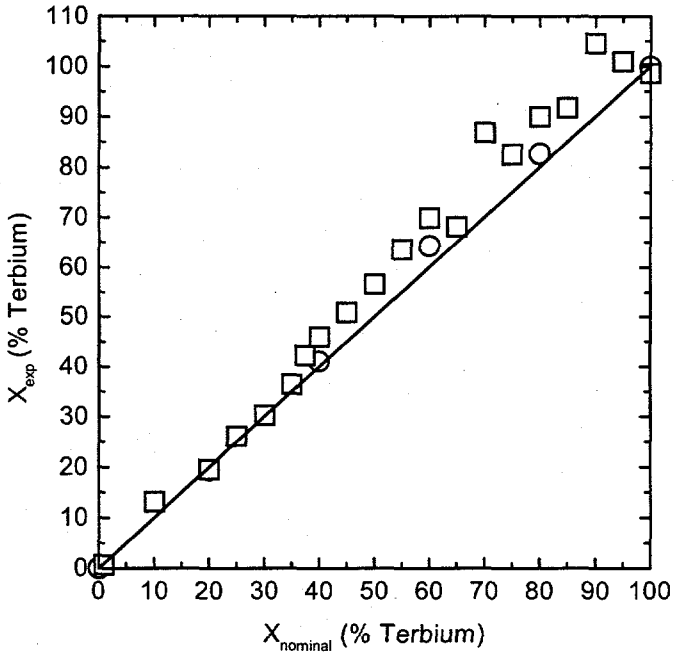

Figure 5.9. Plot of concentration determined experimentally versus nominal concentration. Solid line is nominal concentration, squares are the concentrations determined from high temperature Curie-Weiss fits. Circles are concentrations determined from EMPA. .

reaching the unlikely value of 105 % at x = 0.90. This large deviation reflects the elevated effective moments already seen for this region. Because the EMPA values compare well with the nominal values, the nominal values of x will be used throughout this work

To summarize the data derived from high temperature Curie-Weiss fits, the effective moment per terbium ion stays consistent with its theoretical value of 9.72 μ_B, the Weiss temperatures change systematically, and the system stays Ising-like throughout the dilution series (see Figure 5.5) This means that the changes in the transitions and in the low temperature ground state are due to dilution only. In the rest of this chapter, the

first three of these regions will be examined by looking at a representative composition from each. The fourth region, where spin glass like features emerge, will be more closely examined in chapter 6.

5.4. Region I: 0.75 < x < 1.00

$Y_{0.10}Tb_{0.90}Ni_2Ge_2$ is a representative of the compounds with the greatest terbium concentration (high x). Figure 5.10 shows the low temperature part of the dc susceptibility as a function of temperature for the field applied parallel to the c-axis for both zfc and fc histories. For the zfc data the sample was cooled in zero applied field to 2

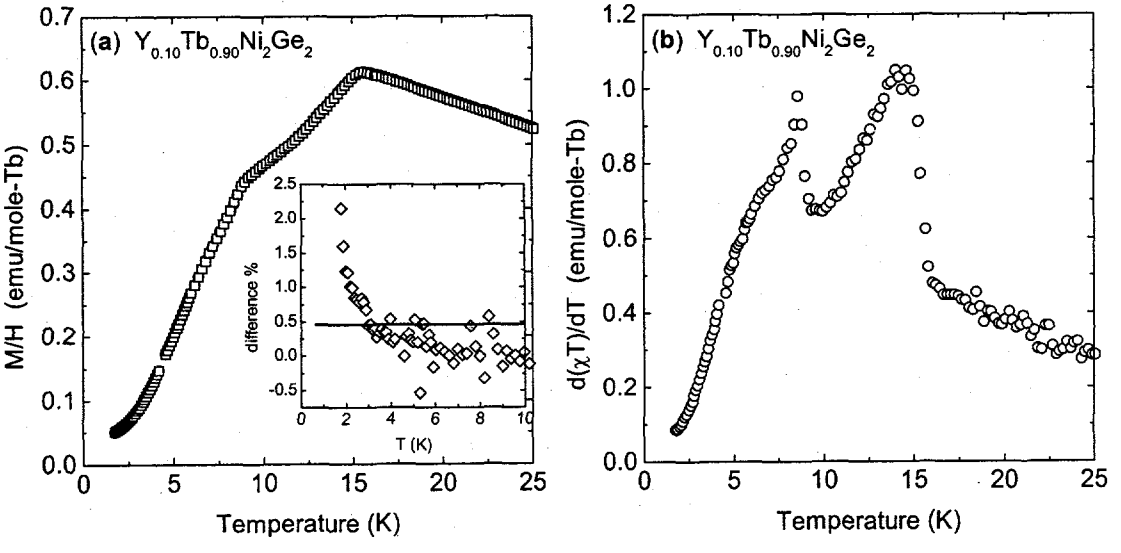

Figure 5.10. (a) Low temperature dc magnetization for zfc (circles) and fc (squares) histories with a field of 50 Oe applied parallel to the c-axis, for composition x = 0.90. Note that these data are almost indistinguishable on this scale Inset shows percent difference between zfc and fc magnetization as a function of temperature, with solid line showing 0.5 % criterion. (b) Plot of $d(\chi T)/dT$ as a function of temperature with field a field of 50 Oe applied parallel to the c-axis.

K and then a field of 50 Oe was applied. For the fc data, a field of 50 Oe was applied at 30 K, and then the sample was cooled to 2 K. The two antiferromagnetic transition temperatures, T_N and T_t, are still prominent. At low temperatures, no irreversibilities can be seen by eye, but if the two data sets are subtracted from each other, differences can be seen as shown in the inset to (a). The solid line shows the somewhat arbitrary 0.5% criterion used to determine the irreversibility temperature, T_{ir}. In this case $T_{ir} = 3.0 \pm 0.5$ K. The cause of this irreversibility is unknown. If another criterion had been chosen, then possibly this would not have been considered an irreversibility. The $d(\chi T)/dT$ is shown in (b). Here the transitions are again displayed by two lambda-like peaks, though not as sharp as those seen in $TbNi_2Ge_2$ (Figure 5.1(d)). The temperature of the transitions as determined from these peaks are 14.5±0.2 K and 8.6+0.1 K.

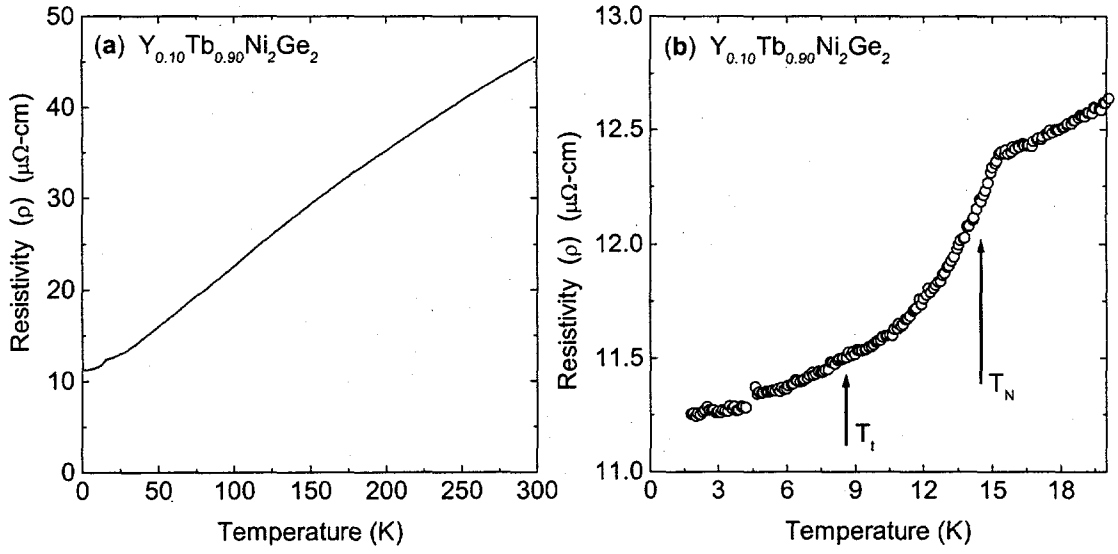

Figure 5.11. (a) Low temperature zero-field resistivity as a function of temperature for composition x = 0.90. Inset shows the resistivity up to 300 K. (b) Plot of low temperature part of dρ/dT as a function of temperature.

Figure 5.11 shows the zero-field temperature dependent resistivity for this concentration. The RRR is again around 4, as is seen in (a) which shows the resistivity up to 300 K. The low temperature part of the resistivity is seen in (b). The upper transition, associated with T_N, is seen as a large decrease in the resistivity due to the loss of spin disorder scattering, as was seen in $TbNi_2Ge_2$. The transition associated with T_t is not clearly seen, though there is a slight feature seen at roughly 8.5 K, close to the value determined from $d(\chi T)/dT$. The transitions in this measurement for this compound are not as clearly defined as they were for the parent compound which is consistent with the results of the dc susceptibility measurements. The gap seen at ~4.4 K is due to measurement difficulties associated with the boiling point of helium.

Measurements of the specific heat were performed and the magnetic contribution

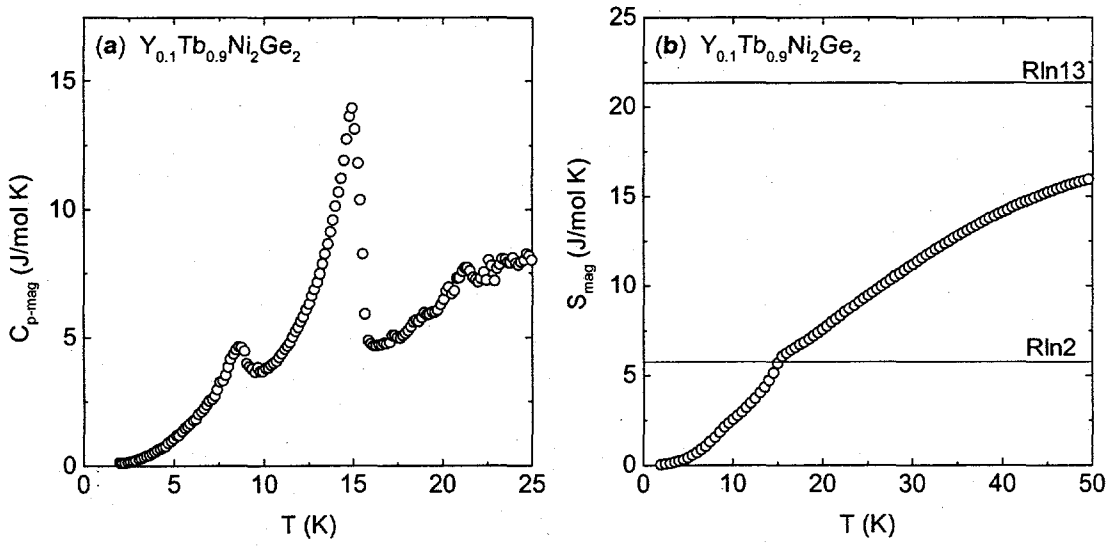

Figure 5.12. (a) Magnetic contribution to the specific heat as a function of temperature for composition x = 0.90. (b) magnetic entropy as a function of temperature. Solid line marks Rln13.

is shown in Figure 5.12(a). The magnetic specific heat was determined by subtracting a linear combination of the specific heat of yttrium and the specific heat of lanthanum, as was described in chapter 4. Similar to the pure terbium compound, at low temperatures there is a T^3 dependence, due to antiferromagnetic magnons, which was likewise extrapolated to 0 K to determine the entropy. Both transitions are clearly seen at the temperatures determined from $d(\chi T)/dT$. The entropy (b) is very similar to that of the pure compound.

Another example from this region is that of the composition with x = 0.80. Figure 5.13(a) shows the low temperature zfc and fc dc susceptibility, performed in the same way as before. Here the irreversibilities are more prominent. (b) shows $d(\chi T)/dT$ of the

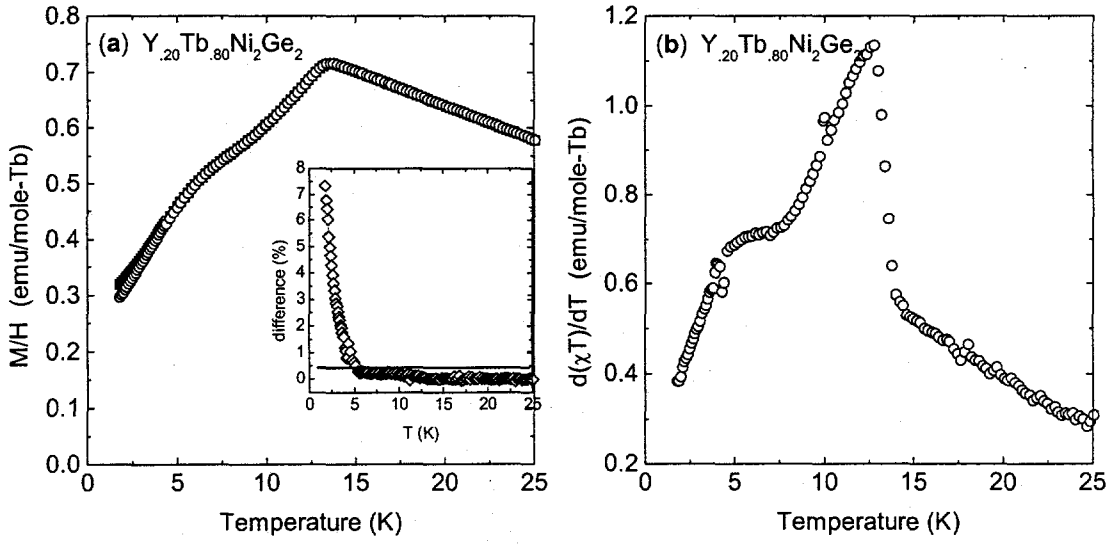

Figure 5.13. (a) Low temperature dc magnetization for zfc (circles) and fc (squares) histories with a field of 50 Oe applied parallel to the c-axis, for composition x = 0.80. Inset shows percent difference between zfc and fc magnetization as a function of temperature, with solid line showing 0.5 % criterion. (b) Plot of $d(\chi T)/dT$ as a function of temperature with field a field of 50 Oe applied parallel to the c-axis.

same sample. Here the transition to the lower ordered state, T_t, is a broad shoulder rather than a peak. The temperature for this transition is approximately 5.2 K ±0.5 K. Below this concentration, it becomes impossible to define a transition temperature for this magnetic state by magnetization measurements.

5.5. Region II: 0.45 < x < 0.75

In this region of the temperature-concentration phase diagram, the features associated with the lower antiferromagnetic transition are no longer present in susceptibility, resistivity, or specific heat measurements. This is illustrated by the magnetic behavior of the compound $Y_{0.40}Tb_{0.60}Ni_2Ge_2$. The low temperature dc

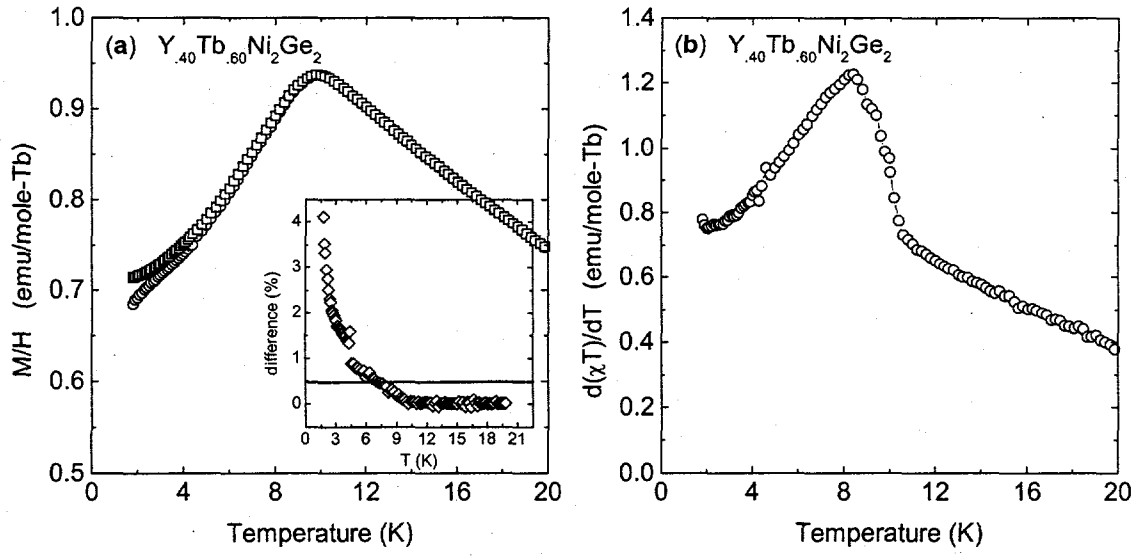

Figure 5.14. (a) Low temperature dc magnetization for zfc (circles) and fc (squares) histories with a field of 50 Oe applied parallel to the c-axis, for composition x = 0.60. Inset shows percent difference between zfc and fc magnetization as a function of temperature, with solid line showing 0.5 % criterion. (b) Plot of $d(\chi T)/dT$ as a function of temperature with a field of 50 Oe applied parallel to the c-axis.

susceptibility for zfc and fc histories is shown in Figure 5.14(a). There is a broad peak at about 10 K and the low temperature irreversibilities can be discerned quite easily, with a T_{ir} = 6.8±0.3 K. The feature representing the lower transition, which changed from a sharp peak in the pure compound to a rounded shoulder as yttrium was alloyed onto the terbium sites as seen in the previous section, has completely disappeared in (b) $d(\chi T)/dT$, leaving only one peak which is located at 8.4±0.1 K which is associated with T_N.

The zero field temperature dependent resistivity at low temperature also displays only one feature due to loss of spin disorder scattering (Figure 5.15(b)) and is located at approximately 8.5 K. For now note that the resistivity just above the transition is nearly horizontal as compared to the previous samples.. The residual resistance ratio is again approximately 4, as can be seen in Figure 5.15(a). Recall that the RRR's for both $TbNi_2Ge_2$ and YNi_2Ge_2 are also close to a value of 4, indicating that impurity scattering

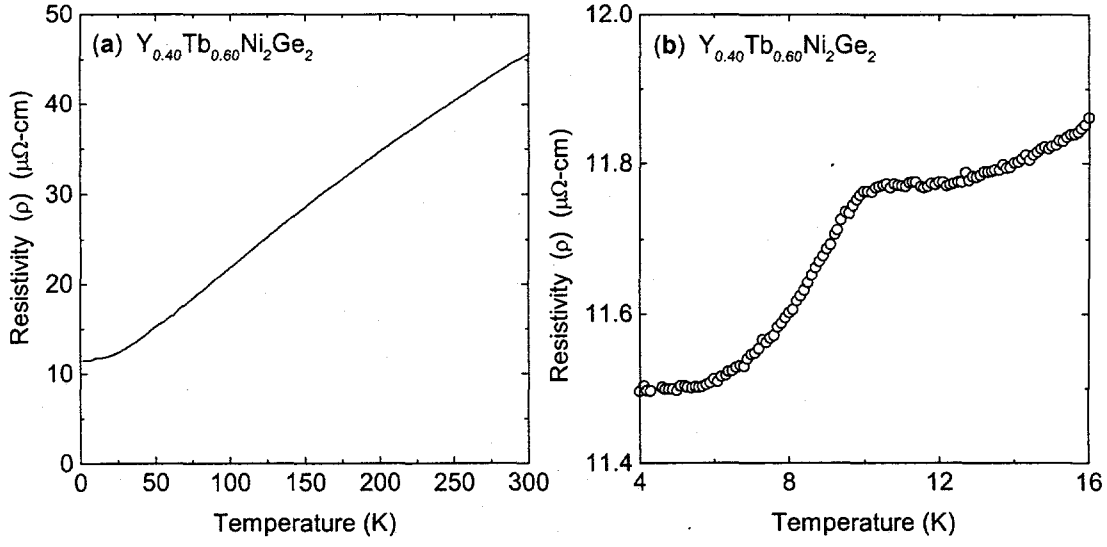

Figure 5.15. (a) Zero-field resistivity as a function of temperature for composition x = 0.60. (b) Low temperature part of the zero-field resistivity.

due to the substitution of yttrium on the terbium sites is insignificant in comparison to the impurity scattering that is already present in the crystals that have been grown.

Figure 5.16(a) shows the magnetic component of the specific heat, determined in the same manner as described above. The peak is located at 8.6 K, which is comparable to the values derived from $d(\chi T)/dT$. There is no evidence of a second transition at lower temperature. The temperature dependence at low temperature follows a $T^{3/2}$ dependence, which was extrapolated to 0 K for the determination of the entropy. This temperature dependence is consistent with either a spin glass state (Thomson, 1981) or ferro- or ferrimagnetic magnons. This change in power law also takes place as we change from a commensurate low temperature state to one of incommensurate order. This also has a large effect on the magnons. In any case, our subtraction is based more on empirical

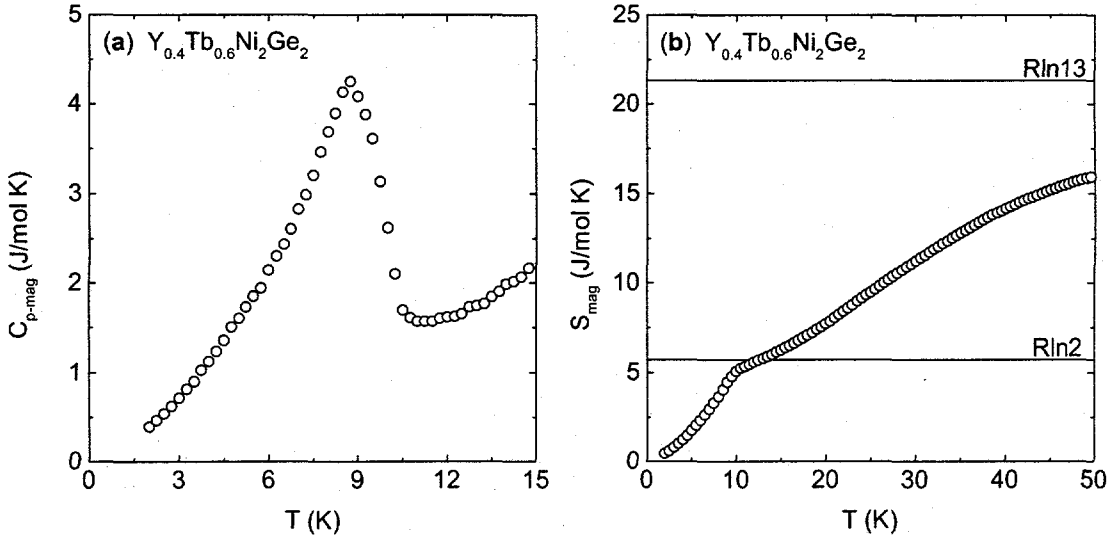

Figure 5.16. (a) Magnetic contribution to the specific heat as a function of temperature for composition x = 0.60. (b) Magnetic entropy as a function of temperature. Solid line shows position of the theoretical magnetic entropy for Tb^{3+} ion, Rln13, and the entropy of a degenerate two level ground state, Rln2.

observation than theoretical justification. Figure 5.16(b) shows the magnetic entropy. At the transition only Rln2 amount of the entropy is frozen out and then the entropy levels out before rising again in the same manner has as been seen for the other compounds. This value of the entropy (Rln2) is consistent with there being a doublet or psuedodoublet ground state in this compound, which is necessary for the existence of an Ising spin glass [Aeppli].

5.6. Region III: 0.375 < x < 0.45

In this concentration range there appears to be a crossover from predominantly antiferromagnetic order to a spin glass state at low temperatures. This can be seen in the

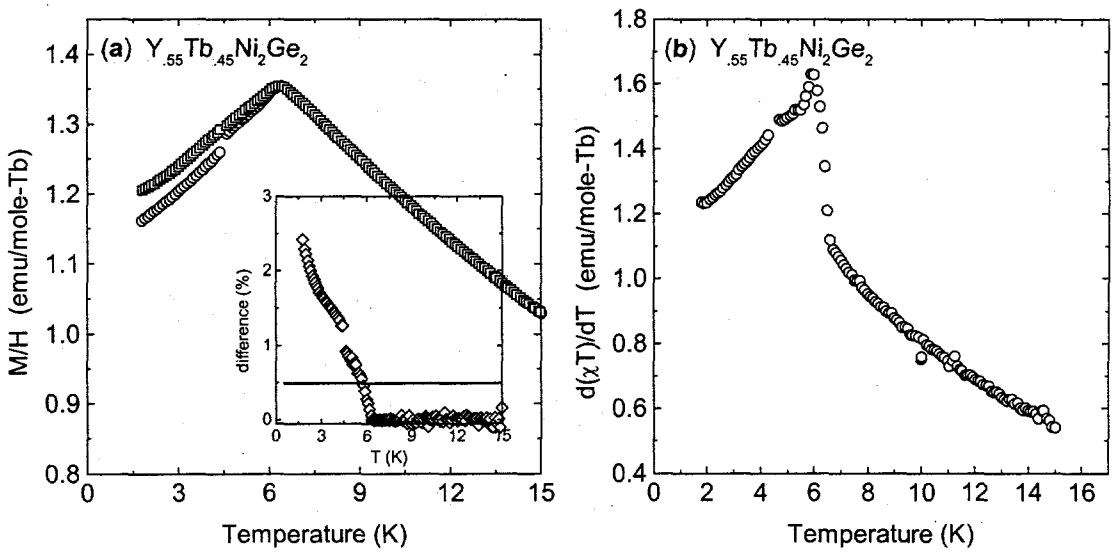

Figure 5.17. (a) Low temperature dc magnetization for zfc (circles) and fc (squares) histories with a field of 50 Oe applied parallel to the c-axis, for composition x = 0.45. Inset shows percent difference between zfc and fc magnetization as a function of temperature, with solid line showing 0.5 % criterion. (b) Plot of d(χT)/dT with as a function of temperature with field a field of 50 Oe applied parallel to the c-axis.

low temperature zfc and fc magnetization with a field of 50 Oe applied parallel to the c-axis (Figure 5.17(a)). The irreversibility is now prominent at all temperatures below the transition temperature, which in this case is $T_N = 5.95 \pm 0.1$ K. Using the 0.5 % criterion, the irreversibility temperature is determined to be 5.7 ±0.1 K as seen in the inset to (a). The $d(\chi T)/dT$ is shown in (b). The shape is becoming distorted from what has been seen before.

The resistivity is shown in Figure 5.18, with the full temperature resistivity shown in (a). This shows that the RRR ~ 3.6 which is consist with the previous the RRR's of the previously seen dilutions. The low temperature resistivity (b) shows a curious upturn in the resistivity below about 11 K. This upturn in resistivity is similar to what is seen in $\rho(T)$ for a spin glass (see section 6.2.5) for $T>T_f$ and may be indicative of the clustering of the terbium moments before the ordering takes place. The fact that there is still a sharp

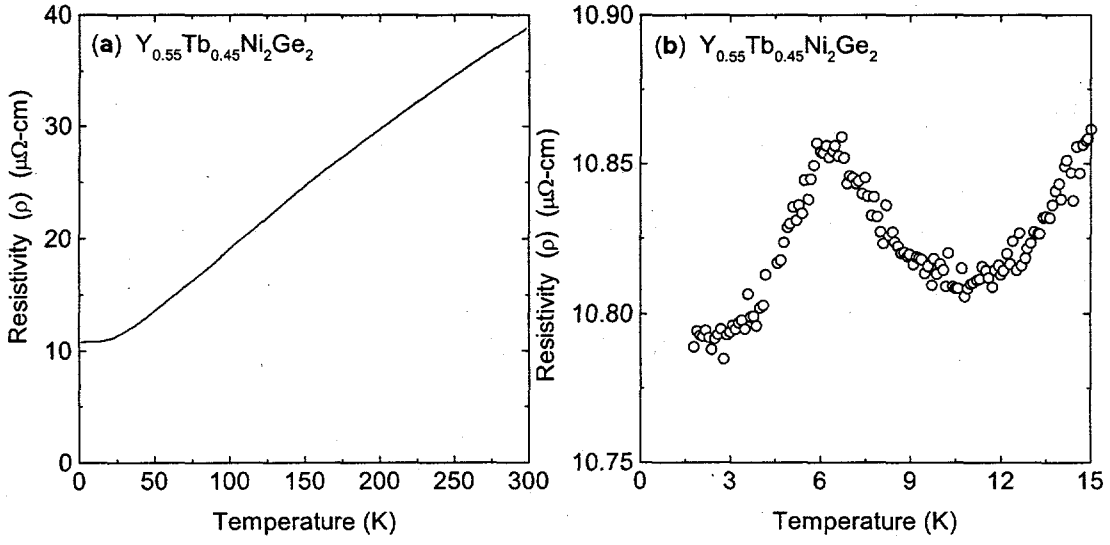

Figure 5.18. (a) Zero-field resistivity as a function of temperature for composition x = 0.45. (b) Low temperature part of the zero-field resistivity.

feature in the resistivity at T_N is consistent with an actual long range order. Also recall that the resistivity for x = 0.60 was also curiously flat just above T_N. That could mean that cluster formation is beginning even in that concentration, though not to the extent seen here.

The magnetic specific heat is shown in Figure 5.19(a). The peak is still fairly sharp and is located at about 6.15±0.1 K which is similar to the value found in the d(χT)/dT. the low temperature specific heat has a $T^{3/2}$ dependence, similar to the x = 0.60 sample, and this was extrapolated to 0 K to determine the magnetic entropy (b). The high temperature entropy is similar to that seen before. At the transition temperature, almost all of the Rln2 entropy of the doublet ground state is frozen out.

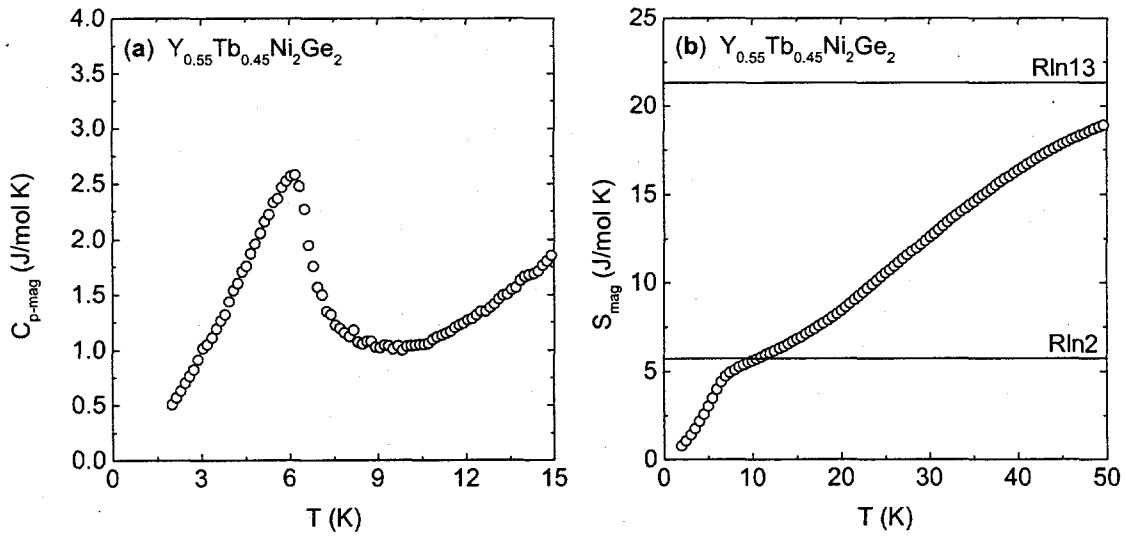

Figure 5.19. (a) Magnetic contribution to the specific heat as a function of temperature for composition x = 0.45. (b) Magnetic entropy as a function of temperature. The solid line shows value of Rln13 and Rln2.

Before continuing on to region IV it is perhaps useful to try to determine where the boundary line is between regions III and IV. This was accomplished by comparing $d(\chi T)/dT$ for fc and zfc data for each concentration. This is seen in Figure 5.20 for concentrations (a) x = 0.40, (b) x = 0.375, (c) x = 0.35, and (d) x = 0.30. For the x = 0.40 composition there is very little difference between fc and zfc data, which has been the case for all higher concentrations as well. The sharp peak corresponds to a transition temperature of $T_N = 4.7$ K.

A divergence between fc and zfc data begins to form for the 0.375 composition near the transition, which in this case is 4.2 K. A sharp peak is still clearly seen in both fc and zfc data. In (c) no sharp peak is observed in the fc data and the data levels off into a plateau while there is still a prominent peak in the zfc data. Likewise for x = 0.30, there is a plateau rather than a peak in fc data and a prominent peak in the zfc data. The scattered points at the lowest temperatures is due to performing a derivative at with nonuniform temperature spacing. In this region the difficulty in stabilizing the temperature of the SQUID (around 2.2 K) leads to large changes in the zfc susceptibility because of its time dependence in the spin glass state. Due to the lack of a peak in the fc data which also leads to the divergence between zfc and fc data, it is determined that concentrations of x = 0.35 and below lie in region IV and concentrations above that lie in Region III.

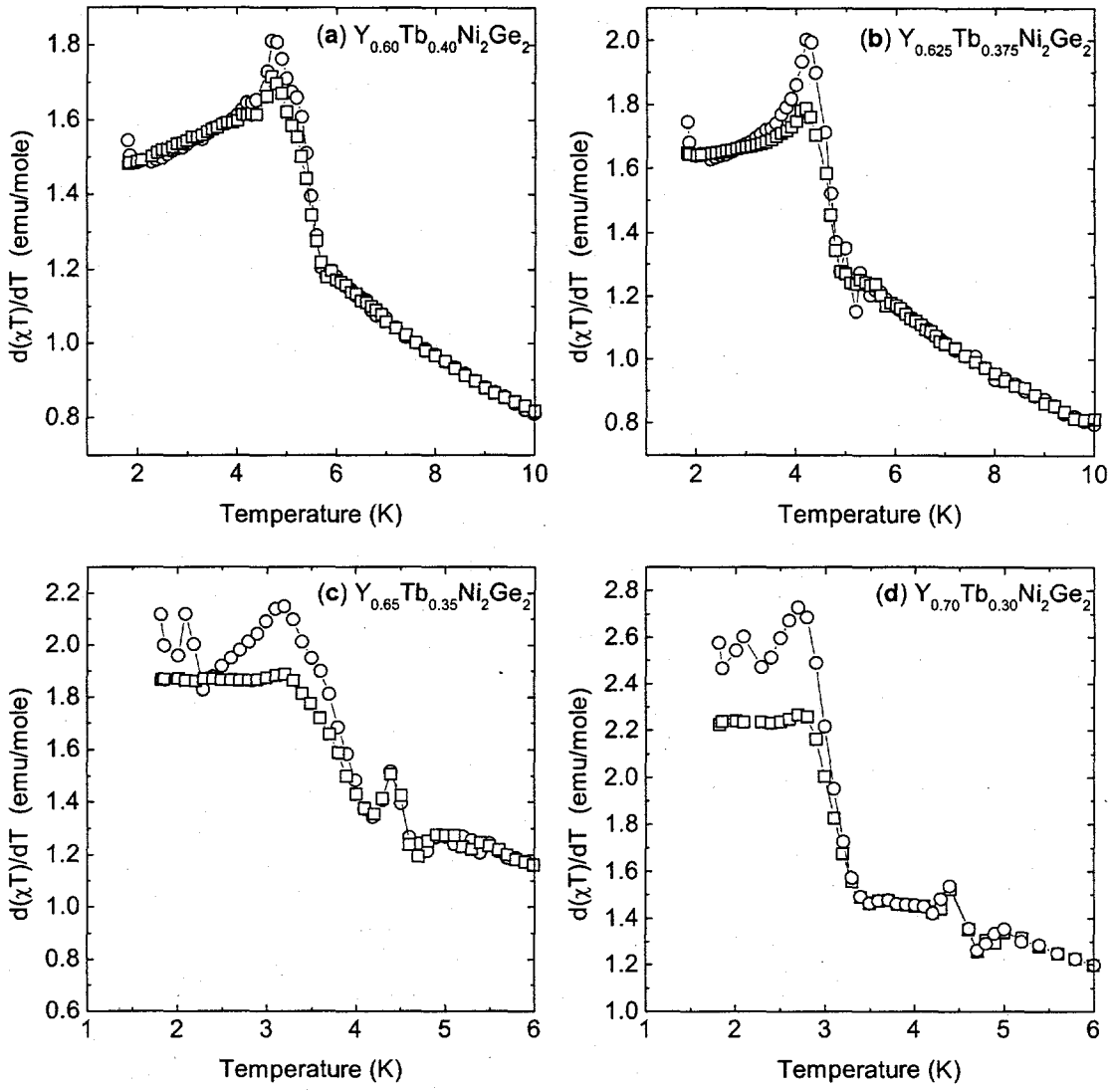

Figure 5.20. Plots of d(χT)/dT for zfc (circles) and fc (squares) for H||c at 50 Oe. (a) At x = 0.40 there is not much difference between fc and zfc data and sharp peak determines T_N = 4.7 K. (b) For x = 0.375 the difference is greater and there is still a sharp peak in the fc data corresponding to T_N = 4.2 K. (c) At x = 0.30 the difference is very great and there no strong peak in fc, just a plateau. (d) Likewise for x = 0.25, big difference between fc and zfc data and no peak in fc data.

5.7. Conclusion

In this chapter, some of the experimental features of the $Tb_xY_{1-x}Ni_2Ge_2$ series have been explored for the higher terbium concentrations (x). Before examining the results for the lowest concentrations, it might be worthwhile to summarize what has been discussed up to this point. It has been seen that the antiferromagnetic order that exists in the $TbNi_2Ge_2$ compound is systematically suppressed with the substitution of yttrium for terbium. The transition from the paramagnetic state to the incommensurate antiferromagnetic state, T_N, decreases linearly with x whereas the transition into the commensurate state appears to decrease much more rapidly and in a nonlinear fashion. The Weiss temperatures (θ), as determined from fitting the high temperature DC susceptibility, also change linearly. This is true for $\theta_{||}$ and may be true as well for $\theta_{\perp}$ though experiments with the crystals better aligned with respect to the field will be needed to be sure. These results are typical of dilution series and demonstrate the scaling of the magnetic interactions with the deGennes factor.

A new feature is the presence of irreversibilities as detected from low field χ_{ZFC} and χ_{FC} measurements with respect to temperature. At high concentrations these irreversibilities may arise from domains or structural defects in the crystals, though this conjecture has not been verified by experiment. At lower concentration these irreversibilities take on more of the characteristics of frustrated moments, though not yet a spin-glass. In the next chapter these irreversibilities will be shown to become a spin-glass state in the next set of concentrations.

6. IS DILUTE $Y_{1-x}Tb_xNi_2Ge_2$ A SPIN GLASS ?

6.1. Introduction

In this section the physical properties of $Y_{1-x}Tb_xNi_2Ge_2$ in lower concentration ($x<0.375$) region will be examined in greater detail. It is in this dilution range that the system displays many of the attributes that are common to other spin glass systems. Many of these characteristics were discussed in chapter 2, where the physical interactions which these attributes are the consequences of, were discussed. It will be shown that this system does indeed display these experimental signatures of spin glasses for $x < 0.375$ and this system will be compared to other well characterized spin glasses.

6.2. Characterization of a Spin Glass

6.2.1. DC Magnetization below T_f

In Figure 6.1 the dc susceptibility is shown for $Y_{1-x}Tb_xNi_2Ge_2$ for (a) $x = 0.25$, (b) 0.30, and (c) 0.35, measured in an applied field of 50 Oe. All three data sets display a spin-glass-type freezing transition in the dc susceptibility. The freezing temperature T_f is defined as the peak in the zfc magnetization, which for these concentrations are 2.5±0.1 K, 3.0±0.1 K, and 3.7±0.1 K respectively. Below T_f, the zfc susceptibility decreases with temperature whereas the fc susceptibility is nearly temperature independent. Figure 6.1(d) displays this irreversibility in a plot of the difference between zfc and fc data

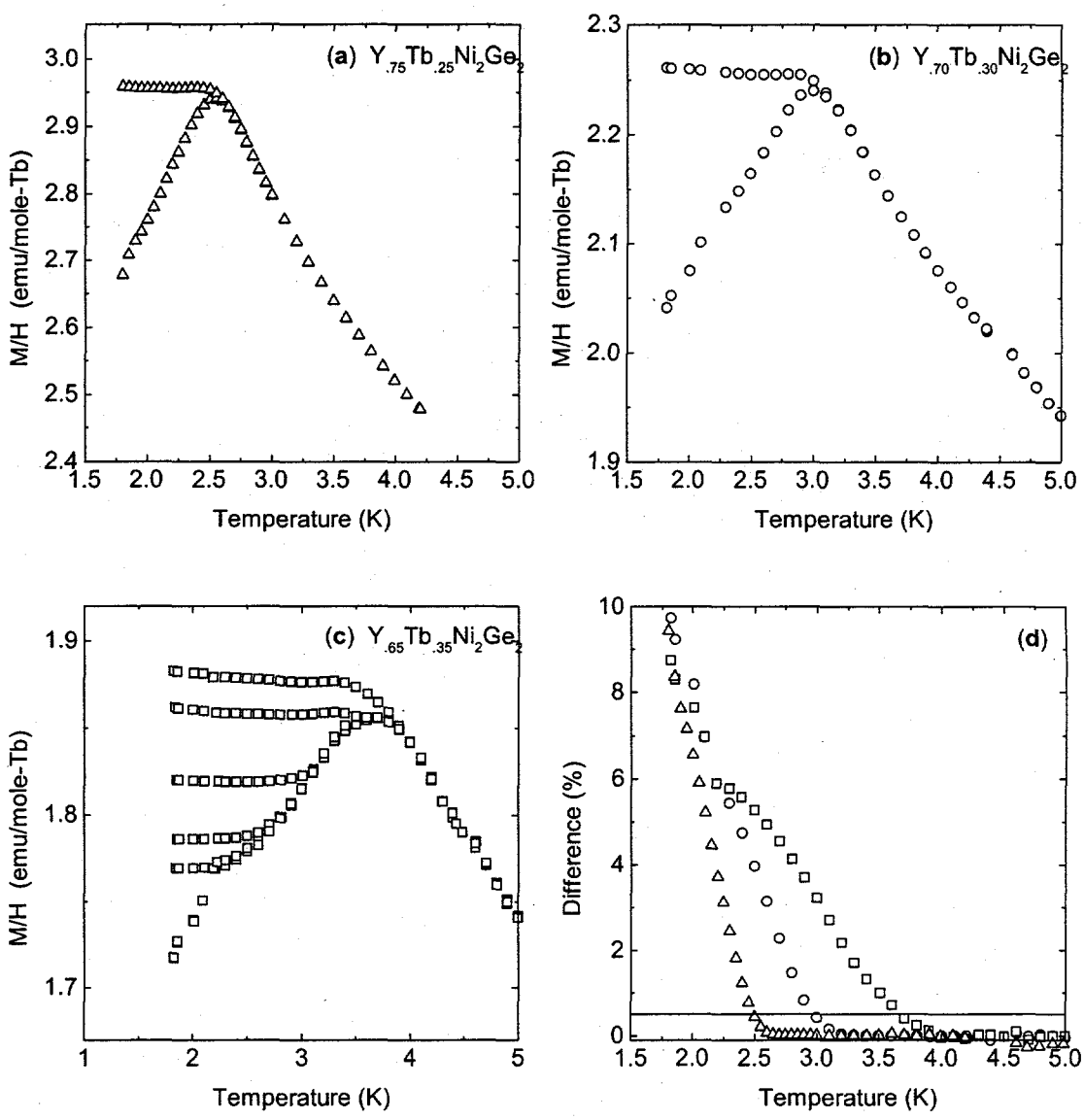

Figure 6.1. The low temperature dc susceptibility of $Tb_xY_{1-x}Ni_2Ge_2$ with (a) x = 0.25, (b) x = 0.30, and (c) x = 0.35 in an applied field of 50 Oe for both zero-field-cooled (zfc) and field-cooled (fc) histories. Also shown in (c) are fc data from temperatures of 2.2, 2.6, 3.0, and 3.5 K following an initial zfc (as described in text). (d) shows the difference between fc and zfc data as a percentage of the fc value, from which T_f is determined (as described in text). The solid line represents the 0.5 % criterion.

with respect to temperature. In the same manner as in chapter 5, the irreversibility temperatures (T_{ir}) were determined by a 0.5% criterion, the temperature where the difference between zfc and fc data is 0.5%, and these are similar in value to the T_f's. Figure 6.1(c) also shows the effect on $Tb_{0.35}Y_{0.65}Ni_2Ge_2$ of zero-field cooling to 1.8 K, warming to $T'<T_f$ in a field of 50 Oe, field cooling back to 1.8 K, and warming again to another $T'<T_f$, repeating this for values of T' = 2.2 K, 2.6 K, 3.0 K, and 3.5 K. The magnetization of the sample while warming from 1.8 K, after field cooling from T', is nearly temperature independent up to T' after which it falls on the original curve traced out by the zfc magnetization. This behavior is consistent with the existence of many metastable states, as expected for a spin glass (Fisher, 1999; Mydosh, 1993).

It should be noted that below T_f the zfc magnetization is strongly dependent on relaxation processes. These processes will be looked at in greater detail in following paragraphs. This relaxation is the cause of the kink in the x = 0.35 data set at 2.2 K. This temperature is close to the lambda point (T = 2.19 K) in liquid helium where there is a change from ordinary liquid helium to liquid helium II, which exhibits superfluidity. Temperature control for the magnetometer is not optimized at this point and the time duration for the temperature to stabilize here can be quite long. This results in an extended period of time between this measurement and the previous measurement, which allows the relaxation processes to make a more prominent contribution than normal. This problem was avoided to some extent in later measurements by skipping past this temperature altogether.

Figure 6.2 shows the low temperature part of the inverse susceptibility as a function of temperature for several concentrations. For (a) x = 0.40 the inverse susceptibility has a positive curvature at low temperatures. This is consistent with what is seen for higher concentrations, for example $TbNi_2Ge_2$ seen in Figure 5.1(b) up to the transition. As the concentration is lowered into region IV, this curvature flattens out as in (b) x = 0.35, and then curves below the line for smaller concentrations. This demonstrates the antiferromagnetic short range correlations and clustering that is taking place well above T_f. The solid lines in the figure are linear fits to the data for a short temperature region (~2 K) just above the region shown for each plot and are drawn to make the curvature clearer to see.

The dc susceptibility (M/H) was studied for a range of applied fields for samples containing terbium concentrations of 30 and 35 %. Figures 6.3(a) and (c) show these results at a few selected fields. In low applied fields, a sharp peak is seen in the zfc magnetization, but in higher fields a significant broadening and flattening of this peak occurs. This effect has been seen for other spin glasses (Chamberlin, 1982; Fisher, 1999). The non-linearity of the magnetization with applied field close to the spin freezing transition is explored in more detail in section 6.2.3. The irreversibility temperature also decreases as the field is increased and shifts from being located at temperatures near the peak in the zfc data to temperatures lower than the center of the flattened peak. The features at low temperatures (~2.2 K) are due to the problem mentioned earlier and hinders the evaluation of irreversibility temperatures below this point.

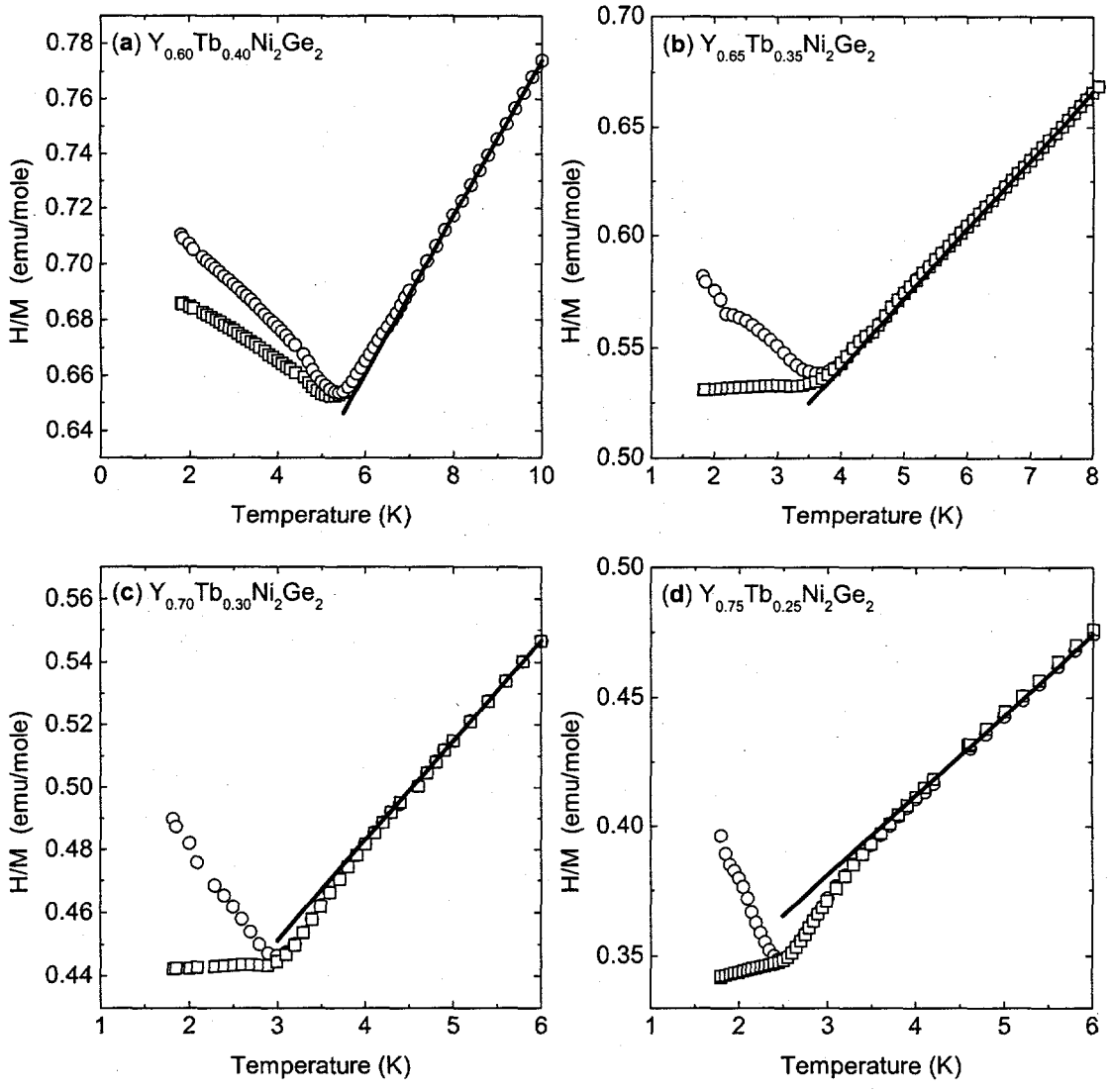

Figure 6.2. Plots of the low temperature part of the inverse susceptibility (H/M) for (a) x = 0.40, (b) x = 0.35, (c) x = 0.30, and (d) x = 0.25 showing the effects of antiferromagnetic clustering. The solid lines are guides to the eye (see text).

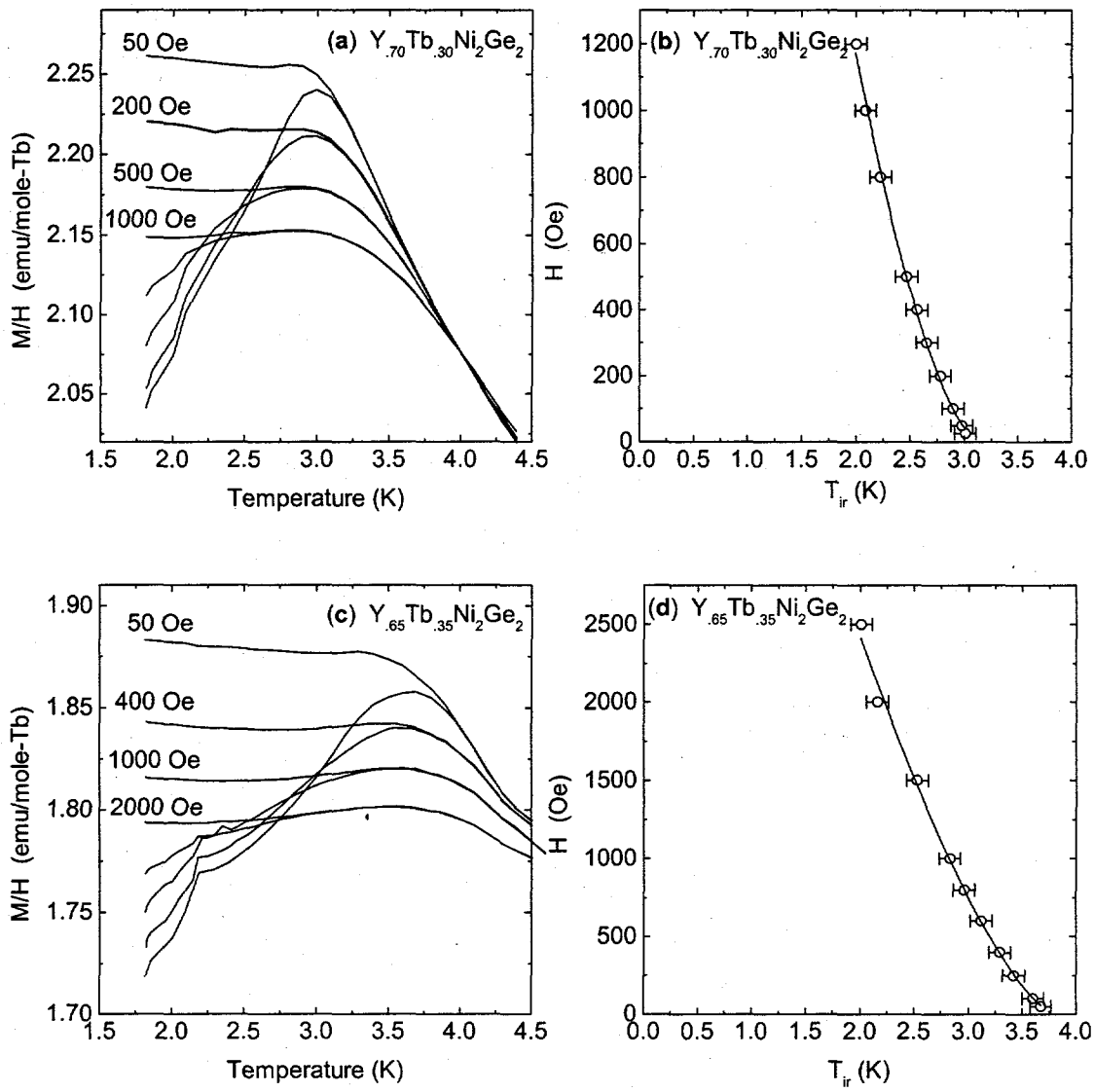

Figure 6.3. Low-temperature zfc and fc dc magnetization for various applied fields. (a) shows data for x = 0.30 and H = 50, 200, 500, and 1000 Oe, and (c) shows similar data for x = 0.35 and H = 50, 400, 1000, and 2000 Oe. (b) and (d) show the field dependence of T_{ir} for x = 0.30 and 0.35 respectively. Lines in (b) and (d) are fits to Eq 6.1.

The applied magnetic fields are plotted as a function of T_{ir} in (b) and (d). The data are well fitted by the de Almeida-Thouless equation, which is derived from mean field theory for an Ising spin glass with infinite range random interactions (Binder, 1986),

$$H(T_{ir}) = \alpha\left(1 - \frac{T_{ir}}{T_f}\right)^{3/2}, \qquad (6.1)$$

allowing α and T_f to be fitting parameters. Fits are shown as solid lines in (b) and (d). Values are $\alpha = 5.4\pm0.1 \times 10^3$ Oe and $T_f = 3.11\pm0.01$ K for x = 0.30 and $\alpha = 7.4\pm.2 \times 10^3$ Oe and $T_f = 3.83\pm.03$ K for x = 0.35. The values of T_f from this fit are similar to the values obtained from the peak in the zfc magnetization in an applied field of 50 Oe, though a little larger. It is possible that measurements in lower applied fields, for example 20 Oe, would more closely approximate the T_f values produced from this fit. This variation of $H(T_{ir})$ is typical of many spin glass systems, such as Tb-Mg-Zn quasicrystals (Fisher, 1999) and $Fe_xMn_{1-x}TiO_3$ (Katori, 1994).

According to theory, the coefficient α is a function of the averaged exchange interaction, J_0/J. In the ideal spin glass the ferromagnetic interactions compete with the antiferromagnetic interactions and $J_0/J = 0$. For this case the theoretical value of α is given as

$$\alpha_{th} = \sqrt{\frac{4}{3}}\frac{k_B T_f}{g\mu_B J}, \qquad (6.2)$$

where J is the total angular momentum. For $Tb_xY_{1-x}Ni_2Ge_2$, g = 1.5 and J = 6x. This gives values of $\alpha_{th} = 1.98\times10^4$ Oe for x = 0.30 and $\alpha_{th} = 2.09\times10^4$ Oe for x = 0.35. These

values are approximately three times larger than the experimentally found values, which is not uncommon and may be due to $J_0/J \neq 0$ (Katori, 1994).

6.2.2. AC Magnetic Susceptibility

The in-phase component χ' and the out-of-phase component χ'' of the ac magnetic susceptibility were measured from 1.8 to 8 K with no bias field and a 1 Oe ac field with frequencies of 1, 10, 100, and 1000 Hz. The results of this are shown in Figure 6.4 for compositions (a) x = 0.25, (b) x = 0.30, and (c) x = 0.35 for χ'. As was seen in the zfc dc magnetization, there is a sharp peak which can be used to define the freezing transition temperature, T_f. The dc magnetization for these samples is also included for comparison, but is not intended to be thought of as a zero frequency limit to the ac susceptibility. In Figure 6.4(d) the χ'' component of ac susceptibility is shown for all three samples for a frequency of 1 Hz.

For all three samples, the peak in χ' moves to higher temperatures with increasing frequency. From this the fractional relative change in freezing temperature per decade change in frequency, $\Delta T_f/(T_f \Delta \log_{10} f)$ can be calculated, where ΔT_f is the change in T_f for the given change in frequency ($\Delta \log_{10} f = 3$ for these data). For these samples $\Delta T_f/(T_f \Delta \log_{10} f) = 0.045$, 0.030, and 0.012 for x = 0.25, 0.30, and 0.35 respectively. These values are similar to those of other canonical spin glasses (*Cu*Mn ~ 0.005, *Ni*Mn ~ 0.18, (*La*Gd)Al_2 ~0.06) (Mydosh, 1993) as well as that of the Tb-Mg-Zn quasicrystal (0.049) (Fisher, 1999).

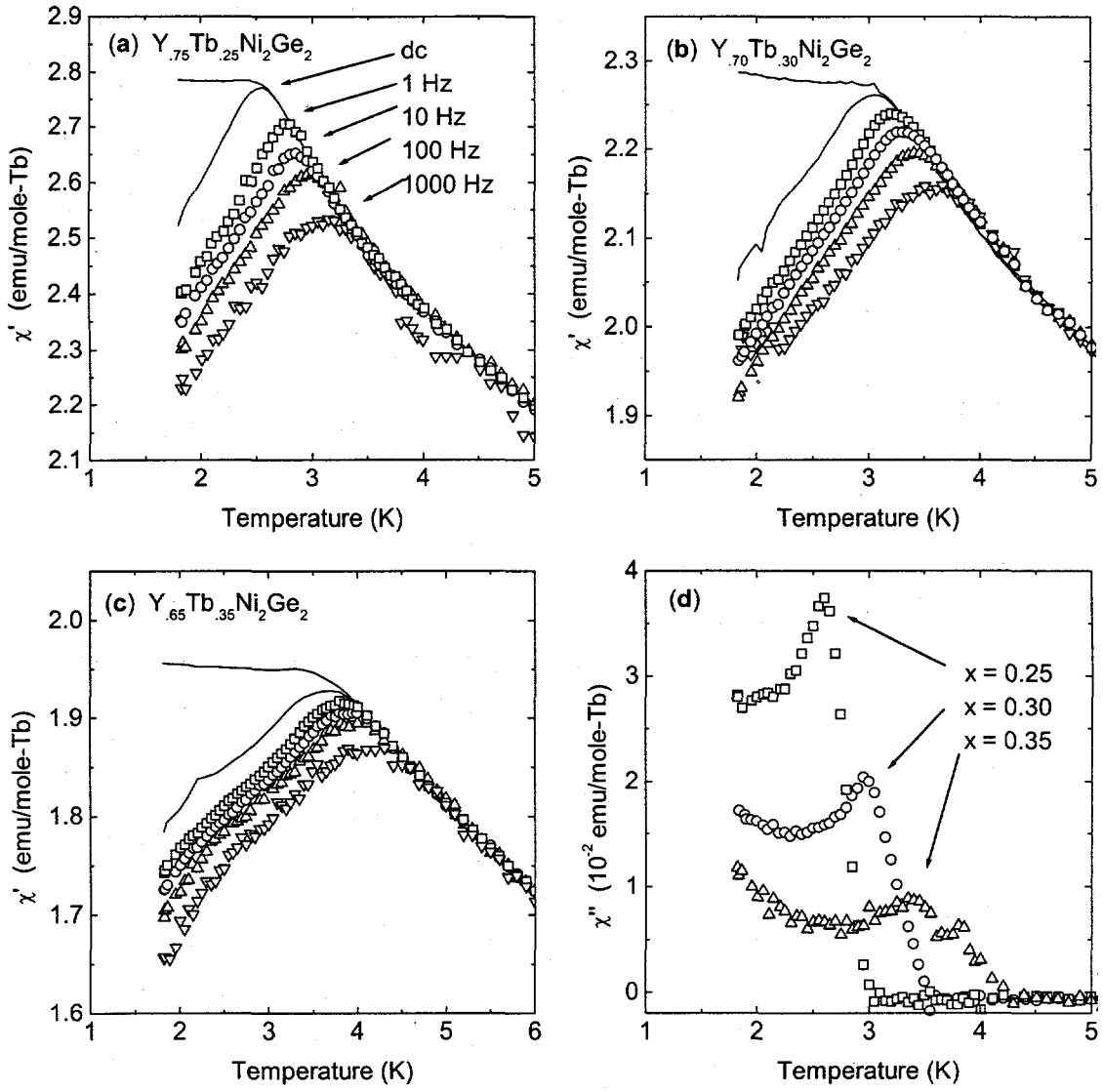

Figure 6.4. The real part, χ', of the zero-field ac susceptibility for different applied frequencies from 1 to 1000 Hz (listed in figure) for (a) x = 0.25, (b) x = 0.30, and (c) x = 0.35. dc magnetization measured in 50 Oe is also shown for all three samples. (d) shows the imaginary part, χ'', for all three samples for an applied frequency of 1 Hz.

The frequency dependence of T_f for these crystals can be fitted to the Arrhenius law for thermal activation, $f = f_0 \exp(-E_a/(k_B T_f))$ (Figure 6.5 (a)). This produces unphysically large of the prefactor f_0 and the activation energy E_a/k_B, which for these samples are found to be 10^{23}Hz and 148 K, 10^{34} Hz and 258 K, and 10^{81} Hz and 723 K for x = 0.25, 0.30, and 0.35 respectively. These numbers are comparable to those found for the Tb-Mg-Zn quasicrystals (Fisher, 1999), but are smaller than some canonical spin glasses (Mydosh, 1993). In general a better description of the experimental data can be obtained by using the Vogel-Fulcher law

$$f = f_0 \exp\left(\frac{E_a / k_B}{T_f - T_0}\right) \tag{6.3}$$

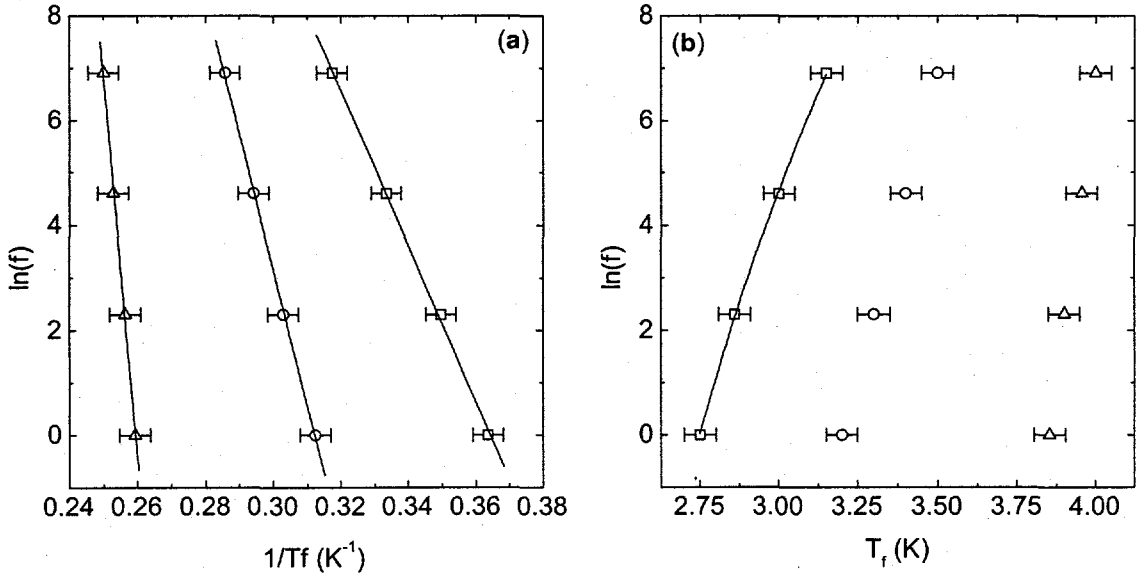

Figure 6.5 (a) shows plots of ln(f) vs $1/T_f$, with solid lines showing fits to an activation energy analysis (see text). (b) shows plots of ln(f) as a function of T_f, with solid line showing fit to the Vogel-Fulcher law for x = 0.25 (see text). compositions shown are x = 0.25 (squares), x = 0.30 (circles), and x = 0.35 (triangles)

data for x = 0.25 (Figure 6.5(b)) were fit in this way and the following values were found: $\ln(f_0)$ = 33.5±8.2, E_a/k_B = 51.8±28.5 K, and T_0 = 1.2±.5 K. These are slightly more reasonable values than those found above, but the error bars involved are rather large and very little can actually be determined from these values. For the samples x = 0.30 and x = 0.35 it proved too difficult to fit the data in this way. The change in T_f is small ($\Delta T_f <$ 0.5 K) and comparable to the uncertainty in the measurements (~0.1 K), that no stable fitting solution could be found. Much finer temperature control and a larger frequency range would be required to overcome this difficulty.

The out-of-phase component χ''(Figure 6.4(d)) also behaves in a manner consistent with other spin glasses (Binder, 1986). Above T_f χ'' is vanishingly small but is nonzero below T_f. This implies that there are relaxation processes that are affecting the measurement. As in other spin glasses, the maximum slope of χ'' corresponds to the peak in χ', and it also increases in temperature as the frequency increases.

6.2.3. Non-Linear Susceptibility

Up to this point, these samples display the hallmarks of spin-glass behavior. It is possible though that this behavior may arise from a blocking of superparamagnetic clusters (Binder, 1986). An important measurement that is useful in discerning between these two cases is to observe the temperature dependence of the third-order magnetic susceptibility χ_3.

The nonlinear susceptibility can be defined in terms of the ac susceptibility χ and applied magnetic field H as

$$\chi = \chi_1 - \chi_3 H^2 + \chi_5 H^4 - \chi_7 H^6 + \chi_9 H^8 + O(H^{10}) \qquad (6.4)$$

where χ_1 is the first-order or linear susceptibility, χ_3 is the third-order and so on. There are other slightly different ways of defining the nonlinear susceptibility and in measuring it, which have been covered in Chapter 2.

In order to determine χ_3, ac susceptibility as a function of applied field (H) were performed on $Tb_{0.30}Y_{0.70}Ni_2Ge_2$ and $Tb_{0.35}Y_{0.65}Ni_2Ge_2$ with an ac field of 3 Oe and a frequency of 1.5 Hz between 2.5 and 7 K and bias fields (H) between –400 Oe and 400 Oe. Examples of $\chi'(H)$ for temperatures just greater than T_f are shown in Figure 6.6(a) for x = 0.30 and (b) for x = 0.35. It is clear that parabolas with higher order corrections should give a good account of the data. Fits to the data were performed using the first

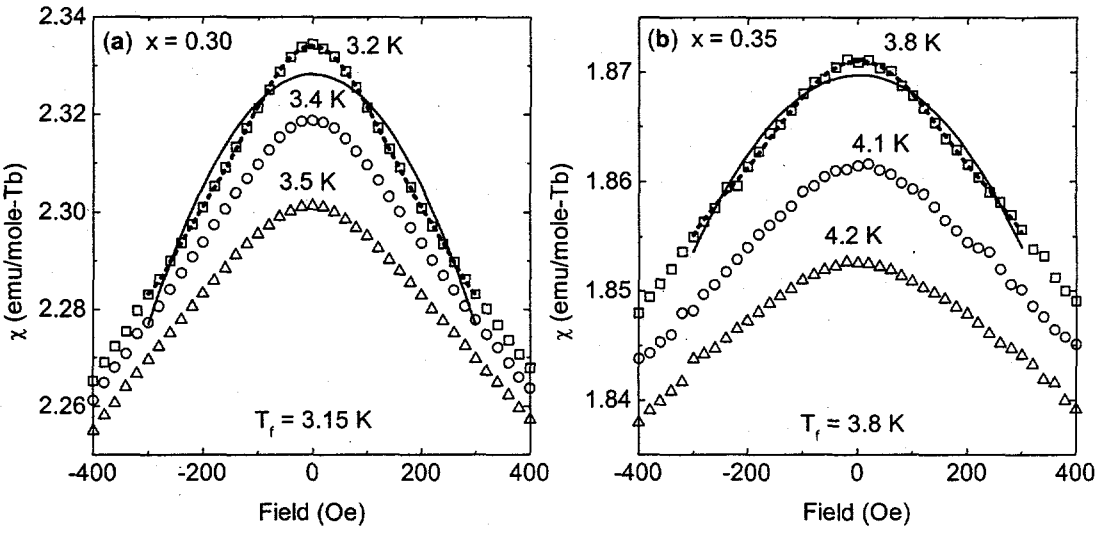

Figure 6.6 (a) shows the real part, χ', of the ac susceptibility as a function of field for x = 0.30 at T = 3.2 K (squares), 3.4 K (circles), and 3.5 K (triangles). (b) shows $\chi'(H)$ for x = 0.35 at T = 3.8 K (squares), 4.1 K (circles), and 4.2 K (triangles). The solid line shows the fit of Eq 6.4 with terms higher than H^2 suppressed and dashed line shows fit with the higher terms for (a) T = 3.2 K and (b) T = 3.8 K.

five terms in Equation. 6.4 for x = 0.30 and the first four terms for x = 0.35 and modifying H to H + h, where h is a correction term to account for any residual or persistent magnetic fields in the magnetometer. The effects of these small persistent fields have previously been seen in the low field magnetization measurements as mentioned in Chapter 3. The results of fitting for x = 0.30 at T =3.2 K and for x = 0.35 at T = 3.8 K are shown in Table 6.1. Though small, the terms proportional to H^4 and H^6 and H^8 do contribute significantly to the measurement. This can be seen in the solid lines in both Figure 6.6(a) and (b), which are fits to the data with terms higher than χ_3 suppressed to zero and the dashed lines which are fits that include the higher terms. Clearly, the higher terms are necessary.

Figure 6.7 shows the temperature dependence of each term in the nonlinear susceptibility for (a) x = 0.30 and (b) x = 0.35. T_f was determined by the peak in χ_1 for each of these samples and were found to be T_f = 3.15 for x = 0.30 and T_f = 3.8 for x = 0.35. These values are about 0.1 K higher than those found for dc measurements but

Table 6.1. Values of the nonlinear susceptibility for concentrations (x) and temperatures as listed. χ_9 for x = 0.35 was to small to be measured.

	x = 0.30, T = 3.2 K	x = 0.35, T = 3.8 K
χ_1 (μ_B/mole-Tb)	2.334±.001	1.871+0.001
χ_3 (μ_B/mole-Tb Oe^2)	$(1.488\pm0.02)\times10^{-6}$	$(3.51\pm0.13)\times10^{-7}$
χ_5 (μ_B/mole-Tb Oe^4)	$(2.63\pm0.12)\times10^{-11}$	$(3.44\pm0.37)\times10^{-12}$
χ_7 (μ_B/mole-Tb Oe^6)	$(2.92\pm0.22)\times10^{-16}$	$(1.66\pm0.28)\times10^{-17}$
χ_9 (μ_B/mole-Tb Oe^8)	$(1.26\pm0.12)\times10^{-21}$	----------

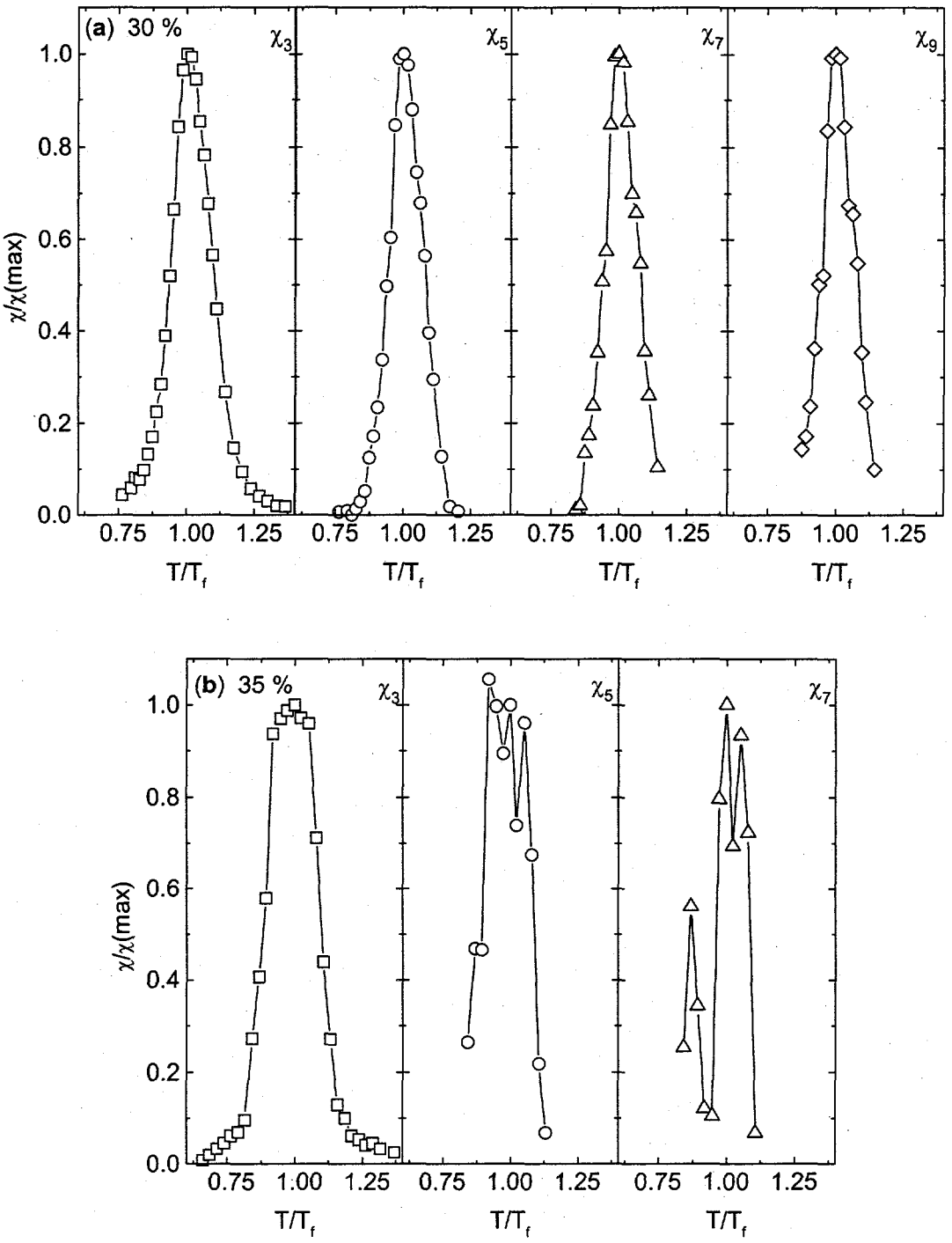

Figure 6.7. Nonlinear susceptibility in $\chi'(H)$ for (a) x = 0.30 and (b) x = 0.35 as a function of reduced temperature T/T_f. Lines are drawn to guide the eye.

recall that T_f increases with frequency. The narrowness of the peak in χ_3 near T_f is strong evidence that the cusps seen in the dc magnetization and in χ' do correspond to a spin-glass freezing and not to the blocking of superparamagnetic clusters as was seen in Figure 2.12 (Bitoh, 1996).

According to theory, the nonlinear susceptibility above T_f should exhibit the critical divergence and exponents of a spin glass (Mydosh, 1993). Unfortunately the critical components cannot be extracted from this data. The noise present in χ_5 and χ_7 for $x = 0.35$ may be due to the small sample used, giving a significantly smaller signal to fit, whereas the $x = 0.30$ sample was much bigger. It may also be possible that the $x = 0.35$ concentration is too close to the arbitrarily chosen boundary of the crossover region ($0.375 < x < 0.45$) and other unknown interactions are occurring.

Figure 6.8 shows a comparison of the temperature dependence χ_3 scaled as T/T_f for concentrations $x = 0.30$ and $x = 0.35$ alongside χ_3 for Tb-Mg-Zn and Ho-Mg-Zn quasicrystals similarly scaled, measured by an ac technique (Fisher, 1999).The similarities in the width of these peaks, especially for $x = 0.30$, demonstrates that these systems do compare well with other known spin glass systems. The slightly broader width in the $x = 0.35$ sample may again be an indication of being too close to the crossover region.

6.2.4. Relaxation and Remanence Effects in the DC Magnetization

Another feature common to spin glass systems is the existence of relaxation processes below the freezing temperature that cause the magnetization to have a time dependence. This has already been seen to some extant in the features that appear at 2.2

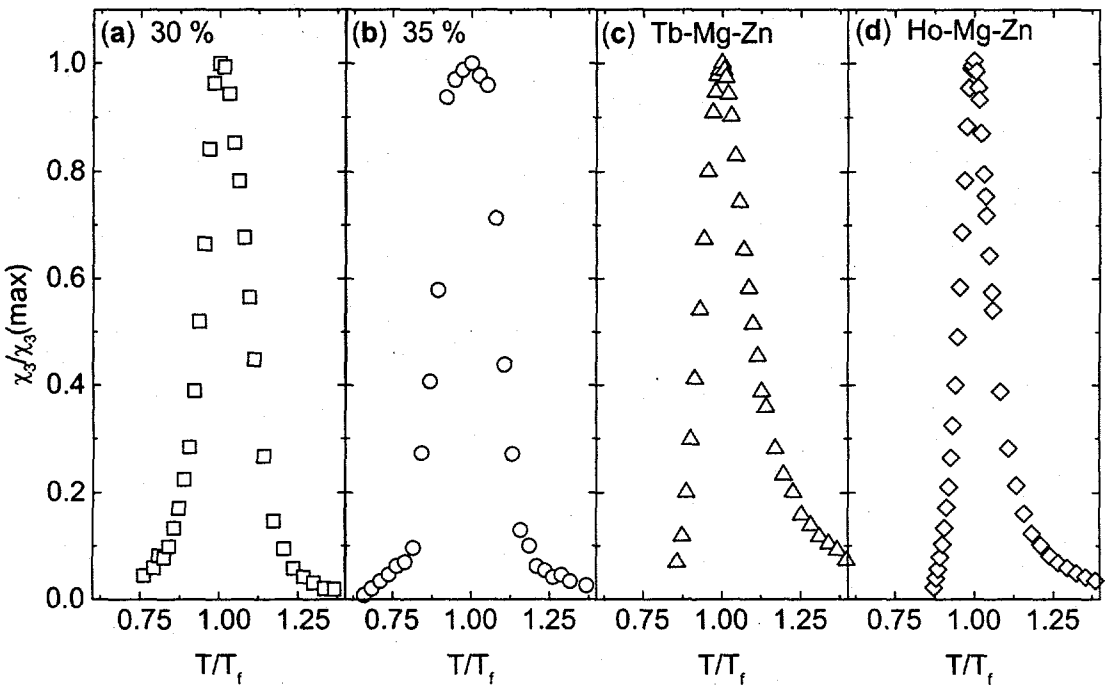

Figure 6.8. Comparison of χ_3 for four different spin glass systems. (a) and (b) are from this study for x = 0.30 and 0.35and (c) and (d) are from (Fisher, 1999).

K for the reasons mentioned previously. These relaxation process also give rise to the nonzero χ'' below T_f. These relaxation processes are an extensive problem and are beyond the scope of this work, but some initial measurements have been made to demonstrate their properties.

Figure 6.9(a) shows the time dependence of the magnetization for both zfc and fc histories in a field of 50 Oe at 2 K for terbium concentrations of x = 0.30 and (b) shows time dependence of the thermoremanent magnetization (TRM) for x = 0.30. For the zfc data, the sample was cooled to 2 K and then the field of 50 Oe was applied immediately after the temperature was stabilized. For the fc data a field of 50 Oe was applied at 30 K

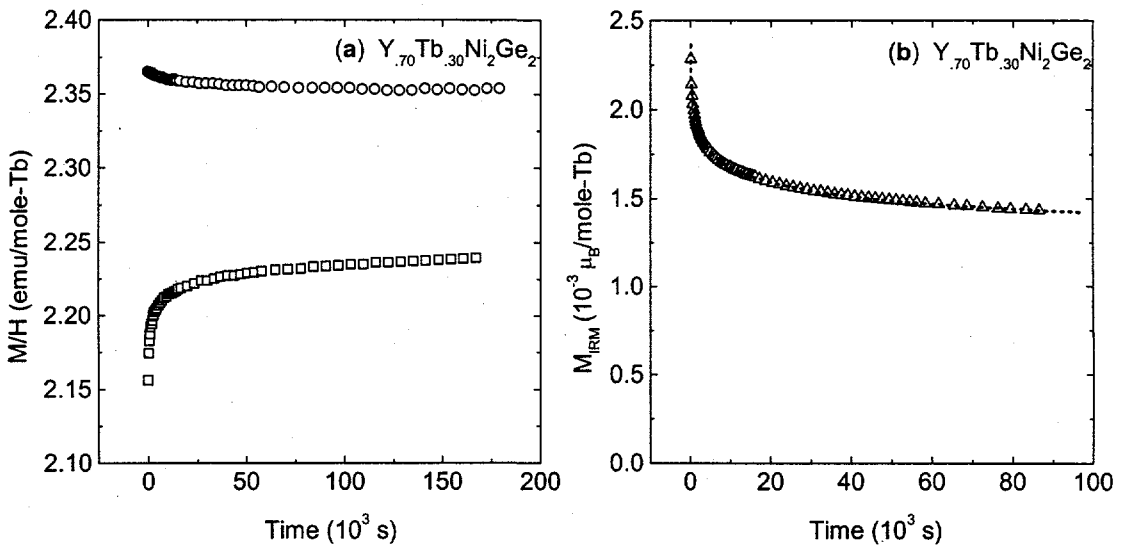

Figure 6.9. (a) Time dependence of the zfc (squares) and fc (circles) magnetization in an applied field of 50 Oe. (b) Time dependence of the TRM (triangles) after cooling in an applied field of 50 Oe. Dashed line shows fit to Equation 6.5 with values from column 4 of Table 6.2

and then the sample was cooled to 2 K. The TRM followed the fc history to 2 K and the field returned to zero. At the end of the run the sample was heated to 4.2 K, which is in the paramagnetic region for this sample and the magnetization drops immediately to its saturation value. This was done because of the already mentioned difficulties of measuring in a small field. If the applied field is not actually zero, then the TRM will not relax to zero but rather to nonzero value determined by the small residual field. By heating to above the freezing temperature and into the paramagnetic region, the magnetization due to this small residual field may be determined.

Measurements using the SQUID magnetometer take on the order of 1 minute, and the applied field takes about 1 minute to stabilize. Therefore any relaxation processes with time constants on the order of 1 minute or less cannot be observed with this

particular technique. Still, the data shown in Figure 6.9 demonstrate relaxation processes with time constants greater than the experimental resolution. In (a), it is noticed that the zfc and fc data, though relaxing towards each other, do not seem to be saturating to the same value, producing a large gap between the two sets of data. Similar results were obtained for Tb-Mg-Zn quasicrystals. This data may imply that the potential energy barriers between the closely spaced energy levels of the system are rather high (Fisher, 1999).

The TRM data seen in (b) was fitted by a modified stretched exponential function

$$M_{TRM}(t) = A\exp\left\{-\left(t/\tau\right)^{\beta}\right\} + S\ln(t) + \delta, \qquad (6.5)$$

where the first term is the stretched exponential function and the second term is an additional logarithmic decay term, and δ is the magnetization leftover after heating above T_f(Nordblad, 1986).

The data was fit with S = 0, in order to fit the data to a pure stretched exponential, and with S as a free parameter in order to see if the data is better described with or without the second term. For unknown reasons, the data is very difficult to fit accurately. Since measurements with the magnetometer take on the order of 1 minute, all fits were taken at times above 200 seconds in order to avoid the potential error in the first few data points. Fits to the data taken over different time intervals resulted in different values for the parameters. This is seen in Table 6.2 where the results of fitting over time intervals of 200 <t< 30,000 seconds and of 200 <t< 60,000 seconds are shown for fits with and without S. The results for the two fits with S = 0 show large variations in all the parameters, especially in τ which changes from 1582 to 4.5 seconds. The results for the

Table 6.2. Values of the parameters in equation 6.5.. Column (1) is stretched exponential for time interval 200-30000 seconds, column (2) is stretched exponential for time interval of 200-60000 seconds, column (3) is modified stretched exponential for time interval 200 – 30000 seconds, column (4) is modified stretched exponential for time interval 200-60000 seconds.

	1	2	3	4
A (10^{-3} μ_B/mole-Tb)	4.06	6.19	2.59	2.81
τ (seconds)	1582	4.5	3038	2907
β	0.084	0.060	0.196	0.170
S (10^{-5} μ_B/mole-Tb)	0	0	5.73	4.80
δ (10^{-4} μ_B/mole-Tb)	4.122	4.122	4.122	4.122

two fits with S a free parameter also show some variation between them but not so severe. This indicates that the data is better fit with the both terms rather than just the stretched exponential, which has also been seen for other spin glasses, such as *Cu*Mn (Nordblad, 1986).

The fit value of β (determined with $S \neq 0$) of $\beta = 0.33$, which was found for *Cu*Mn with a time interval of 1000 seconds by measuring the relaxation of the IRM as a function of time (Chamberlin, 1984), but is similar to the value found for Tb-Mg-Zn (0.18), which was determined form a zfc measurement similar to that seen in Figure 6.9(a) (Fisher, 1999). In any case, the nonunitary value of β indicates that there are several relaxation processes involved, and is typical for spin glasses (Mydosh, 1993).

A study of the isothermal remanent magnetization (IRM) and the thermoremanent magnetization (TRM) was performed on both $x = 0.30$ and $x = 0.35$ concentrations. The IRM was performed by zero-field cooling the sample from 30 K to 2 K, immediately applying a field H, and then immediately removing the field and measuring the remanent

magnetization. The TRM was measured by applying a field H at 30 K, cooling to 2 K, then removing the field and immediately measuring the remanent magnetization. As mentioned before, the SQUID magnetometer takes on the order of 1 minute to perform each of these steps. This is significantly shorter than the τ observed in the stretched exponential in the preceding paragraphs, but faster relaxation processes cannot be determined. Figure 6.10(a) shows the IRM and TRM of x = 0.30. The IRM and TRM appear to reach a common saturation value of about 0.005 μ_B/Tb for fields greater than 4 kOe. Similarly for x = 0.35 (b), the two data sets seem to saturate at 0.01 μ_B/Tb for applied fields greater than 6 kOe. The IRM and TRM of both of these samples are similar in form to those of other spin glasses (Mydosh, 1993; Fisher, 1999). The slight differences in shape between these two samples, particularly for the IRM curves, may be

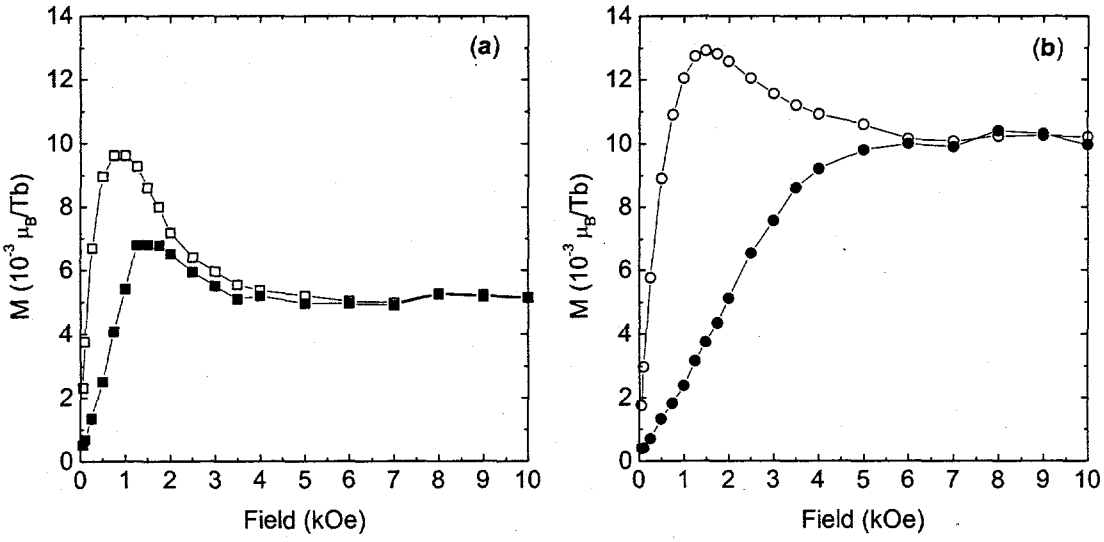

Figure 6.10. IRM (filled) and TRM (open) of x=30 (squares) and x = 35 (circles) measured at 2 K. Precise field history and timing as described in text. Lines are drawn to guide the eye

due to the fact that 2 K is closer to the spin freezing temperature of the x = 0.30 sample (T_f = 3.0 K) than it is for the x = 0.35 sample (T_f = 3.8 K) and it has been shown that the relaxation processes are temperature dependent and relaxation occurs at a faster rate as T_f is approached (Chamberlin, 1984).

6.2.5. Specific Heat and Resistivity

Low temperature specific heat measurements were performed on both the x = 0.30 and x = 0.35 samples. The magnetic components to the specific heat were found by subtracting from the total specific heat the specific heat of lanthanum and the specific heat of yttrium in the same ratio as terbium and yttrium in the sample,

$$Cp_{mag} = Cp_{Y(1-x)Tb(x)Ni2Ge2} - (1-x)Cp_{YNi2Ge2} - (x)Cp_{LaNi2Ge2}, \quad (6.6)$$

as performed in chapter 5. This magnetic specific heat was then extrapolated to T = 0 K using a $T^{3/2}$ dependence, which is thought to be characteristic for spin glass systems at very low temperatures (Caudron, 1981; Thomson, 1981). This was done so as to account for the entropy below 2 K. These results are shown in Figure 6.11 (a) and (c). The arrows point out T_f for each system. Looking at (a) x = 0.30, many features that are commonly seen in spin glasses are apparent. There is a broad maximum located at 3.8 K, which is about 1.26 T_f. This is in the range of 1.2 – 1.4 T_f which is typical for spin glasses. There is also a gradual decline in the specific heat, which is roughly fit by a 1/T dependence for increasing temperature, which is shown by the solid line in (a). This is similar to what is seen in *Cu*Mn. This existence of this peak and tail shows that the formation of magnetic clusters or short-range order is taking place well above T_f. The

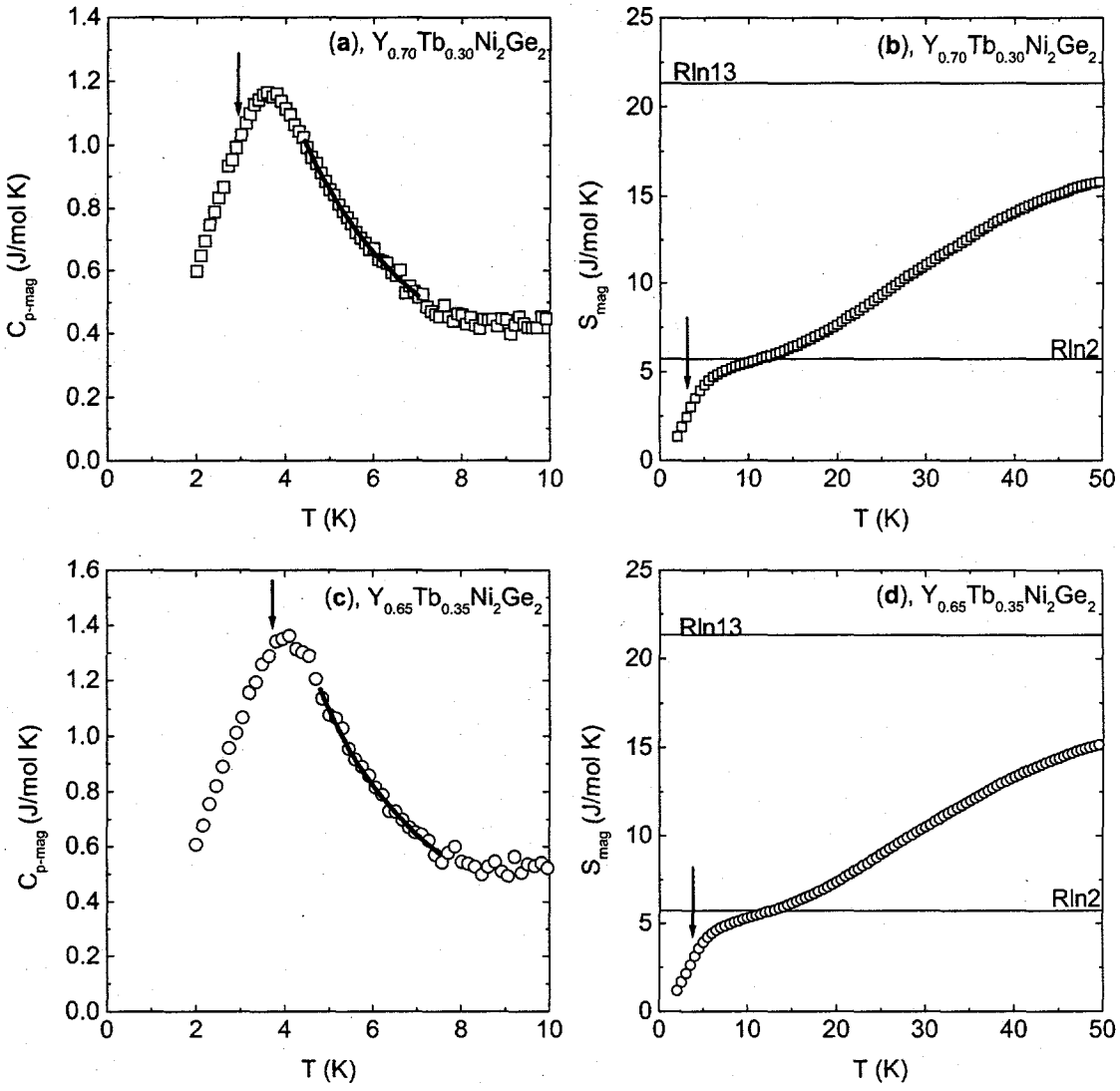

Figure 6.11. Magnetic contribution of the specific heat and entropy as a function of temperature for: (a) and (b) x = 0.30 and for (c) & (d) x = 0.35. Arrows indicate the spin freezing temperatures. Solid lines in (b) and (d) indicate value of Rln13 which is the theoretical total magnetic entropy for Tb^{3+} ion and Rln2 which is theoretical entropy of a degenerate two level CEF ground state.

spin glass state is then formed from these clusters. The gradual tail also shows that the short-range order persists up to higher temperatures, which is due to the relatively strong and long-range RKKY interaction. The fact that no sharp feature is seen at T_f is another feature common to spin glasses. Below T_f, there is an approximately linear dependence to the specific heat, which is the low temperature signature of a spin glass state (Mydosh, 1993).

The magnetic contribution to the entropy is shown in Figure 6.11(b). At 10 K there is a shoulder in the entropy at about Rln2, which is the entropy associated with a ground state doublet, lending confirmation to our assertion that the ground state is a doublet or psuedodoublet. By Tf only about 55 % of this theoretical entropy is present. This is again typical of spin glasses (Chernikov, 2000). In the same manner seen in previous specific heat plots, the high temperature specific heat does not reach its total value of Rln13 by 50 K, so other Shottky-type anomalies may exist at higher temperatures (Bud'ko, 1999).

Many of these same features are seen in x = 0.35, such as the low amount of entropy present at T_f, comparable to that of the x = 0.30. The single greatest difference is that the peak in the specific heat occurs at a temperature which is very close to T_f (~3.8 K). Another difference is that the specific heat above the peak falls off with an approximately $T^{-1.7}$ dependence rather than a 1/T dependence. This is irregular for a spin glass and gives added weight to the previous indications (χ_3) that the composition x = 0.35 is not a particularly good example of a spin glass and is probably too close to the III-IV boundary in Figure 5.7.

Plots of the resistivity for (a) x = 0.30 and (b) x = 0.35 are shown in Figure 6.12. The insets show that, similar to all the other members of this series, the RRR~4. No sharp features exist at or near T_f for either compound. This is normal for spin glasses considering that even in the frozen state there is spin disorder. Because of the very low RRR and the normal 10 % error in the absolute value of the resistivities (see Chapter 4), no quantitative analysis could be performed on these samples, such as finding $\Delta\rho(T)$, the difference between ρ of the spin glass and the ρ of pure YNi_2Ge_2, which could be considered the magnetic contribution to the resistivity. The upturn at low temperatures was also seen for the concentration x = 0.45 (see Figure 5.19). This increase may be due the formation of clusters and short range correlations of the terbium moments before entering into the spin glass state.

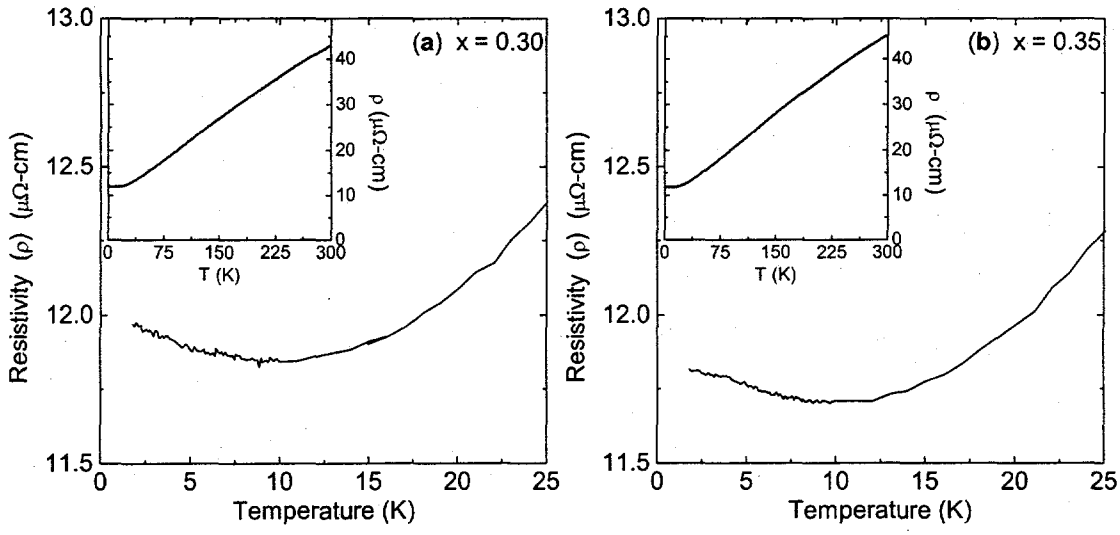

Figure 6.12. Low temperature resistivity measurements for (a) x =0.30 and (b) x = 0.35. Insets show full temperature dependence to illustrate that RRR ~ 4 for both samples.

6.3. Conclusion

In this chapter several measurements have been performed in order to test the irreversibilities seen in the zfc and fc dc magnetization at low temperatures and to determine whether this is a spin glass state or not. It should be clear that for terbium concentrations between x = 0.25 and 0.35 this system is a good Ising, metallic, RKKY coupled spin glass. These systems conform to many of the experimental signatures that are displayed by other more well-known spin glass systems. Of the three concentrations studied in this chapter, the sample with x = 0.30 may be considered the better sample. From χ_3 and specific heat measurements the x = 0.35 sample has irregularities that affect its quality as a spin glass, and the x = 0.25 sample has a freezing transition (T_f = 2.5 K) that is too low to allow several of the critical measurements to be easily performed. It should be possible to explore the various theoretical questions that have arisen in this field with this system. In order to do so will require more detailed measurements at lower temperatures and more sensitive equipment than has been used in this study.

7. CONCLUSIONS

The purpose of this work was to study the response of the magnetization, specific heat and resistivity of the site diluted Ising $Y_{1-x}Tb_xNi_2Ge_2$ system to changes in the concentration x. This was done in the hopes that a good Ising spin glass system could be found. There is much theoretical interest in Ising spin glasses, and in particular their response to an applied transverse field as T approaches 0 K. Recent investigations into quantum phase transitions in Ising spin glasses were performed on members of the dilution series $LiHo_xY_{1-x}F_4$ (Rosenbaum, 1991). These crystals are a site-diluted and isostructural derivative of the dipolar-coupled, insulating, Ising ferromagnet $LiHoF_4$ which has a T_c of 1.53 K. The spin glass transition temperature for the concentration x = 0.167 is T_g = 0.13 K. In contrast, the $Y_{1-x}Tb_xNi_2Ge_2$ system is a metallic, RKKY coupled, Ising antiferromagnet with $TbNi_2Ge_2$ having a T_N = 16.7 K.

Large single crystals of $Y_{1-x}Tb_xNi_2Ge_2$ were grown from a psuedoternary using a self-flux technique. A concern in dilution series such as this, is deviation of actual concentrations of the constituents from the initial nominal concentrations. The actual concentrations were determined from high temperature Curie-Weiss fits and by electron microprobe analysis. Both measurements confirm that deviations from the nominal concentration are small across the series.

Investigations into the magnetic characteristics of the dilution series as a function of the concentration x reveal four regions in the T-x phase diagram. At the large x, there are two antiferromagnetic transitions, as x is decreased the lower transition fades away

and the upper transition continues to decreases in temperature in a linearly with x. It should also be noted that significant differences begin to emerge between zfc and fc susceptibilities measured in low (50 Oe) applied fields. These irreversibilities become stronger and their onset temperature (T_{ir}) increases as the concentration decreases. At intermediate values of x there is a region which shows a mixed behavior, demonstrating a well defined ordering temperature characteristic of long-range antiferromagnetic order and the strong irreversibilities that are signatures of spin glass systems. In the region of $0.25<x<0.35$, the system has lost its long-range order and spin-glass-like features are prominent. As x is changed, the Weiss temperatures determined from Curie-Weiss fits at high temperature change in a linear fashion, demonstrating the scaling of the magnetic interactions with concentration and therefore with the de Gennes factor.

The region displaying a spin glass nature was looked at in more detail. Results of dc susceptibility revealed the formation of clusters at temperatures above the freezing temperature, as well as the irreversibilities due to temperature and field histories. It was also seen that these irreversibilities, characterized by the onset temperature, T_{ir}, follow the AT line theoretically predicted from a mean field theory for Ising spin glasses. From ac susceptibility measurements further similarities with other accepted spin glasses were seen. The nonlinear susceptibility was studied at temperatures near T_f and a sharp feature was seen, which is again typical of spin glasses. Preliminary investigations were undertaken to demonstrate the time dependent nature of the spin glass state at low temperature. Finally, specific heat and resistivity measurements were taken which again demonstrates the onset of clustering well above T_f.

From these measurements, the conclusion must be drawn that a clear Ising spin glass state does exist in this system. A concentration of $0.25<x<0.30$ would probably be the best sample, having strong spin glass characteristics combined with an easily accessible transition temperature. Now that a good, metallic, RKKY coupled, Ising spin glass has been found, the next step will be to apply a transverse field. In order to study the quantum nature of this system, lower temperatures will be needed. At these lower temperatures problems may arise due to the CEF splitting of the ground state. It is thought that the final ground state might be two closely spaced singlets. This means that at low enough temperature the populations of these states will no longer be equally populated and as the upper state empties into the lower state changes in the magnetic properties will occur. The determination of the exact ground state will require specific heat and neutron diffraction measurements at very low temperature ($T<1$ K). It would also be of interest to study the nature of irreversibilities that emerge at high concentrations.

REFERENCES

Ashcroft, N. W., and N. D. Mermin, *Solid State Physics*, (W. B. Saunders, Philadelphia, 1976).

Binder, K., A. P. Young, Reviews of Modern Physics, **58**, 801 (1986)

Bitoh, T., K. Ohba, M. Takamatsu, T. Shirane, S. Chikazawa, J. Magn, Magn, Mater., **154**, 59 (1996)

Boutron, P., Phys. Rev. B, **7**, 3226 (1973).

Brooke, J., D. Bitko, T. F. Rosenbaum, G. Aeppli, Science, **284**, 779 (1999)

Bud'ko, S. L., P. C. Canfield, C. H. Mielke, A. H. Lacerda, Phys. Rev. B, **57**, 13624 (1998).

Bud'ko, S. L., Z. Islam, T. A. Wiener, I. R. Fisher, A. H. Lacerda, P. C. Canfield, J. Magn. Magn. Mater., **205**, 53 (1999)

Canfield, P. C. and Z. Fisk, Phil. Mag., **65**, 1117 (1992).

Caudron, R., P. Costa, J. C. Lasjaunias, B. Levesque, J. Phys. F: Metal Phys., **11**, 451 (1981)

Cava, R. J., H Takagi, H. W. Zandbergen, J. J. Krajewski, W. F. Peck, Jr., T. Siegrist, B. Batlogg, R. B. van Dover, R. J. Felder, K. Mizuhashi, J. O. Lee, H. Eisaki, S. Uchida, Nature (London), **367**, 252 (1994)

Chamberlin, R. V., G. Mozurkewich, R, Orbach, Phys. Rev. Lett., **52**, 867 (1984)

Chamberlin, R. V., M. Hardiman, L. A. Turkevich, R. Orbach, Phys. Rev. B, **48**, 6720 (1982)

Chernikov, M. A., S. Paschen, E. Felder, P. Vorburger, B, Ruzicka, L. Degiorgi, H. R. Ott, I. R. Fisher, P. C. Canfield, Phys. Rev, B, **61**, (2000)

Cho, B. K., P. C. Canfield, D. C. Johnston, Phys. Rev. B, **77**, 163 (1996)

de Almeida, J. R. L. and D. J. Thouless, J. Phys. A, **11**, 983 (1978)

Dunlap, B. D., J. Magn. Magn. Mater., **37**, 211 (1983)

Escorne, M., A. Mauger, D. Ravot, J. C. Achard, J. Phys. C: Solid State Phys., **14**, 1821 (1981)

Fisher, I. R., K. O. Cheon, A. F. Panchula, P. C. Canfield, M. Chernikov, H. R. Ott, K. Dennis, Phys. Rev. B, **59**, 308 (1999)

Fisher, M. E., Phil. Mag., **7**, 1731 (1962)

Hurd, C. M., *Electrons in Metals*, (John Wiley & Sons, Inc., NY, 1975)

Islam, Z., C. Detlefs, A. I. Goldman, S. L. Bud'ko, P. C. Canfield, J. P. Hill, D. Gibbs, T. Vogt, A. Zheludev, Phys. Rev. B, **58**, 8522 (1998)

Islam, Z., private communication (2000)

Katori, H. A. and A. Ito, J. Phys. Soc. Japan, **63** (1994)

Kittel, C., *Introduction to Solid State Physics*, (John Wiley & Sons, Inc., NY, 1996)

Lévy, L. P., Phys. Rev. B, **38**, 4963 (1988)

Massalski, T. B., H. Okamoto, P. R. Subramanian, L. Kacprzak, *Binary Alloy Phase Diagrams*, (ASM International, Materials Park, OH, 1992).

Morgownik, A. F. J. and J. A. Mydosh, Solid State Commun., **47**, 321 (1983)

Mydosh, J. A., *Spin Glasses: an Experimental Introduction*, (Taylor & Francis, Washington DC, 1993)

Myers, K. D., P. C. Canfield, V. A. Kalatsky, V. L. Pokrovsky, Phys. Rev. B, **59**, 1121 (1999).

Nagarajan, R., Chandan Mazumdar, Zakir Hossain, S. K. Dhar, K. V. Gopalakrishnan, L. C. Gupta, C. Godart, B. D. Padalia, R. Vijayaraghavan, Phys. Rev. Lett., **72**, 274 (1994)

Nordblad, P., P. Svedlindh, L. Lundgren, L. Sandlund, Phys. Rev. B, **33**, 645 (1986)

Rosenbaum, T. F., J. Phys. Condens, Matter, **8**, 9759 (1996)

Rosenbaum, T. F., W. Wu, B. Ellman, J. Yang, J. Appl. Phys., **70**, 5946 (1991)

Rosenberg, H. M., *Low Temperature Solid State Physics*, (Oxford University Press, London, 1965)

Rossat-Mignod, J., P. Burlet, J. Villain, H. Bartholin, Wang Tcheng-Si, D. Florence, O. Vogt, Phys. Rev. B, **16**, 440 (1977)

Taylor, K. N. R. and M. I. Darby, *Physics of Rare Earth Solids*, (Chapman and Hall, London, 1972).

Tholence, J. L. and R. Tournier, J. Phys. (Paris), **35**, C4-229 (1974)

Thomson, J. O. and J. R. Thomson, J. Phys. F: Metal Phys., **11**, 247 (1981)

Villars, P., Pearson's Handbook Crystallographic Data for Intermetallic Phases, (ASM International, Materials Park, OH, 1997)

Wiener, T. A., and P. C. Canfield, "Magnetic Phase Diagram of Flux-Grown Single Crystals of CeSb" 2000a, (accepted for publication in J. Alloys Comp.)

Wiener, T. A., and P. C. Canfield, "The Magnetic Characteristics of the $Tb(Ni_{1-x}Co_x)_2Ge_2$ System" 2000b, (accepted for publication in J. Alloys Comp.)

Wu, W., D. Bitko, T. F. Rosenbaum, G. Aeppli, Phys. Rev. Lett., **71**, 1919 (1993)

ACKNOWLEDGEMENTS

I would like to express my sincere appreciation to my advisor, Paul Canfield, for his encouragement, guidance, and strong desire to share his knowledge. His enthusiasm for physics is inspiring.

I am thankful to Sergey Bud'ko, who has shared much knowledge and insightful discussions with me. His help with the specific heat and ac susceptibility studies has added greatly to this work.

I would like to acknowledge Ian R. Fisher for blazing the trail through the forest of spin glass studies. His help and critical review of this work were invaluable.

I am indebted to Zahirul Islam and Changyong Song for their help with the X-ray diffraction, and Alfred Kracher for the electron microprobe analysis (EMPA) to confirm concentration amounts in the samples.

I would also like to thank Jason Schissel, Norm Anderson, and Nathan Kelso for their help cutting metal, arcmelting, filling cryogens, and performing other important tasks.

I am deeply appreciative of the support and encouragement I received from my mother and father and my mother-in-law and father-in-law. I would especially like to thank my wife, Kristin for all that she has put up with over the last year.

This work was performed at Ames Laboratory under Contract No. W-7405-Eng-82 with the U. S. Department of Energy. The United States government has assigned the DOE Report number IS-T 1910 to this thesis.